THE LOADING AND FUNCTION OF THE MITRAL VALVE UNDER NORMAL, PATHOLOGICAL AND REPAIR CONDITIONS: AN IN VITRO STUDY

A Dissertation
Presented to
The Academic Faculty

by

Jorge Hernan Jimenez Mejia

In Partial Fulfillment
of the Requirements for the Degree
Doctor in Philosophy in Bioengineering

Georgia Institute of Technology

December, 2006

THE LOADING AND FUNCTION OF THE MITRAL VALVE UNDER NORMAL, PATHOLOGICAL AND REPAIR CONDITIONS: AN IN VITRO STUDY

Approved By:

Dr. Ajit P. Yoganathan , Advisor
School of Biomedical Engineering
Georgia Institute of Technology

Dr. Thomas Vassiliades
School of Medicine
Emory University

Dr. Marc Levenston
School of Mechanical Engineering
Georgia Institute of Technology

Dr. Joseph Gorman
School of Medicine
University of Pennsylvania

Dr. John Oshinski
School of Biomedical Engineering
Georgia Institute of Technology

Date Approved: November 10, 2006

A la familia, lo mas importante en la vida.

A aquellos amigos que son como hermanos.

ACKNOWLEDGEMENTS

There are a number of people I would like to thank for their help and support during the last five of years. First, I would like to thank my family, you are always there with loving support, basically, you are my reason for wanting to be a better person.

Special thanks, goes to my advisor Dr. Ajit P. Yoganathan for your guidance and your support, which allowed me to take full advantage of the opportunities I was given at Georgia Tech. I would also like to thank Dr. Marc Levenston, Dr. John Oshinski, Dr. Thomas Vassiliades, and Dr. Joseph Gorman for being part of my thesis committee.

I would like to thank all the members of the Cardiovascular Fluid Dynamics Laboratory for your support and friendship: Zhaoming and Dr. He thank you for everything you taught me. Dennis "thanks" for your friendship and collaboration, and for the technical information which is presented in Appendix A of this thesis. To Laura, Will, Christina, Mark, James N, Michael, Jenny, Anna, Ashley, Murali, Donni, Yap, Resmi, Kartik S, Kartik B, Diane, Helene, Philippe, Yun, Suchitra, Claire, Amanda, Lisa, Leo, Dave, Steffen, Hiromi, Prasad, Chang, James W, Kerem, and Casey, it was great working with you guys.

To Chris, Pat, Colly and Michelle, you guys have been great and made my life here much easier. To Jim McEntee and the Holifield Slaughter house, thank you for your contributions to my work. In addition, I would like to thank the National Institute of Health for the support which made my work possible (grant # HL52009).

A Paola gracias por la inspiración para seguir adelante, tu amor y apoyo incondicional me dieron mucha fuerza para continuar y no dejarme llevar en los malos momentos. A

mis amigos, ustedes saben quienes son, les agradezco en el alma haberme apoyado en las buenas y especialmente en las malas. Gracias por ayudarme y darme el ánimo para llegar donde siempre he querido.

TABLE OF CONTENTS

LIST OF TABLES

LIST OF FIGURES

ABBREVIATIONS

Abbreviation	Definition
MV	Mitral Valve
PM	Papillary Muscle
MR	Mitral Regurgitation
LV	Left Ventricle
CO	Cardiac Output
F_A	Alfieri Stitch Force
HR	Heart Rate
APM	Anterolateral Papillary Muscle
PPM	Posteromedial Papillary Muscle
TEE	Trans-Esophagic Echocardiography
FMR	Functional Mitral Regurgitation
MS	Mitral Stenosis
VASAC	Variable Annular Shape Atrial Chamber
PSF	Peak Systolic Force
PSS	Peak Systolic Stress
TP	Transmitral Pressure
SL	Septal-Lateral Diameter
EOA	Effective Orifice Area
SR	Saddle Height to Commissural Diameter Ratio

MAA	Mitral Annular Area
MFR	Mitral Flow Rate
SG	Strain Gauge
2D	2-Dimensional
3D	3-Dimensional

SUMMARY

Currently, mitral valve repair techniques have shown substandard mid-term and long term results. In order to improve the efficacy of these repair techniques, detailed knowledge of normal mitral valve function and the alterations to the valvular and subvalvular apparatus which occur under pathological conditions is required. Furthermore, current techniques may be optimized through a better understanding of the function and mechanics of the mitral valve after a particular repair.

The experiments which comprise this study were designed using an *in vitro* approach since this technique has the clear advantage of isolating and independently controlling specific parameters that are of importance to valvular mechanics and function. The experiments were conducted in the Georgia Tech Left Heart Simulator using native porcine and human mitral valves. The first set of experiments measured the chordal force distribution and anterior leaflet strain of the mitral valve in its normal geometrical configuration. Subsequent experiments measure mitral regurgitation volume and chordal force distribution in conditions associated with ventricular dilation. The last set of experiments simulated two commonly used mitral repair techniques. For the Alfieri stitch experiments, the effects of mitral flow rate, transmitral pressure, and mitral annular area on valve stenosis, mitral regurgitation and Alfieri stitch force were evaluated. For annuloplasty, the effect of annular saddle curvature on anterior leaflet strain was quantified.

In Conclusion, the normal geometry of the native mitral valve optimized its function and mechanics. Under pathological conditions associated with ventricular dilation, significant

alterations to mitral valve function and mechanics were present. Although the studied repair techniques may have significantly restored valve function, severe alterations to the mechanics of the valve still persisted.

CHAPTER I

INTRODUCTION

Mitral valve (MV) malfunction both as a primary and secondary pathology is a major and increasingly prevalent clinical problem which challenges cardiac surgeons and cardiologists alike. Rheumatic disease, myxomatous degeneration and congenital abnormalities are primary pathologies which directly affect MV function. As a result of the reduction in the prevalence of rheumatic disease in the United States, the treatment of MV malfunction as a primary pathology has been relegated in importance by its treatment when present as a secondary pathology.

Ventricular dysfunction due to ischemic heart disease or dilated cardiomyopathy often leads to MV insufficiency [1]. Though a secondary pathology resulting from ventricular remodeling, associated MV malfunction significantly increases patient mortality. Patients with dilated cardiomyopathy have a mortality of 50% five years after initial diagnosis and 75% after ten years [2]; a significant contribution to these statistics being the associated mitral insufficiency. In terms of the affected population, ischemic mitral regurgitation (MR) is the most prevalent of the aforementioned clinical problems. Statistics by Grigioni *et. al.* 2001 showed that patients with MR after myocardial infarction have a 23% reduced survival rate after 5 years [3]. Therefore, from the 7 million patients in the United States which suffer from myocardial infarction each year [4], 1.6 million may die from conditions exacerbated by MR. Because of the large population and significant mortality associated with MR as a

secondary pathology, treatment of MV insufficiency has become a major area of research and innovation in recent years.

Mitral valve repair has been shown to have significant advantages over MV replacement. Since heart valve replacement has a higher incidence of complications in the mitral position, MV repair is becoming the procedure of choice when dealing with most MV related pathologies [5]. Although recent statistics show a favorable trend towards repair, only 36% of mitral interventions are repair procedures, whereas 64% are replacements [6], leaving significant room for growth. The higher number of replacements is associated with the technical complexity and level of surgical expertise needed to perform a successful mitral repair.

The MV is the most complex and heavily loaded of the four valves in the heart. Its function is characterized by the elaborate interplay of its different components, which are still not well understood. Recent publications associated with MV mechanics have demonstrated that the geometry of the MV [7, 8], its constituent specific dynamics [9-11], the material properties of its components [12, 13], and the living elements of its structure [14-17] optimize its function and mechanical configuration. In brief, normal valvular geometry and dynamics decreases leaflet stress [8], improves chordal force distribution [7], enhances ventricular filling and reduces closing volumes [9]. Therefore, alterations to the normal MV will lead to substandard function and unfavorable mechanics.

Studies have also shown how the mechanics of different components of the MV are altered in instances of ventricular remodeling. Several studies have reported changes in mitral annulus geometry and dynamics in patients with dilated cardiomyopathy and ischemic heart diseases [11, 18, 19]. In all these studies, geometrical and dynamic changes on the MV

annulus were associated with different degrees of mitral malfunction, characterized by the presence of clinically significant levels of MR. Complementary studies have shown how dilated cardiomyopathy reduced papillary muscle (PM) contractility [10] and increased endocardial radius of the left ventricle [20]. Additionally, Gorman III *et. al.* 1997 showed using an ovine model how the PMs lost contractility and became displaced under ischemic conditions [21]. During pathologies associated with ischemic heart disease and cardiomyopathy such as ischemic MR and functional MR, changes in annular geometry, annular dynamics, PM function and location have been identified [10, 18-21]. Although the primary pathology is a ventricular disease and should be addressed biochemically, subsequent MR may be addressed surgically through repair or replacement.

Currently most repair procedures address individual components of the MV leading to abnormal interactions and mechanics after the repair. Since the MV is a structural entity, successful repair procedures should address the valve as a whole, by addressing all its components and their interaction:

"Identification of the malfunction of each of the components of the mitral valve apparatus is essential for a successful repair" **[22]**

For the past three decades, MV repair has been centered on resizing the mitral annulus through annuloplasty. Although annuloplasty has shown good results for some pathologies and is the standard for MV repair, long term results in conditions associated with continual ventricular remodeling or dilation require improvement [23, 24]. Additionally, studies have shown that annuloplasty, even with flexible rings, severely restricts annular dynamics [25]. Annular dynamics have been shown to improve MV function [9] and mechanics [7-8].

As leaflet coaptation is the endpoint through which MR occurs, more recent approaches are aimed directly at correcting systolic leaflet coaptation. The Alfieri stitch is a commonly used adjunctive procedure which restores leaflet coaptation through a stitch joining the tips of the posterior and anterior leaflets [26]. An advantage of this procedure is its feasibility for less invasive approaches. Midterm studies [,27] have shown positive results for the Alfieri stitch in conjunction to annuloplasty, but substandard results when performed alone [28]. Although this procedure may restore coaptation it results in abnormal diastolic and systolic MV mechanics [29-31].

Recently clinicians have started to acknowledge the necessity of addressing the subvalvular apparatus, especially for those pathologies associated with ventricular remodeling or dilation.

***"Finally, if we can break through our denial, which is always tough for a surgeon, and accept that simple ring annuloplasty is not enough for patients with IMR, is there anything we can add to a ring at the ventricular level to improve things, such as a Coapsys device or other method of LV reshaping?"*[32]**

As previously described, ventricular remodeling or dilation repositions the PMs and therefore alters the chordal force distribution resulting in leaflet malcoaptation. Chordal replacement and transposition will address failure of the chordal apparatus, but currently there is no widely accepted procedure which restores PM position and chordal force distribution. Ventricular reconstruction procedures have been proposed but are rarely used because of their invasiveness [33]. Recently, as a result of the need for addressing the subvalvular apparatus, devices such as the Coapsy system have been developed with the intent of repositioning the PMs [34], but currently these devices have not been approved by the FDA.

The development of new techniques such as those mentioned above has improved patient survival and quality of life, yet current repair procedures are far from perfect. Recent studies have shown that within 5 years after the initial repair, significant levels of MR recur in most patients [23 , 24]. These studies have also shown that most of the failures are due to a lack of durability of the initial repair (i.e. procedural related factors). In order to increase the efficacy and long term durability of the initial repair, improved post interventional mechanics of the MV are essential. The clinical community has started to understand that optimizing mechanics by minimizing abnormal or residual stresses should improve repair durability:

"The aim of mitral repair is not only to obtain a valve that no longer leaks, but also to achieve anatomical restoration of all components of the mitral apparatus, so that the mechanical stress on the valve, whose tissue is abnormal, is reduced to a minimum." [22]

The overall objective of the research presented here is to better understand normal MV mechanics and function and how alteration due to ventricular remodeling and subsequent repair procedures may affect this function and dynamics. The research presented in this thesis initially studies MV function, leaflet strain and chordal stress distribution under normal conditions. Additionally, changes in MV function and chordal stress distribution are also studied for different PM positions associated with ventricular dilation. Finally, alterations to valvular mechanics and function after two commonly used repair procedures are also addressed. For the Alfieri repair different variables of both diastolic and systolic function and stitch force are studied for different configurations of the MV. For annuloplasty, the effect of ring saddle height to commissural diameter on MV function and leaflet strain was also studied.

To independently analyze the variables of interest, *in vitro* experiments were utilized. *In vitro* experimental capabilities have a clear advantage of focusing on and independently

controlling parameters that are of importance to MV mechanics and function. These experiments will provide detailed quantitative information on function and mechanics in the normal, pathological and repaired MV. Qualitative and quantitative information from the experiments presented here may provide a bases or guide which may lead to improved long term results for mitral repair interventions.

CHAPTER II

BACKGROUND

2.1 The Heart

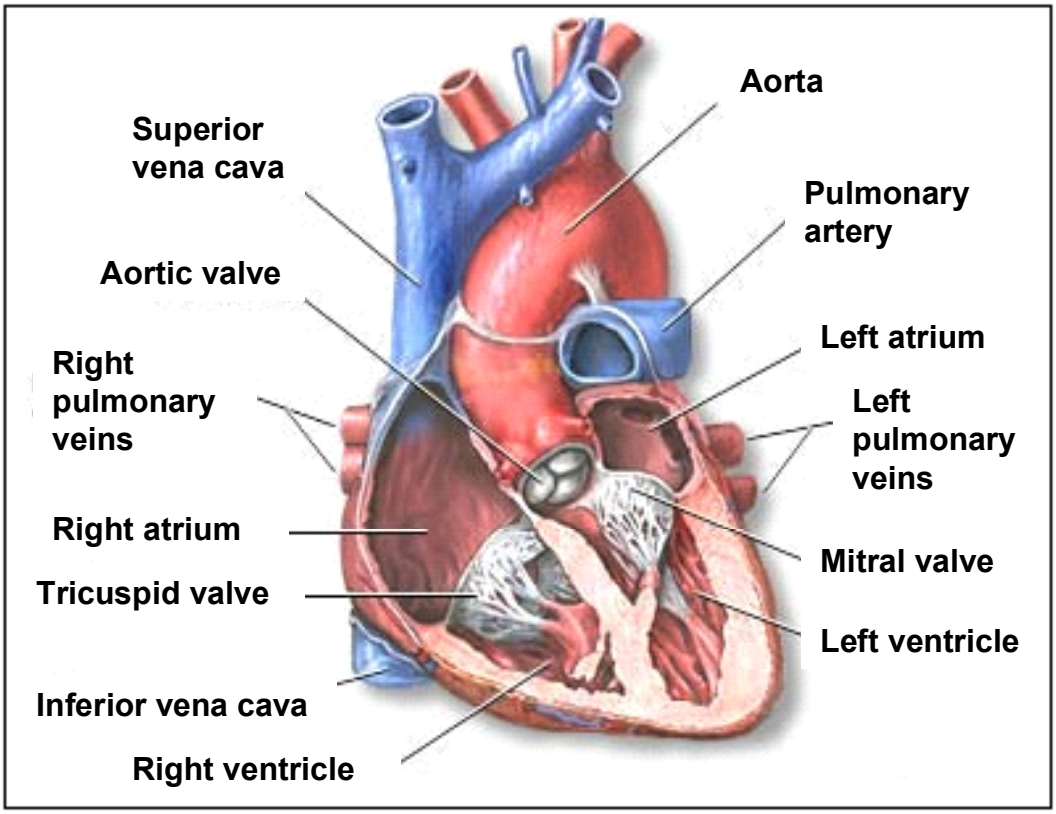

Figure 2.1 Diagram of the heart and its components. (http://www.nlm.nih.gov/ medlineplus/ency/imagepages/1056.htm)

The human heart is a hollow, cylindrical shaped muscular organ, that constitutes the driving force for the circulatory system. The heart to some extent may be considered to be two independent pumps. Each separate pump is comprised of two separate chambers, a superior atrium and a lower ventricle. These chambers are separated by atrio-ventricular (A-V) valves, which control flow between the chambers. Semilunar valves in the

ventricles control backflow from the arteries. Pump synchronicity is controlled by electrical potentials originating at the sinus node and traveling through the atrio-ventricular bundle [35]. Therefore, the heart is comprised of four valves and four chambers, which pump non-oxygenated blood through the lungs, and then, newly oxygenated blood into the systemic circulation (Figure 2.1).

The function of the right side of the heart is to pump blood returning from the circulatory system into the lungs. The right side of the heart is considered a low-pressure system, as its function only requires pressures up to 40mmHg gauge [36]. Right heart dysfunction is normally associated with congenital or pulmonary pathologies, which may be caused by idiopathic mechanisms or thromboembolic events.

Sustaining pressures of up to 150mmHg, the left side of the heart pumps blood into and through the systemic circulation. The left atrium has a volume of approximately 45ml and works at pressures up to 25mmHg. The left ventricle has an approximate volume of 100ml and works normally at a pressure of 120 mmHg, although pressures may increase to 150mmHg under pathological conditions. Left heart dysfunction can be associated with ischemic heart disease, hypertension, cardiomyopathy, valvular pathology, congenital defects, bacterial and infectious processes, and other pathological factors. Valvular pathologies are predominant in the left side of the heart, a fact which has been thought to be associated with increased mechanical loads.

The heart as a whole is a complex and synchronized mechanism. Between its four chambers it holds around 350ml of blood, which is approximately 6.5% of the total blood volume of a typical individual [36]. Because of its limited volume, the heart must cyclically pump to ensure continual renewal of oxygenated blood in the tissues.

Underlying these functional characteristics, the heart hosts several electrical, chemical and biological events, which also characterize this highly complex life sustaining pumping system.

2.2 The Mitral Valve

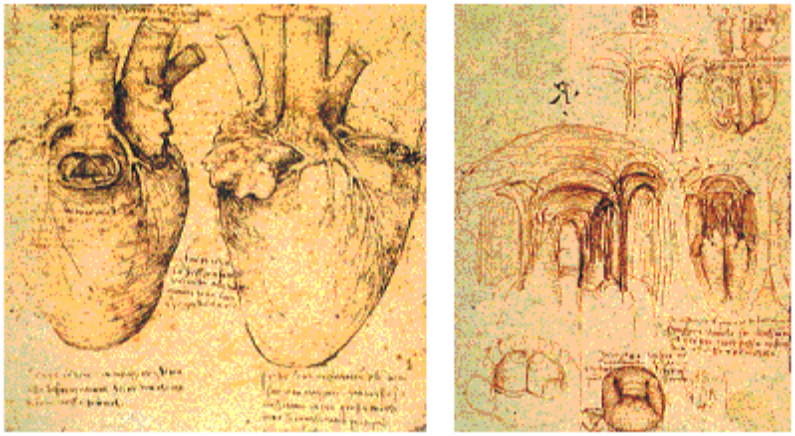

Figure 2.2 Sketches of the human heart by Leonardo Da Vinci and Andreas Vesalius (Jensen *et. al.* 2000)

Because of its life sustaining function, its complexity, and its multiple components, extensive research on the heart has been performed for centuries [37]. Within valve function, special emphasis has been placed on the mitral valve since it is the most heavily loaded and complex of the four valves present in the heart. As shown in these sketches by Leonardo Da Vinci and Andreas Vesalius (Figure 2.2), the basic structure and function of the mitral valve has been known for centuries. But only until recently have researcher begun to understand the detailed mechanics and individual function and interaction of its components.

The mitral valve is a complex unit comprising the annulus, the leaflets, the chordae tendineae, and the underlying left ventricular myocardium [38]. The mitral valve is attached to the left atrium and ventricle through its annulus, while the papillary muscles extend from the anterolateral and posteromedial sections of the ventricle. The PMs are named according to their location within the ventricle, as the anterolateral papillary muscle (APM) and posteromedial papillary muscle (PPM). The PMs communicate to the leaflet by the way of the chordae tendineae (Figure 2.3). These chords extend from the bellies of the PMs and insert relatively symmetrically to both leaflets and the annulus.

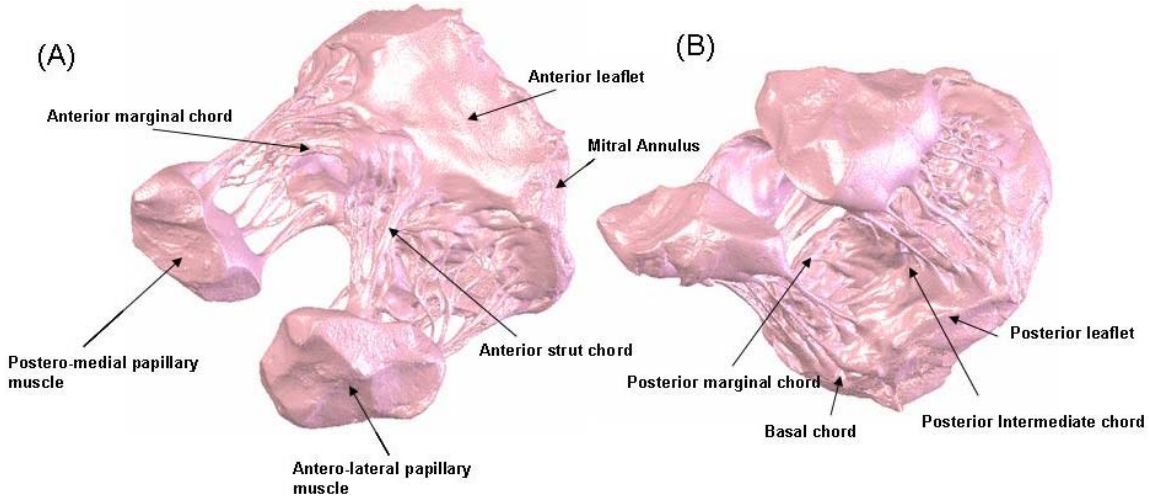

Figure 2.3. (A) Anterior view of microCT reconstruction of a porcine mitral valve. (B) Posterior view of microCT reconstruction of a porcine mitral valve.

The mitral valve is separated from the aortic valve by the intravalvular curtain. Under normal conditions these valves maintain a 135-degree angle between them. The section of the annulus adjacent to the aortic valve holds the anterior leaflet, which is the largest leaflet by area. The mitral valve uses residual tissue on the tips of its leaflets as sealing or coaptation surfaces. To accomplish its purpose under complex conditions, the mitral

valve is redundantly designed, having on average a leaflet surface area two times larger than the area of the mitral orifice [39].

2.2.1 Mitral Valve Leaflets

Although there is large valve to valve anatomical variability in the mitral leaflets, several features are consistently observed in all normal specimens. The leaflet section of the mitral valve consists of a continuous veil of tissue [38], which inserts into the annulus around the entire circumference of the mitral orifice.

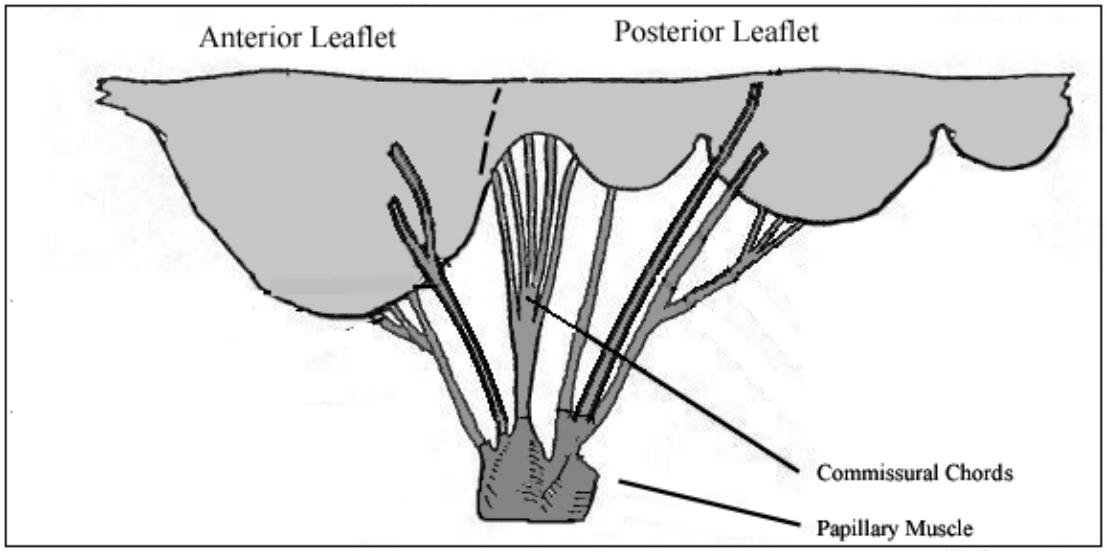

Figure 2.4 a) Diagrammatic representation of the mitral valve with fan-shaped commissural and cleft chordae tendineae attached.

As shown in Figure 2.4, two major leaflet sections may be identified regularly, and because of their location within the valve, they have been named the anterior and the posterior leaflets. These leaflets are separated by two commissural sections located in the anterolateral and posteromedial sections of the ring. As observed, the commissural

sections of the annulus are characterized by fan-like chordae tendineae insertions. The commissural sections of the valve are part of the posterior system; therefore, the mitral valve generally (92% of cases) [38] contains three scallops in its posterior section. The major central scallop is usually called the posterior leaflet, while the other two are described as commissural scallops and identified by location (postero-medial commissural scallop and anterolateral commissural scallop).

Three major zones can be identified in both leaflets: 1) a rough zone in its distal section, 2) a clear zone proximal to this, and 3) a basal zone. Both, the rough and basal zones receive chordae tendineae insertions, while the clear zone is membranous and relatively smooth [38].

The posterior leaflet, scallops included, attaches to the larges section of the mitral orifice perimeter. The posterior leaflet is characterized by its dense insertion of chordae tendineae. Because of this dense insertion of chords, the ventricular surface of the posterior leaflet is extremely wrinkled and dominated by ridges. During coaptation, the central scallop of the posterior leaflet tends to be stretched out and in contact with the anterior leaflet, while the commissural scallops cover the limiting sections between the two leaflets.

The anterior leaflet has a significantly larger area than the posterior leaflet, and during coaptation covers most of the mitral orifice. As the anterior leaflet covers most of the mitral orifice, it is subject to a larger load due to pressure. The anterior leaflet is also subject to a significantly lesser insertion of chords. Two major strut chords insert into the midsection of the leaflet while several marginal chords insert into its tips. Because of the larger orifice area covered by the leaflet and the chordal insertion pattern, the anterior

leaflet billows during coaptation. The curvature generated by billowing has been shown to be of mechanical importance, as it reduces the stress on the anterior leaflet material [40]. Because of its size and function, the anterior leaflet is considered the most important scallop on the mitral valve.

At a structural level, the MV leaflets are composed of three layers that may be observed under the microscope, an endothelial layer on the atrial side, an intermediate layer of fibrous material called spongiosa, and a ventricular endothelial layer. An important characteristic of this arrangement is the underlying collagen microstructure in the intermediate layer [12],[13]. Like some other collagenous tissues, the MV anterior leaflet has been shown to be quasi-linear-elastic, and, because of the directionality of the collagen fibers, it has been shown to be anisotropic [41]. Characteristics such as increased surface area during closure, collagen fiber locking after valve coaptation and their mechanical significance have revealed the specificity of mitral leaflet material to its function.

In addition, mitral valve leaflets are not simple membranes. The presence of nerves, vessels, and smooth muscle cells capable of contraction makes them complex biological systems. Recent research has shown that smooth muscle cell contraction may contribute to the tone of the aortic leaflets [16, 17]. As these cells are also present in the mitral valve, the function of these leaflets may not be passive.

2.2.2 The Mitral Annulus

Although the mitral annulus has been described anatomically as an incomplete and almost diaphanous structure, recent findings have enlightened it as a vital component of

the mitral valve. The anterior section of the mitral annulus connects to the aortic valve through the intra-valvular curtain and is delimited by two cartilaginous masses called the annular trigones. In past years, researchers thought that this section of the annulus was rigid, but a recent study has shown that it changes in length during the cardiac cycle [42].

The sphincteric action of the annulus aids ventricular filling by expanding during diastole, and facilitates leaflet coaptation by contracting during systole [9]. Because of its fundamental function, several recent studies both in humans and animals have been focused on describing annular dynamics. Annular area and its dynamics are important parameter, not only for the understanding of mitral valve function but also for the design of cardiac implants such as annuloplasty rings. Elaborate studies using invasive methods in animals and non-invasive methods in humans have revealed important but sometimes conflicting data on annular size. Initial measurements by Davids and Kinmonth [43] using radiopaque markers around the canine annulus revealed a 30% change in annular area, with annular contraction beginning during atrial systole. Other studies in dogs using radiopaque markers and echocardiography, in sheep using 3-D sonomicrometry, and in pigs using echocardiography revealed annulus area reductions ranging from 34% to 12%[9]. Although there was a significant disparity in the magnitudes of the measurement and the exact timing of the onset of mitral annulus contraction, all of these studies supported the idea of a pre-ventricular-systole mitral annulus contraction. Therefore, animal studies support the hypothesis that the mitral annulus begins contraction during atrial systole, and continues to contract through ventricular systole.

In humans, two-dimensional [44] and three-dimensional echocardiography [45] have been the method of choice to study annular dynamics, although in recent years additional

studies have been conducted using MRI [46]. There is a large disparity in the measurements of human annular size and dynamics. Using advanced imaging techniques, researchers rely on their ability to identify anatomical markers to identify the annulus. Therefore, all of these studies may be hindered by human judgment and error. As with animal measurement, although there is disparity in magnitudes, human studies also agree on the concept of annular contraction at the onset of left atrial systole, that continues through ventricular systole. Systolic annular area in these studies varied from 4.5cm^2 to 12cm^2, and diastolic annular area ranged from 5.2cm^2 to 12cm^2 [9].

Another controversial characteristic of the mitral annulus is its shape. Initially, the annulus ring was thought to be a flat structure, but imaging during the cardiac cycle showed apical-basal flexing of the mitral annulus both in animals and in humans. Recent studies have further elucidated the characteristics of annulus shape by demonstrating that the three dimensional curvature of the mitral annulus persists during the whole cardiac cycle [18]. Based on recent studies, the mitral annulus is described as a three-dimensional saddle because it resembles a non-planar, three-dimensional ellipse. In addition to its position, the area, the eccentricity, and the non-planarity or curvature of the mitral annulus varies during the cardiac cycle describing a dynamic structure [9], [21], [47-49]. Mitral annular geometry and dynamics have been studied *in vivo* in animals [21], [48-50] and humans [11], [45], [51-53] both in normal and pathologic subjects. Three-dimensional echocardiographic studies on the shape of the mitral annulus have proposed saddle heights from 0.78±0.11cm to 1.2±0.2cm in humans [18], [19]. Another factor related to annular shape that has been recently studied is the saddle height to commissural ratio. The interest in this parameter is that a computational model of the anterior leaflet showed

that a saddle height to commissural ratio of 20%, (approximately what is present in humans and other animals) will optimize mechanical performance by reducing the stress on the anterior leaflet [8].

The mitral annulus does not only contract and bend, but it also moves during the cardiac cycle. The mitral annulus has been observed to displace across the apico-basal axis of the left ventricle. During systole, the mitral annulus moves basaly 10±3mm [19] from its most apical position during diastole.

As described above, the mitral annulus is not a simple rigid ring which holds the leaflets, as proposed in the past [38], but an important dynamic structure which aids the mitral valve in its function.

2.2.3 The papillary muscles

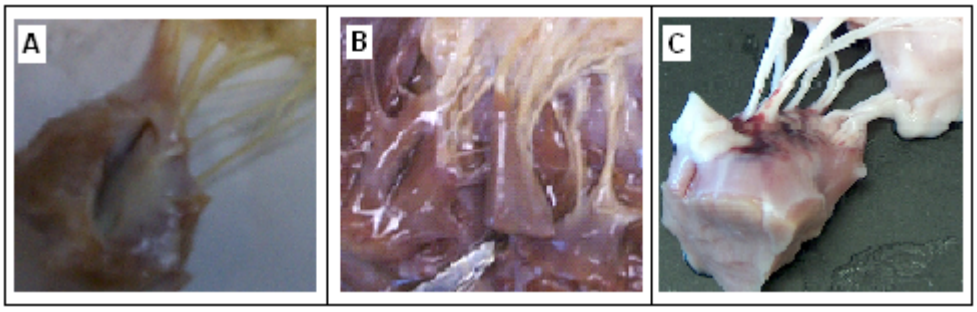

Figure 2.5. Photographs of papillary muscles: A) Simple human papillary muscle B) Complex human papillary muscle C) Porcine papillary muscle.

Two sets of papillary muscles extend from the left ventricle wall: the anterolateral and the posteromedial. From the "bellies" of each papillary muscle, several chordae tendineae extend, and may insert into the valves leaflets or near the annulus as well as into the left ventricular wall. The tips of the papillary muscle usually point to their respective

commissures [54], sending their chords to relatively symmetrical insertions on the valve. Papillary muscle bellies and chordal insertion patterns vary significantly between humans and also between species. According to their complexity, human PMs have been divided into four group types, type I being the simplest and type IV being the most complex. Normal porcine PMs are anatomically simple, and therefore, may be compared to a type I human PM (Figure 2.5).

From each PM belly individual muscle excursions hold individual chords. Even though the PMs are geometrically complex, average lengths and dimensions have been recorded in literature. In healthy sheep, sonomichrometry transducer studies have shown average APM lengths of 23.2mm during diastole and 20.1mm during diastole. Simultaneously, the lengths of the PPM were 25.2mm during diastole and 23.0mm during systole [21]. Therefore, papillary muscle contractions on the order of 2-3mm are present in sheep models. Transesophagic echocardiography (TEE) studies have been able to assess both length and cross sectional area of the normal human PMs *in vivo* [10]. The average cross-sectional areas were 1.32±0.29cm^2 for the APM and 0.99±0.18cm^2 for the PPM at end diastole. At end systole, these areas changed to 1.71±0.31cm^2 for the APM and 1.18±0.20cm^2 for the PPM. In the same study, end diastolic APM length was 3.55±0.33cm and end diastolic PPM length was 2.91±0.20cm. End systolic APM length was 2.81±0.35cm and end systolic PPM length was 2.42±0.23cm. As these results show, human PM contract during systole by approximately 4mm [10].

Although several studies have described their geometry, the actual dynamics of human PM motion are still unknown, mostly because of limitations in the time resolution of the imaging techniques.

2.2.4 Chordae Tendineae

The main function of the chordae tendineae is to prevent leaflet prolapse during ventricular systole. These chords, not only hold the leaflets in place during systole, but are of great significance in the geometrical conformation of the mitral valve and play an important role in left ventricular function. The chordae tendineae extend from both PMs and insert into different sections of the leaflets. Several anatomical studies have been conducted that characterized the chords in different groups. Normally, chords were characterized by their insertion point in the leaflets. Raganathan *et. al.* 1970 named the chords according to the location of their leaflet insertion as rough, cleft and basal. Recently simpler nomenclature has been used to characterize chords [55]:

1. *Primary or marginal*: These chords extend from the PMs, and insert into the free margin of the leaflets.
2. *Secondary or intermediate*: These chords originate in the PMs and insert into the body of the ventricular surface of the leaflets.
3. *Basal chords*: These chords originate in the PMs and insert near or into the mitral annulus.

This classification is not based solely on anatomical location, as differences in composition, size, mechanical characteristics and function have been identified.

Marginal chords are significantly thinner than basal chords. Sedransk *et. al.* 2002 observed that on average the marginal chords were 68% thinner than the basal chords, and that the chords on the posterior leaflet were 35% thinner that their counterparts on the anterior leaflet of porcine mitral valves [56]. Using a calibrated optical microscope on

porcine chordae tendineae, results from Liao *et. al.* 2003 verify the fact that the marginal chords are thinner, assuming circular cross sectional areas and uniform thickness through the chord [57]. The average cross-sectional areas in this study were 0.38±0.18mm^2 for the marginal chords, 2.05±0.40mm^2 for the intermediate chords, and 0.71±0.25mm^2 for the basal chords. Researchers have described the anatomies of porcine and human mitral valves as very similar. Kunzelman *et. al.* 1994 described similar lengths in porcine and human mitral valve chordae tendineae [58], but there are limited data on the cross-sectional area of human chords. Therefore, most studies relay on porcine data.

Although limited mechanical characterization of the chordae tendineae exists in the current literature, recent studies have elucidated important differences between chords that may be associated to their function. Uniaxial tensile tests showed how porcine marginal chords failed at significantly lower tension when compared to basal chords. But when considering the relations in cross-sectional area, failure stress followed a different trend, as presented in Table 2.1[56].

Table 2.1. Failure tension and failure stress for porcine marginal and basal chordae tendineae [56].

Location		Failure Tension (kg)	Failure Stress (N/mm2)
Anterior	Marginal	0.730±0.098	12.93±1.43
	Basal	2.270±0.264	9.63±0.95
Posterior	Marginal	0.420±0.035	7.98±0.82
	Basal	1.293±0.144	10.69±1.26

Further research by the same group revealed interesting relations between geometry and mechanical characteristics of the chords, which were then related to their microstructural composition and organization [57].

Table 2.2 Extendibility, tensile modulus and average chordal size for porcine chordae tendineae [57].

Chordal Type	Marginal	Basal	Strut	Significance
Extendibility(% strain)	4.3±1.6	8.5±3.0	17.5±3.3	p<0.001
Tensile modulus (MPa)	84.4±21.2	86.1±20.9	64.2±13.5	p=0.002
Average chordal size (mm2)	0.38±0.18	0.71±0.25	2.05±0.40	p<0.001

As shown in Table 2.2, extendibility increased with diameter, while the modulus of elasticity decreased with increasing diameter. All results showed statistically significant difference between the different types of chords.

All chordae present an inner layer characterized by a high concentration of collagen and an outer layer that is mostly elastin with interwoven collagen fibers [57], [59]. The collagen microstructure is characterized by directional crimping. Studies have shown that thicker chordae had a smaller crimp period of the collagen fibers, which allowed increased strain on thicker chords before lockup [57]. Although the cross–sectional area occupied by the collagen fibers is constant (49.2% on average), the thicker chords have a larger average fibril diameter but less fibril density [57]. Hematoxylin and eosin staining has shown fibroblasts evenly distributed throughout the inner and outer layer of the chordae tendineae [59]. Blood vessels have also been observed in the longitudinal and circumferential directions of porcine chordae [59].

The results presented above show how the chordae tendineae have a very complex material structure, which varies from chord to chord according to their specific mechanical function.

2.3 Mitral Valve Hemodynamics

During isovolumetric relaxation, the pressure in the left atrium exceeds that in the left ventricle, causing the mitral valve cusps to open. Blood then flows through the open valve from the left atrium to the left ventricle during diastole. The initial filling is enhanced by the active relaxation of the ventricle, which helps to maintain a positive transmitral pressure. A peak in the mitral flow curve, called the E-wave, occurs during the early filling phase with normal peak velocities ranging from 50-80 cm/s [60]. Following active ventricular relaxation, the fluid begins to decelerate, and the mitral valve partially closes. In late diastole the atrium contracts and the blood accelerates through the valve again to a secondary, lower velocity peak, termed the A-wave, with normal E/A velocity ratios ranging from 1.5 to 1.7 [60].

Mitral valve fluid dynamics studies using magnetic resonance imaging (MRI) have shown that a large anterior vortex is normally present at the onset of partial valve closure as well as following atrial contraction [61]. Bellhouse [62] first suggested in an *in vitro* model that vortices generated by ventricular filling aid the partial closure of the mitral valve following early diastole, and that without the strong outflow tract vortices the valve would remain open at the onset of ventricular contraction. However, later *in vitro* experiments suggested that both flow deceleration and partial valve closure were due to

an adverse pressure differential in mid-diastole, even in the absence of a ventricular vortex [63]. Thus, although the vortices may provide additional closing effects in the initial stage, the adverse pressure gradient appears to be dominant in mitral valve closure. A more unified theory of valve closure includes the importance of chordal tension, flow deceleration and ventricular vortices, with chordal tension being a necessary condition for the other two [64].

2.4 Mitral Valve Mechanics

The mechanics of the mitral valve as a whole are complex, and limited studies on this subject have been conducted. The annulus, PMs, leaflets, and left ventricular wall are synchronized to maintain a balance within a dynamical environment [65], [66]. The overall force on the mitral valve leaflets is dictated by the pressure gradient across the valve. But within the constant motion of all its components, the actual force distribution and specific loading on the annulus, the chordae tendineae and PMs have not been fully described.

2.4.1 Leaflet Mechanics

The leaflet loading depends on the trans-mitral pressure, annular geometry and dynamics, coaptation geometry, chordae tendineae tension distribution, and contact forces between the leaflets. The curvature generated by the billowing of the leaflets during systole has been shown to be of mechanical importance since it reduces the stress on the anterior leaflet [40]. Additionally, a simplified computational model of the anterior leaflet has shown that the secondary curvature induced by the mitral annulus saddle shape is also a

stress relieving characteristic [8]. This model proposes that a saddle height to commissural diameter ratio of approximately 20% generates the minimum stress configuration for the central region of the anterior leaflet under systolic loading. In a non-linear fluid-coupled finite element model of the mitral valve, Einstein *et. al.* [67] predicted that the peak principal stress (254 kPa) during the cardiac cycle would occur in the belly of the anterior leaflet during peak systole (Figure 2.6).

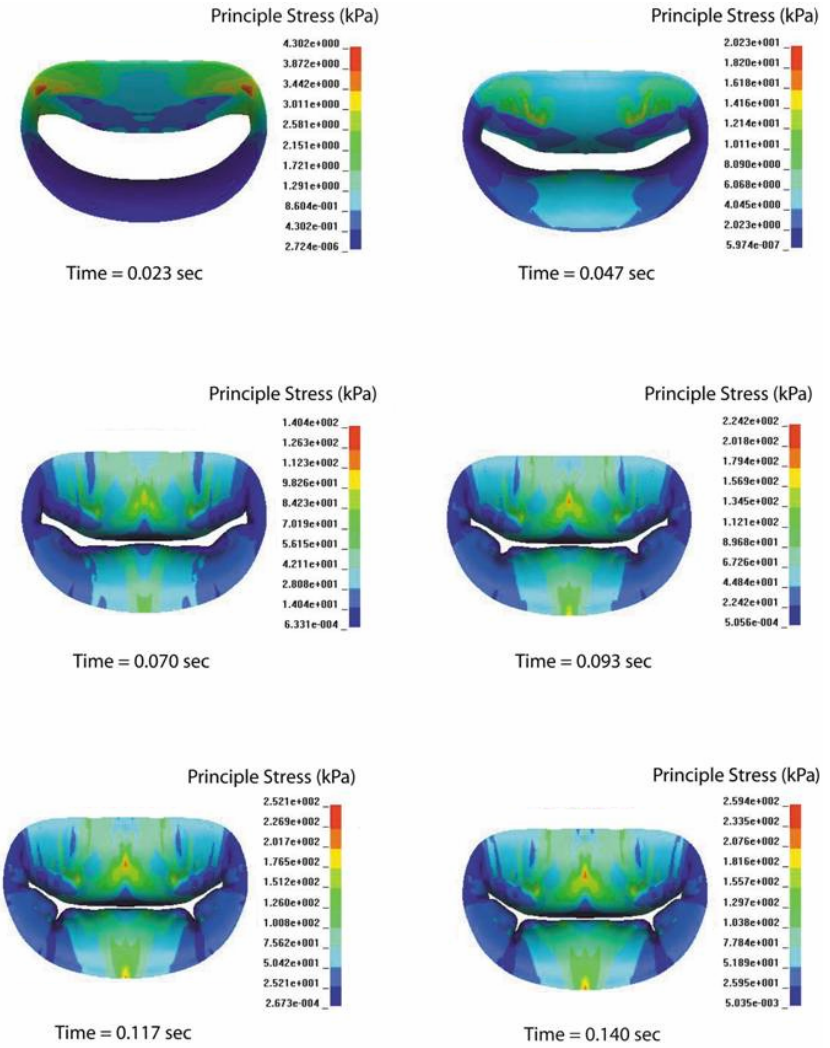

Figure 2.6. Time course of principal stress on the mitral leaflets and annulus during the cardiac cycle. Initially when the valve is fully opened the largest stresses are concentrated around the trigones of the mitral annulus. As the valve is loaded by the transmitral pressure the principal stress is transferred to the belly of the anterior leaflet during closure (Einstein, 2005).

Sacks *et. al.* [12] and He *et. al.* [13] described *in vitro* not only the material characteristics of the anterior leaflet under physiological loads, but also how the underlying collagen matrix influences valve mechanics during coaptation by controlling directional strain through collagen fiber locking. During valve closure the anterior leaflet stretched both in the circumferential and radial directions. Since the collagen fibers in the central region of the leaflet are arranged mainly in the circumferential direction, the leaflets became significantly stiffer in that direction as the collagen fibers uncrimped. A plateau at principal circumferential strains of 1.4 and radial strains of 1.2 indicated that the collagen fibers were uncrimped, thus limiting further deformation induced by transmitral pressure. No material creep was observed during this plateau at constant transmitral pressure. Peak strains persisted until the transmitral pressure decreased after which the material returned to its relaxed conformation. Similar strain behavior has been observed in the central region of the posterior leaflet [68] with some notable differences. The strain rates were lower in the posterior leaflet than those measured in the anterior leaflet, and a compressive strain at the beginning of valve closure was observed. Grashow *et. al.* [41] recently performed biaxial testing on the central region of the mitral valve anterior leaflet under physiological loading conditions. This study not only demonstrated the non-linear response and anisotropy of the central anterior leaflet, but also found that the material response was independent of strain rate. As a result, the material was described as quasi-elastic and anisotropic. All of these studies have been limited to the central regions of the mitral leaflets, which are relatively homogeneous. However, small angle light scattering [12] has demonstrated that other regions of the anterior leaflet have more complex

collagen fiber distributions. Therefore different material responses are expected for different regions of the leaflets.

2.4.2 Chordae Tendineae Mechanics

Leaflet coaptation geometry is highly dependent on chordal insertion and chordal tension distribution. Nazari *et. al.* [69] described theoretically how valve leaflet stress distribution is directly related to chordae tendineae distribution. During coaptation the load on the leaflets is transferred sequentially to increasingly larger chordae, leading to an optimal mechanical configuration during peak systole. He *et. al.* [70] defined a characteristic triangular structure between chordae that is fundamental to valve function. This triangle is formed when a smaller chorda branches off a larger chorda, and both insert into the leaflet to form a triangle between the two chorda and the leaflet. The disruption of this 'He' triangle can lead to mitral regurgitation. Lomholt *et. al.* [71], using an *in vivo* porcine model, showed that the dynamic tension on the secondary chordae was three times as large as that on the primary chordae with a peak systolic tension of 0.7 N for the secondary chordae and an average tension of 0.2N on the primary chordae. More recently, Jimenez *et. al.* [7] confirmed *in vitro* that the secondary chordae hold significantly larger loads than the primary chordae with remarkably similar forces to those found *in vivo* (secondary chordae=0.66N, primary chordae=0.22N). Recent studies have also demonstrated that the saddle shape of the annulus results in a more even distribution of loads among the various chordae tendineae [7]. Investigations of the tensile properties of the chordae tendineae have also shown a non-linear stress-strain relationship [72]. The maximum strain experienced by the anterior strut chord during the cardiac cycle

has been gauged at 4.29%±3.43%. The loading rate was higher at 75.3%±48.6% strain per second than the unloading rate at 54.8%±56.6% strain per second [73].

2.4.3 Annular Mechanics

The force from active myocardial contraction around the mitral annulus has not been directly measured. However, Einstein *et. al.* [67], using a non-linear, fluid-coupled, finite element model of the mitral valve, estimated that the largest stresses around the annulus ring were during late diastole and early systole in the trigonal areas (aprox 4.3KPa), which are the most rigid areas of the annulus (Figure 2.6).

2.4.4 Papillary Muscle Mechanics

Papillary muscle contraction is an essential component of the loading of the mitral valve. An *in vitro* study of porcine mitral valves showed PM loads on the order of 4.4N for the posteriomedial PM and 4.1N for the anterolateral PM [74]. However, this model did not simulate PM contraction, and therefore, these results represent only the force present in the PMs due to valve closure without accounting for annular motion, ventricular motion, or PM contraction. Papillary muscle material characteristics have also been studied using animal tissue. Pinto and Fung [75] demonstrated in unstimulated rabbit PM tissue samples that the relaxation function is independent of stretch ratio for strains under 30%. Creep tests with un-stimulated PM tissue have also shown large elongation (creep strain) under a constant load. Under cyclic uniaxial testing, unstimulated PM tissue reached a steady state hysteresis loop after preconditioning that was unaffected by strain rate, typical of a pseudoelastic response. For both uniaxial loading and unloading, the stress on un-

stimulated PM tissue varies as an exponential function of strain [76]. All of these characteristics describe the viscoelastic nature of the un-stimulated papillary muscle tissue.

2.5 Mitral Valve Malfunction

Mitral valve malfunction is normally described as a complex and often morbid condition that challenges cardiologists and cardiac surgeons alike. As the mitral valve's function is to control the flow between the two left heart chambers, pathologies may be classified in two different functional groups. The first group is stenosis, which describes the total or partial obstruction of the mitral orifice affecting ventricular filling. The second group is associated with malfunction during valve closure. When the mitral valve does not close adequately, the higher pressure in the ventricle during systole generates backflow jets into the atrium. This condition is called mitral regurgitation (MR). Mitral regurgitation may result from congenital malformation or disease, or, when in the absence of structural abnormalities of the MV, this condition is referred to as functional mitral regurgitation (FMR).

Both mitral stenosis (MS) and MR are products of several different causes and may exist simultaneously under specific conditions. Under MS or MR, the heart has to work harder as the efficiency of cardiac function is reduced. In the case of MS, stroke volume is reduced because of the inappropriate filling of the ventricle. On the other hand, the reduction in cardiac output associated with MR results from leakage through the valve. This leakage causes an increase in the regurgitation volume and thus a decrease in the

ejection fraction of the ventricle. Clinically significant regurgitation fractions are above 20% [65].

When the heart cannot compensate for the improper function of the mitral valve, cardiac output is reduced and therefore the body is subject to an inadequate supply of oxygen to the tissues. Patients with mitral valve disease will appear fatigued, present palpitation or suffer from chest pains [37]. Under severe pathological condition, where cardiac function as a whole is compromised, mitral valve disease may prove to be deadly.

2.5.1 Pathologies Which Directly Affect the Mitral Valve

There are several pathologies which directly affect the mitral valve by infectious processes, congenital abnormalities, or trauma. For several decades mitral valve disease was equated to rheumatic fever, as it was the most common pathology. Rheumatic fever causes the formation of small thrombi on the valves surface, leading to leaflet thickening or chordal shortening [38]. The combination of lesions in both the leaflets and chords may produce MS, MR or a combination of both. In myxomatous degeneration mitral valve tissue is directly affected, leading to MR. Myxomatous valves are characterized by floppy leaflets which have altered tissue structures [77-80]. Myxomatous tissue has been shown to have altered structure and directionality of the collagen fibers within the spongiosa. These structural changes lead to altered mechanical properties of the tissue. Thickening and enlargement of the leaflets and abnormal material properties of the chordae tendineae generally lead to regurgitation due to malcoaptation. Other diseases that may affect the mitral valve include bacterial endocarditis [81], Marfan's syndrome [1], and Whipple's disease [38].

The two main mechanisms through which the aforementioned diseases induce mitral regurgitation are leaflet malcoaptation and chordal rupture. These two conditions may independently or simultaneously affect the MV. Malcoaptation is generally a result of abnormal leaflet geometry and/or thickening of the tissue in such diseases as myxomatuos [77-80] degeneration or infective endocarditis [81]. Chordal failure is common in diseases such as myxomatous degeneration and rheumatic fever. Failure of the chords affected by these pathologies is associated with tissue degeneration [1], [38], [78-80]. Recent studies on myxomatous and normal MV tissue have shown that diseased chords fail at significantly smaller loads when compared to their respective normal counterparts [82].

2.5.2 Mitral Valve Malfunction Associated with Ventricular Disease

Several topological changes within the left ventricle have been associated with mitral valve malfunction [10], [11], [18-21] after ischemic heart disease or dilated cardiomyopathy. Alterations in the geometry or motion of the left ventricle result in changes in annular geometry/dynamics and repositioning of the papillary muscles (PM) within the mitral apparatus.

Changes in annular geometry and dynamics (2D area, 2D perimeter, saddle curvature, annular displacement) have been observed in patients with ischemic mitral regurgitation[11], [47] and different types of cardiomyopathies [19], [51], [53]. Additionally, recent studies both in animal models [21], [50] and human subjects [10] have quantified displacement of the PMs in pathologies such as ischemic mitral regurgitation and dilated cardiomyopathy. The results have shown that even subtle alterations in the position of the PMs during the cardiac cycle may lead to regurgitation.

The mitral annulus, as an important component of the mitral apparatus, has been related to several pathological conditions in which its size, dynamics, and shape may vary. Dilation is an important and common condition in the mitral annulus that has been related to several pathologies. Dilated cardiomyopathy, ventricular remodeling, and dilation after myocardial infarction have been associated with increases in annular area and subsequent regurgitation. Flachakampf *et. al.* 2000 used three-dimensional transesophagic echocardiography to reconstruct the mitral annulus of normal and pathological subjects. This study reported annular areas from 11.8±2.5 cm^2 in normal patients to 15.2±4.2 cm^2 in patients with dilated cardiomyopathy [19]. In an ovine model of normal and ischemic hearts, increases in annular area were observed by Dagnum *et. al.* 2000 after coronary occlusion [25]. Researchers measured the commissural-to-commissural and septal-lateral diameters of the mitral valves of these sheep. The results showed significant increases in both diameters, during diastole and systole. During systole, the mitral annulus commissure-to-commissure diameter was 33.7±1.4mm before ischemia and 34.6±1.7mm during ischemia. The septal-lateral diameter also increased from 24.3±1.2mm before ischemia to 27.4±1.8mm after ischemia [83].

Clinically, annular dilation is generally accompanied by other alterations of the mitral valve apparatus and the left ventricle (ventricular dilation, reduced ventricular contraction, PM displacement, etc.). Hence, *in vivo* it is not possible to quantify the individual contribution of annular dilation and these other factor to mitral regurgitation. To solve this problem, He *et. al.* 1999 designed an *in vitro* study that isolated the effect of annular dilation on mitral valve function. This study showed conclusively that dilating

the annulus by a factor of 1.75 induced mitral regurgitation without PM displacement, while PM displacement induced MR at significantly lesser levels of annular dilation [39].

Other more subtle changes in annular geometry have been observed in patients with mitral regurgitation. Changes in annular geometry (increased 2D-area, increased 2D-perimeter, decreased saddle curvature) were observed in patients with functional mitral regurgitation [18]. The patients in this study of FMR had as primary pathologies dilated cardiomyopathy and ischemic congestive heart failure. In this study there was a significant decrease in saddle height between normal and FMR patients. Flachskampf *et. al.* 2000 presented a clinical study of dilated and hypertrophic cardiomyopathy, and reported changes associated with annular shape, specifically annular saddle height. Saddle height decreased from 1.2±0.2mm in normal patients to 0.76 ± 0.1mm in patients with hypertrophic cardiomyopathy [19]. Therefore, changes in saddle height or curvature have been described as a possible cause of MR. Researchers based this hypothesis on the decreased septal-lateral diameter associated with saddle curvature, which may aid in valve closure.

Flachskampf *et. al.* 2000 and Toumanidis *et. al.* 1992, in independent clinical studies, showed decreased mitral annulus apico–basal motion in patients with mitral regurgitation [11], [19]. In Flackskampf's study, decreases of approximately 7mm in annular displacement were associated with dilated cardiomyopathy. The study by Toumanidis showed variations in annular motion associated with several cardiac pathologies that resulted in subsequent MR. In this study, annular motion was combined with annular area to calculate the volume traveled by the mitral valve during the cardiac cycle. Changes in this volume were directly associated to mitral regurgitation.

Although left ventricular dysfunction in most cases is accompanied by several alterations of the mitral apparatus, PM displacement or discoordination have been identified as major and direct contributors to MR. Dilated cardiomyopathy and ischemic heart disease are the pathologies most commonly associated with PM displacement.

Gorman *et. al.* 1997 used an *in vivo* ovine model of ischemic mitral regurgitation to observe geometrical alterations of the different components of the mitral valve after infarction [50]. This study showed that significant mitral regurgitation occurred even though the annular area increased only 9.2±6.3%. After infarction the posterior papillary muscle moved 1.4±0.6mm closer to the annulus while the anterior papillary muscle moved 0.9±0.7mm from the annulus. In addition, losses of contractility on the order of 2mm were also observed in the PMs. Papillary muscle displacement induced tenting and bulging of the mitral leaflets and subsequent regurgitation.

Bulged/tented leaflet geometries have been observed in other studies of MR where PM displacements on the order of 1 to 2.5mm induced significant MR[21]. These results describe the dynamic and fragile balance between the components of the mitral valve. The findings from the aforementioned studies of ischemic mitral regurgitation were confirmed by Nielsen *et. al.* 1999 and He *et. al.* 2003 using two different *in vitro* models. Both of these models showed how papillary muscle misalignment caused significant regurgitation in native porcine mitral valves [84], [85].

Tibayan *et. al.* 2003 measured ventricular curvature and principal strains in an ovine model of dilated cardiomyopathy using an array of radiopaque markers, under biplane video fluoroscopy. The results of this study showed increases of approximately 5mm in endocardiac ventricular curvature resulting in ventricular dilation and sphericity [20]. As

the PMs are attached to the ventricular wall, their bases are subject to these displacements. Dilated cardiomiopathy has also been associated with losses of PM contractility on the order of 2-3mm from clinical studies in humans [10]. The loss of contractility implies additional dislocation of the papillary muscles. In addition, dilated and hypertrophic cardiomyopathies have been linked to mitral regurgitation [11], [19], [51]. Therefore, mitral regurgitation resulting from cardiomyopathy has been associated to PM displacement induced by ventricular alterations. This regurgitation may increase if annular dilation is also present under the aforementioned pathology.

There are several mechanisms through which ventricular disease may affect mitral valve function. These mechanisms may be present independently or simultaneously. Ventricular remodeling or dilation affects both the annular and subvalvular components of the valve. Annular dilation due to ventricular dilation results in decreased coaptation length resulting from increased septal-lateral diameter. This increase in orifice area may lead to mitral regurgitation. The subvalvular apparatus is affected through PM displacement or more directly, in ischemic cases, through PM rupture. PM rupture is associated with tissue degeneration when the infarct affects the PM directly. PM displacement may induce mitral regurgitation through leaflet malcoaptation or chordal failure. As explained in the section above, malcoaptation in the form of leaflet tenting or prolapse may be derived from abnormal chordal force distributions resulting from the aforementioned PM displacement. The mechanism of chordal failure due to ventricular dilation is not well understood. Normal and pathological functional stresses have not been reported in literature. Therefore, there is no basis for comparative analysis with the

failure stress for chords which have been reported recently [56], [68]. Although these essential data has not been reported, complementary research has shown that dilated and ischemic cardiomyopathy patients have abnormal mitral tissue properties [86], [87]. Grande-Allen *et. al.* 2005 reported that chords from patients with dilated or ischemic cardiomyopathy were on average 16% stiffer [87]. Additionally, a case report by the same author describes how outer sheath rupture may precede complete chordal rupture in fibrotic mitral valve disease [88]. The presence of chordal tissue stiffening [87] and a gradual failure mechanism [88] suggest that chordal failure in ischemic or dilated cardiomyopathy patients may be due to a combination of tissue remodeling and accumulated damage.

2.6 Mitral Valve Repair After Ischemic Heart Disease or Dilated Cardiomyopathy

Repair has become the procedure of choice when dealing with most MV related pathologies [5]. The development of new techniques has improved patient survival and quality of life, however, current repair procedures are far from perfect. Recent studies have shown that within 5 years after the initial repair, significant levels of MR reoccur in most patients [23], [24]. These studies have also shown that most of the failures are due to a lack of durability of the initial repair (i.e. procedural related factors). Further understanding of mitral valve mechanics and function are essential to the solution of this growing medical problem.

Ventricular dilation/remodeling causes overall enlargement of the ventricle leading to alterations in the geometry of the mitral valve apparatus. Two mayor alterations are

normally present, annular dilation and papillary muscle repositioning. Of these alterations, only annular dilation is usually addressed, through ring annuloplasty. As a result of the substandard results associated with addressing an individual component during repair, the surgical community has started acknowledging the importance of simultaneously addressing several components of the valve in order to improve the long term results of mitral valve repair [32].

Although recent statistics show a favorable trend towards repair, only 36% of mitral interventions are repair procedures whereas 64% are replacements [6], leaving significant room for growth. The higher number of replacements is associated with the technical complexity and level of surgical expertise needed to perform a successful mitral repair.

2.6.1 Annuloplasty

There are several repair procedures associated with restoring the size and function of the mitral annulus. The most common procedure is the insertion of an annuloplasty ring. The ring is sutured around the mitral annulus restoring its size to some extent. Rings are described as rigid or flexible according to their flexibility, and complete or partial according to geometry. The first annuloplasty rings were rigid and complete. These rings are still used today and their latest versions include apical-basal curvature to restore the saddle shape of the mitral valve. Newer flexible rings have been designed as a result of studies which show the importance of annular dynamics in mitral valve function [7-9]. These rings try to maintain annular bending and contraction during the cardiac cycle, but, results on their effectiveness in maintaining annular dynamics are contradictory in the current literature [9], [25], [89-91]. Different groups have studied several brands of rings,

finding disparities in their dynamic characteristics [25], [89-91]. Most rings severely reduce mitral annular dynamics as they must have a somewhat rigid nature to hold the annulus from dilating again [25]. Partial rings were developed in order to prevent obstruction of the aortic outflow track since complete rings may alter the mechanical characteristics of the aortic root. When oversized leaflets are present it is commonplace to conduct annuloplasty and leaflet resection in parallel. During leaflet resection, the leaflet of interest is initially severed from the annulus, then a section of leaflet is resected, and finally the leaflet is resutured (Figure 2.7). These types of reconstructions are complex and leave vulnerable suture lines on the leaflet.

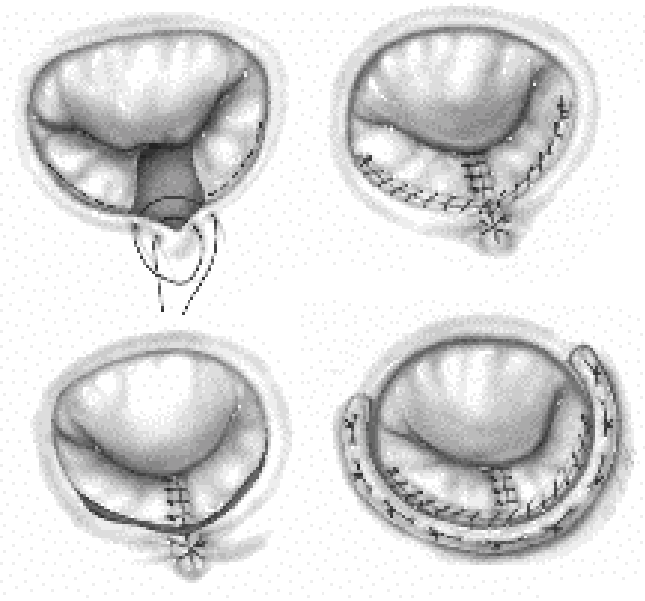

Figure 2.7. Diagram of an annuloplasty repair with posterior leaflet resection and annular placation (Courtesy of Dr. Joseph Gorman).

Currently, a significant degree of research is being conducted on the development of minimally invasive alternatives to annuloplasty. One of these techniques which are under development is based on introducing a device into the coronary sinus and using an anchoring system to reduce the size of the annulus [92].

2.6.2 The Alfieri Stitch

The edge-to-edge repair has shown to be a simple and effective adjunctive procedure when dealing with MV insufficiency [93]. However, the specific etiologies in which this tool may be used and its long term efficacy are still controversial [94]. In this procedure, the tips of the anterior and the posterior leaflets are sutured together to correct coaptation in prolapsing valves. The leaflets are generally sutured at the middle and a double orifice valve is created.

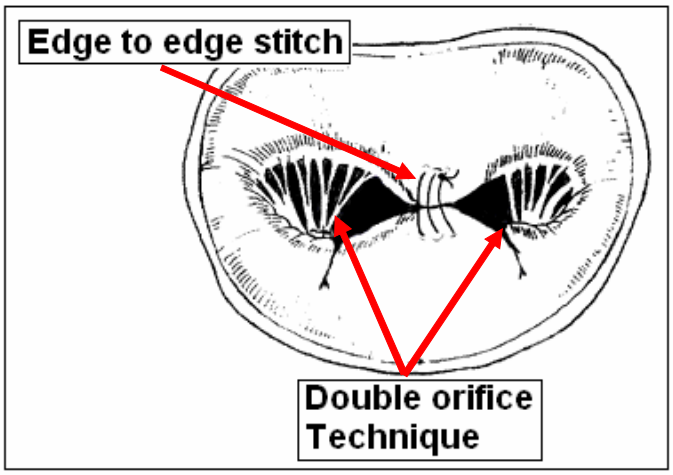

Figure 2.8. Schematic of the Alfieri repair using a single stitch in order to improve leaflet coaptation.

To improve the understanding of MV mechanics after the edge-to-edge repair several studies have recently been performed. Variables of valve function and mechanics such as regurgitation volume [94], [95], [97], [98], trans-valvular pressure gradient [95], [96], leaflet stress [99] and Alfieri stitch force [100], [101] have been studied. The pressure drop due to this double orifice has been studied by both in animals and in humans [95], [96]. The results from these studies demonstrated that the level of stenosis caused by the Alfieri stitch was

not clinically relevant. Timek *et.al.* 2003 demonstrated in an ovine model that the Alfieri repair does not prevent acute MR nor corrects valvular or subvalvular geometric perturbations without adjunct surgical procedures such as ring annuloplasty [97]. Clinical studies on the efficacy of the edge-to-edge technique without annuloplasty show suboptimal midterm results when compared with the results from edge-to-edge repairs with concomitant annuloplasty [98]. However, the need for concomitant annuloplasty may limit the development of new minimally invasive edge-to-edge repair alternatives [102], [103].

Studies by Nielsen *et. al.* 2001 and Timek *et. al.* 2004 demonstrated how annular size and geometry could statistically be correlated to Alfieri stitch force [100], [101]. Although edge-to-edge stitch failure is uncommon, Alfieri stitch force is an important parameter which may affect repair durability. Additionally, since less invasive techniques will require the use of mechanical devices such as clips to hold the leaflets together, knowledge of the loading to which these devices will be exposed is essential to their design.

2.6.3 Septal-lateral Annular Cinching

Although ring annuloplasty has proven to be an effective technique when dealing with mitral regurgitation, it abolishes normal mitral annular and posterior leaflet dynamics [25]. Recently, a novel surgical approach for ischemic mitral regurgitation in which a series of sutures are used to reduce the septal-lateral diameter of the annulus has been investigated [104-107]. As shown is Figure 2.9, five to six sutures are laid across the mitral annulus and then tethered to reduce its size. This technique has been shown to reduce ischemic mitral regurgitation by decreasing annular septal-lateral diameter (but not commissure-

commissure diameter), while maintaining normal annular and leaflet dynamics in animals [106], [107]. This procedure may represent a simple method for the surgical treatment of ischemic mitral regurgitation, either alone or as an adjunctive technique. The detailed mechanics and hemodynamics of the MV after annular cinching are yet to be studied, and thus require further investigation.

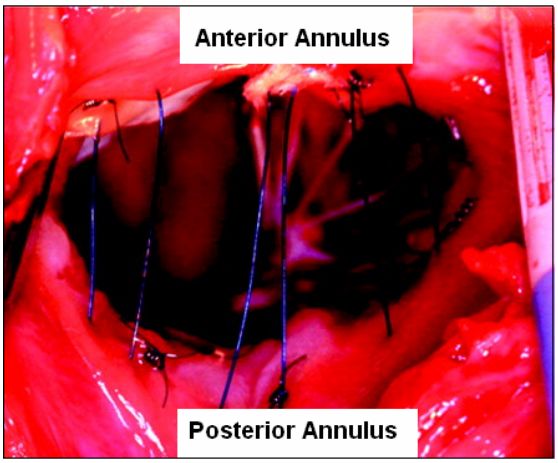

Figure 2.9. Photograph of the mitral orifice after septal lateral annular cinching [106].

2.6.4 Papillary Muscle Relocation

Surgeons and clinicians have proposed several procedures to correct MR due to PM displacement. Ventricular reconstruction procedures have been evaluated but are rarely used because of their invasiveness [33]. Recently, as a result of the need for correcting the relative position of the PMs after ventricular dilation, devices such as the Coapsy system [34], epicardial balloons, and the PM band have been developed. Additionally, ventricular restraints which may be used after ischemic events to limit remodeling of the ventricle are also under investigation [108]. Currently, none of the aforementioned solutions to PM relocation have been approved by the FDA.

2.6.5 Chordal Repair

Chordal repair of the mitral valve's subvalvular apparatus is divided into four different categories: cutting, transfer, replacement and shortening. Chordal repair is generally performed in order to correct MR associated with a prolapsing leaflet or chordal failure. The chordae that are most prone to failure are the marginal chords on the posterior side of the valve [1]. Although chordal repair procedures have evolved in recent years, they still present suboptimal results and in many cases are associated with re-operation [1].

Chordal cutting consists of severing both intermediate chords on a restricted leaflet in order to improve its coaptation. This procedure has been performed generally in animals [109] since it is in an experimental stage. Although a few clinical cases have been performed [110], recent reports describing limited efficacy and abnormal leaflet mechanics will probably restrict its clinical use [111].

Chordal replacement consists in using a single loop of suture in order to replace a failed chord. Chords are most often replaced with PTFE [112] sutures since polypropylene sutures may cause repair failure [113]. Autologous pericardium has also been used for chordal replacement in order to minimize any biological response from the body. Collagen based tissue engineered chords are currently under development and may someday be available for clinical use [114]. The major obstacle for chordal replacement is not material selection since PTFE sutures have shown good long term results [112]. The major obstacle during chordal replacement surgery is the adjustment of the length of the chord, since the surgeon is working on a passive and non-beating heart. Currently, more advanced techniques are being developed in order to cope with this problem [115], [116].

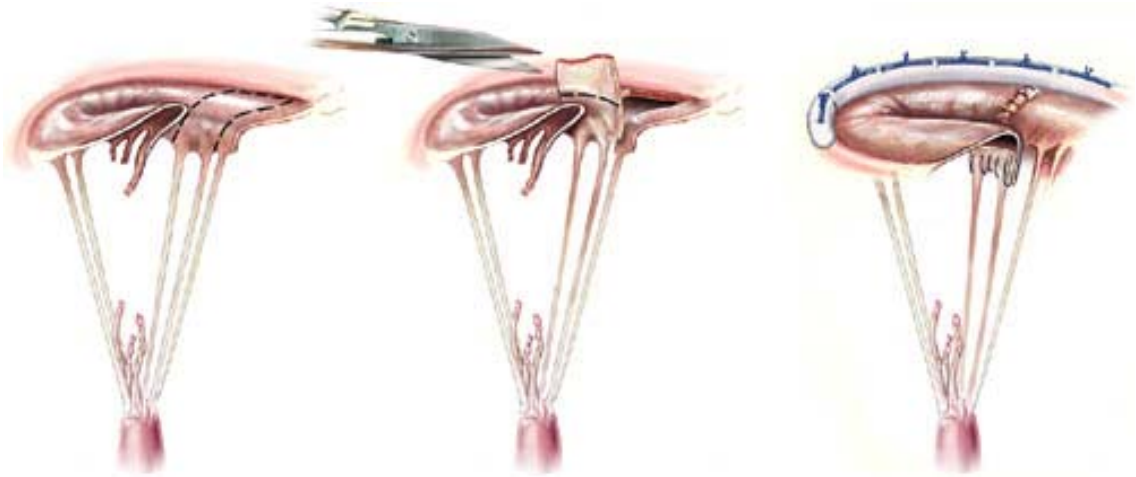

Figure 2.10. Chordal transfer for a prolapsed anterior leaflet due to chordal failure. (http://www.clevelandclinic.org/heartcenter/images/innovations/valveinnov)

Both chordal transfer and shortening are techniques commonly used for the repair of prolapsing leaflets. Prolapse may be due to chordal failure as presented in Figure 2.10 or elongated chords. Although posterior leaflet prolapse is more commonly associated with mitral regurgitation [1], anterior leaflet prolapse is the most complex to repair. For a prolapsing anterior leaflet, chordal transfer is performed by translating chords from the posterior leaflet to the free margin of the anterior leaflet. Similarly, for elongated chords, chordal transfer is normally preceded by the resection of the elongated structures. When dealing with elongated chords, chordal shortening may be performed instead of chordal transfer. To shorten the chords, a slight is cut into the PM and the excess length of the chords is tucked into this slight. The chords are then anchored with sutures and the slight is sutured shut. Because of substandard long term results for chordal shortening, chordal transfer is generally considered a better option [117], [118].

As described above, the mitral valve is a complex entity with hemodynamic, mechanic and biological functions. Pathological alterations to this system results in reduced quality

of life or life expectancy. Because of the substandard results with current mitral repair procedures, basic research on mitral valve mechanics in order to design more comprehensive approaches is required.

CHAPTER III

HYPOTHESIS AND SPECIFIC AIMS

At this time there is an important clinical need for improvement in MV repair efficacy and durability. Basic understanding of normal MV function and its alterations under pathological conditions is necessary for the design of repairs that restore, as much as possible, the normal function of the MV. In addition, reduction of altered or residual stresses after repair is a fundamental condition that may lead to increased repair durability.

To provide further understanding of MV function and mechanics under normal, pathological, and repair conditions, a set of studies has been conducted based on the following hypothesis: ***Alterations to the mechanics of the mitral annulus and subvalvular apparatus induced by ventricular remodeling lead to mitral regurgitation. Although current repair techniques may effectively restore hemodynamic mitral valve function, significantly altered valvular mechanics may still be present.*** To test this hypothesis the following specific aims were investigated:

Specific Aim 1 - ***To determine the normal function and mechanics of the native mitral valve within a physiological environment. .*** Although recently there has been significant progress in the study of normal MV mechanics, further understanding is still required. The objective of this section of the study was to better understand the function and mechanics of the MV and the interactions between its different components under normal

conditions. These measurements provided fundamental information, and were also used as a baseline to analyze alterations under pathological and repair conditions.

Specific Aim 2 - ***To measure changes in mitral valve function, chordal force/stress distribution, and coaptation characteristics under conditions induced by ventricular remodeling or dilation.*** Several topological changes within the left ventricle have been associated with MV malfunction after ischemic heart disease or dilated cardiomyopathy. Alterations in the geometry or motion of the left ventricle result in changes in annular geometry/dynamics and repositioning of the PMs within the mitral apparatus. A series of *in vitro* experiments were conducted emulating conditions found after ventricular remodeling. Functional and mechanical alterations were identified by comparing these measurements with those obtained in specific aim 1. Further understanding of the mechanical changes on the MV under pathological conditions provides not only fundamental information on the pathology itself but also may lead to the design of improved repair procedures.

Specific Aim 3 - ***To determine changes in mitral valve function and mechanics after annuloplasty and/or the edge-to-edge repair.*** To accomplish this specific aim a series of experiments were conducted simulating well established repair procedures. Local forces and stress/strain distributions were quantified under the aforementioned loading conditions. Understanding of MV mechanics after repair procedures will provide information on the causes of failure and deficiencies of current repair techniques. Data from the experiments encompassed in this specific aim may help to improve the reliability/durability of these commonly used MV repairs.

Accurate diagnosis and treatment of MV malfunction and the development of improved surgical strategies/techniques require a complete understanding of the normal MV structure and dynamics as well as the interplay of each of its components. This study utilized well-controlled *in vitro* experiments, allowing each component to be isolated in order to better identify its individual role in MV function. The significance of this research is associated with addressing the fundamental issues involving normal MV function and alterations resulting from specific pathologies or subsequent repairs.

CHAPTER IV

MATERIALS AND INSTRUMENTATION

4.1 Mitral Valves

Fresh porcine MVs from a local abattoir (Holifield Farms, Covington, GA, USA) fresh human MVs from Emory University and MVs from frozen human hearts provided by Corazon Technologies Inc. (CA, USA) were used in this study. Porcine mitral valve sizes were assessed using an annuloplasty ring sizer (Edwards Life Sciences, Irvine, CA, USA). The hearts from Emory University were obtained from heart transplant recipients with Institutional Review Board approval following the guidelines for the protection of study volunteers in research.

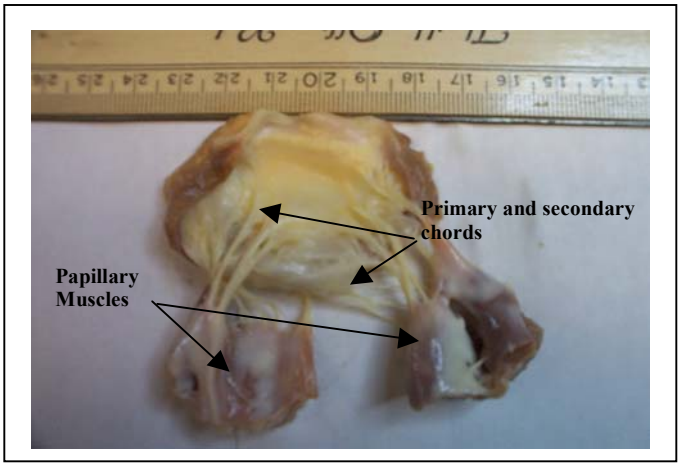

Figure 4.1. Intact human mitral valve with primary and secondary chordae tendineae and preserved papillary muscle sections.

Diseased mitral valves were excluded from this study. Valves with normal anatomical features and similar orifice areas were used. Experiments involving measurements of

chordae tendineae tension only used valves with simple (Type I and Type II) PM insertion patterns (Figure 2.6). The reasons for the selection according to PM structure were that complex PMs could not be appropriately coupled with the ventricle model, and that simple human papillary muscles are similar to porcine PMs. Valves were extracted from the hearts, preserving the complete mitral apparatus. (Figure 4.1)

During extraction, all chords that inserted into the leaflets or the annulus from the PMs were preserved. Chords which inserted from the PMs into the ventricle wall were severed. The extracted valves were preserved in saline solution (0.9%) to keep them moist during valve preparation and instrumentation. Since extraction, instrumentation, and experimentation could not be completed in the same day due to time constraints, valves were maintained in a refrigerator overnight following preparation. At least 15mm thickness was conserved in the PMs. This muscle volume allowed the valves to be coupled to the left ventricle simulator.

4.2 In *Vitro* Flow Loop

The *in vitro* experiments were carried out in the modified Georgia Tech left heart simulator. The simulator uses a pressure driven compressible bladder type pump, which is controlled and synchronized by a computer controlled pulse generating system. Compressed air is fed to the system main line at 40psi by a portable compressor (Thomas Ultra Air Pac, Model T-2820, Thomas Compressors & Vacuum Pumps, WI, USA). The air in the system is controlled by solenoid valves which are synchronized using a generic driver and a pulse timer unit (TeleVideo Model 910, Televideo Inc, CA, USA). This

controlled air supply is used to cyclically compress a silicon bladder, which provides the driving force for the loop by simulating ventricular pressures. The solenoid valves in the system were synchronized to maintain a total cycle time of 860ms, with systolic (compression) duration of approximately 300ms and diastolic (expansion) duration of 560ms.

Trans-mitral pressure was measured using a differential pressure transducer (model DP15-24 Tl, Valydine Inc., Northridge, CA) coupled to an amplifier/signal conditioner (model CD23, Validyne Inc., Northridge, CA). The trans-mitral flow rate was measured upstream from the valve using a cannular type electromagnetic flow probe (model EP680 Carolina Medical Instruments Inc. King, NC) connected to an analog flow meter (model FM501, Carolina Medical Instruments Inc. King, NC).

As shown in Figure 4.2, the left heart simulator is composed of a reservoir, an atrial chamber, a ventricular chamber and bladder, a resistance and connective tubing. The system is filled with 0.9% saline as a blood analogue. Initially the atrium is filled by fluid from the reservoir by gravity. The liquid column in the reservoir is maintained at a level which simulates atrial pressures. Fluid from the atrium flows into the ventricle through the native mitral valve. The bladder compression system then builds up pressure in the ventricular chamber forcing the fluid out through a mechanical aortic valve. Sections of tubing leaving the ventricle are compliant to simulate the aorta. Flow is controlled in this section of tubing using a manual clamp simulating circulatory systemic resistance. After the resistance, the fluid returns to the reservoir were it may initiate another cycle. This system is capable of producing physiologic and pathophysiologic flow and pressure

waveforms. The left heart simulator has been described in previous articles and documents [37], [39], [74].

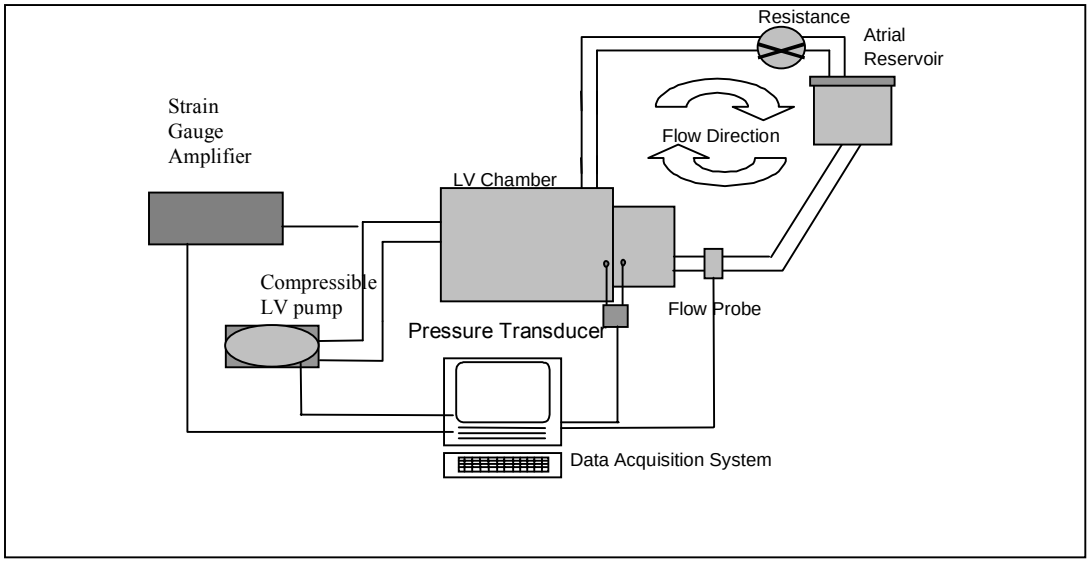

Figure 4.2. Schematic of the Georgia Tech Physiological Left Heart Simulator.

4.3 Ventricle Chamber

The left ventricle chamber of the simulator is a quasi-rectangular acrylic chamber (Figure 4.3). The transparent nature of the chamber allows optical access to appraise and record valve function. The upper frontal section of the chamber, which holds the aortic valve, forms a 135-degree angle with the frontal face of the chamber to reproduce the geometrical positioning of the mitral and aortic valves. A 27mm Bjork-Shiley convex-concave mechanical valve is used in the aortic position. The two syringes connected onto

the lid are used as air compliance in order to reduce fluctuations in the pressure waveforms.

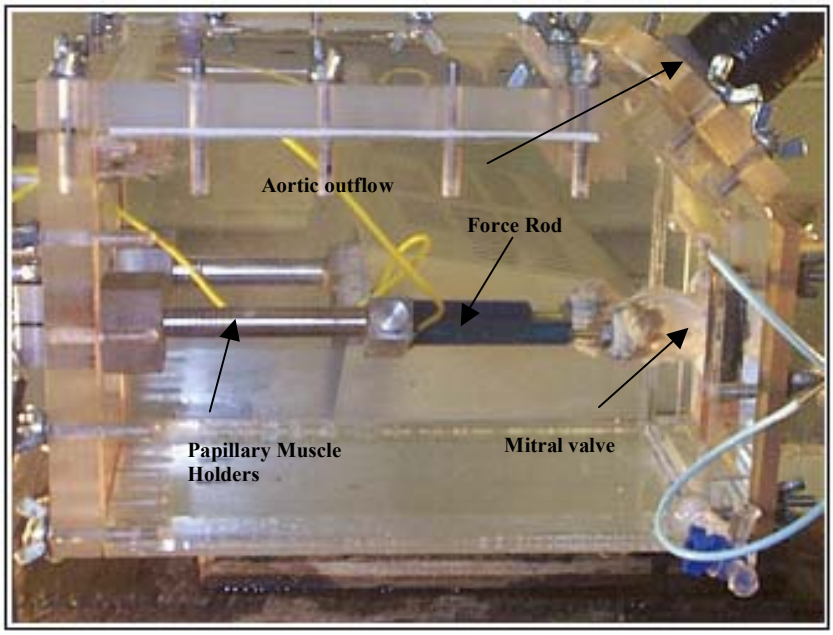

Figure 4.3. Photograph of the left ventricle chamber with papillary muscle positioning system and a native mitral valve (Courtesy of Morten Jensen).

The ventricular chamber has a papillary muscle holding system which allows three dimensional displacements.

4.4 Papillary Muscle Positioning System

As shown in Figure 4.4, the PM positioning system is composed of a main arm, a 90° pin gear system, an elevator, and a force rod. The main arm of the holding system slides through a tight fitting on the back plate of the ventricular chamber, allowing motion in the apical- basal direction and also rotation. The elevator system is coupled to the main

arm at 90-degrees. A 90° pin gear system is used to control the position of the elevator from outside the ventricle. A gear rotation rod inside the main arm may be rotated from outside the ventricular chamber in order to rotate the elevator screw throw the gear system. The apical-basal sliding of the main arm, its rotation, and the motion of the elevator allows this system to control PM position three dimensionally from outside the ventricular chamber.

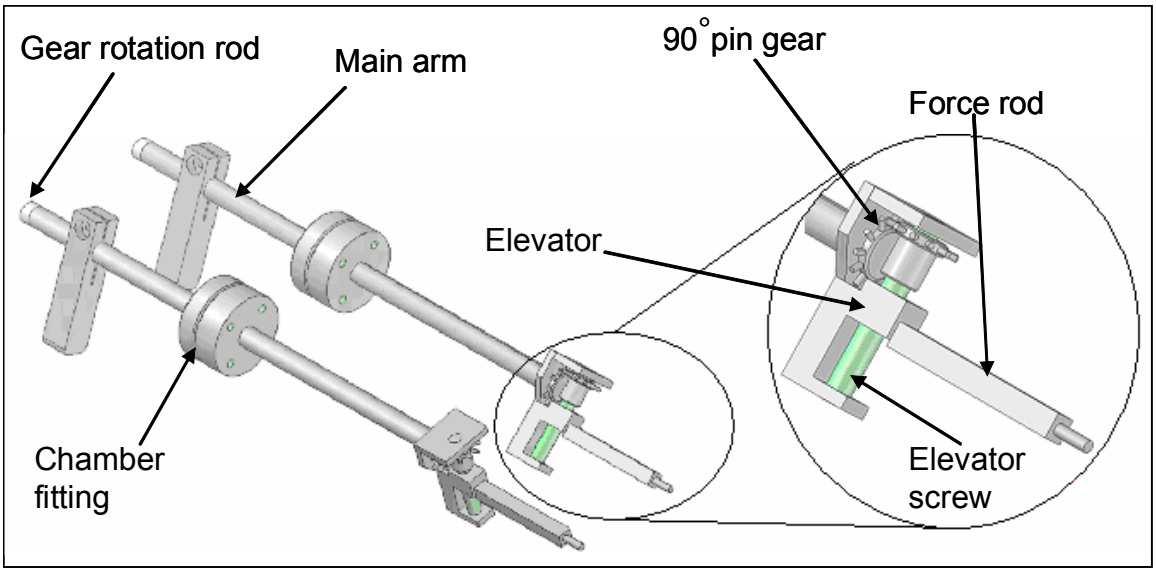

Figure 4.4 Assembly of the components of the papillary muscle positioning system.

Displacements in the apical-basal direction are evaluated directly using a ruler (±0.5mm) and measuring the distance which the main arm slides from the backboard from one position to another. Lateral and anterior-posterior displacements are calculated from the interaction of the elevator and the rotation of the main arm. The rotation of the main arm is measured outside the loop using a protractor (±1°). The exact displacement of the elevator is calculated from the rotation of the gear system (0.91mm/turn). Through simple trigonometric relations, the displacement in the elevator and the rotation angle required to attain exact positions may be calculated.

Using this system, exact displacements from a reference position may be obtained. An advantage of this system is that the PMs may be moved three dimensionally from outside the ventricular chamber. Details on the papillary muscle positioning system have been previously published [119].

4.5 Variable Shape Mitral Annulus Chamber (Flat – Saddle)

A variable annular shape atrial chamber (VASAC) was constructed to obtain the different annular geometries during the *in vitro* experiments (Figure 4.5). This chamber was used along with the Georgia Tech left heart simulator. Detailed blue-prints of this chamber are available in a previous publication [120].

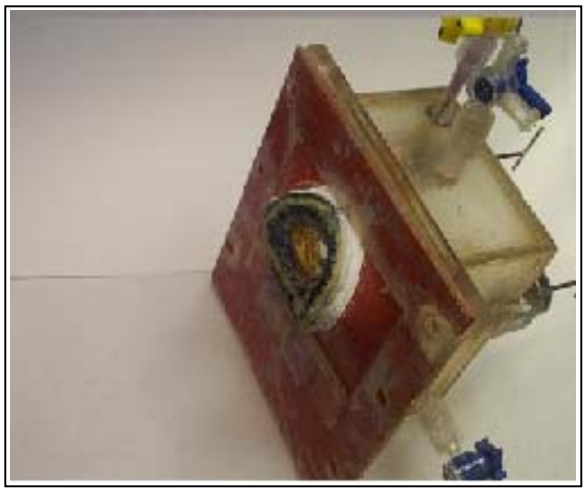

Figure 4.5. Photograph of the variable shape annulus chamber in the saddle configuration.

The atrial chamber was constructed of 3mm transparent acrylic plates, enabling visualization and echocardiographic imaging of the valve through a frontal window 5cm away from the annulus. The chamber has a rectangular volume of 229cm^2 and an inlet

diameter of 2.5cm. The annulus ring was composed of a multi-link chain which deformed three dimensionally (Figure 4.6), but retained an approximately constant 3-D perimeter

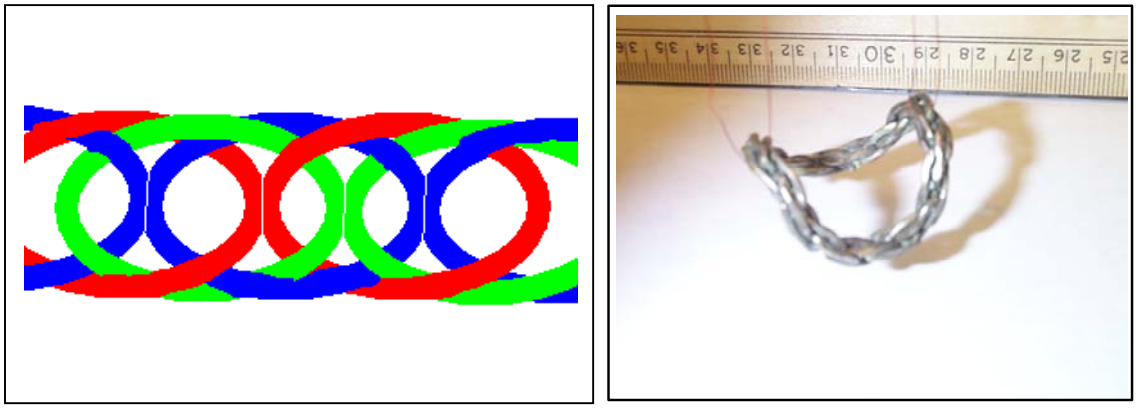

(a) (b)

Figure 4.6. (a) Schematic of the linking pattern of the chain used for this model. (b) Photograph of the multi-link chain forming a three-dimensional saddle geometry.

(maximum perimeter variation = 3%). The chain structure is characterized by a connection pattern where two sequential links (identified in Figure 4.6a by color) are joined together by two other individual links, which are also sequentially connected to each other. The chain had a perimeter of 11cm and each segment of chain was joined by three parallel links. In the flat configuration, the commissure-commissure diameter was approximately 3.6cm and the septal lateral diameter was 2.3cm. A 2cm section of chain links was fixed together using epoxy (Epoxy Bond, Atlas Minerals & Chemicals, PA,USA) to generate the D-shaped geometry characteristic of the mitral annulus orifice. Two straight control rods, connected at one end to the center of the commissural sections of the annulus, were used to modulate annular shape. These control rods slided through couplings in the frontal wall of the chamber. This mechanism was maintained water tight by O-rings. Moving the control rods in the forward direction pushed these sections of the

annulus forward, transforming the initially flat ring into a geometry similar to that of a saddle.

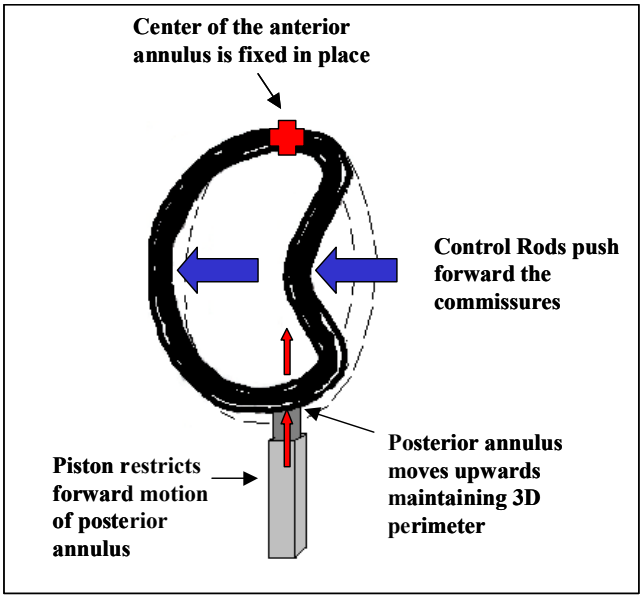

Figure 4.7. Diagram of the mechanism which shifts the shape of the annulus from a flat ring to a 3D saddle.

The annulus was held fixed at the middle of its anterior section and was connected to a small metallic piston at the midpoint of the posterior section (Figure 4.7). The piston was a 1.5cm long steel rod with a diameter of 3mm. The shaft was a hollow square bronze rod with a length of 2cm and an internal side length of 3.8mm. Therefore, the piston mechanisms provided a loose fit allowing easy motion of the piston. Because of this design, when the rods were pushed forward to generate the saddle the commissural section protruded into the ventricular cavity and the anterior section of the annulus was fixed in place (Figure 4.8). Since the perimeter was constant, the posterior section of the

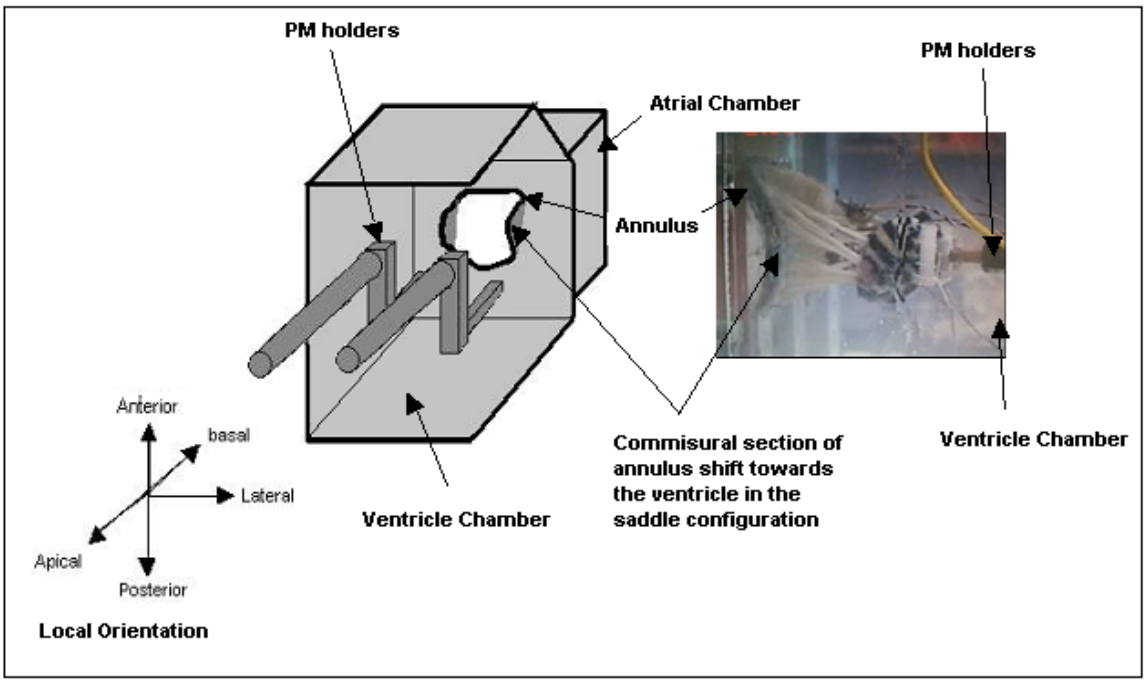

Figure 4.8. Schematic of the saddle shape configuration setup and local orientation.

annulus moved upward, reducing the septal–lateral diameter of the valve. The piston was used so that the posterior section of the annulus did not move apically, only septal-laterally. This variation in annular septal-lateral diameter is observed in the native mitral valve when going from a semi-flat structure in diastole to a three dimensional saddle in systole [18]. The whole ring is wrapped in a Dacron cloth allowing for extra support and the suturing of the valve.

The annulus was also sutured to a red silicon membrane (1.5mm thick) that deformed when shifting annulus shapes. This membrane kept a water tight seal around the annulus ensuring that fluid only went through the valve. The space behind the membrane in the saddle configuration was filled with plasticine to avoid membrane motions which may

promote inaccurate readings in the flow transducer. When in the flat configuration, the membrane bulged forwards because of the plasticine.

Annular geometry varied from a completely flat ring with an approximate orifice area of 6.8cm^2 to a saddle shaped geometry with maximum saddle height to commissural diameter ratio (SR) of 30%. The annulus model was capable of reproducing SR ratios observed clinically [18] [52]. The annular area and annular area variation were also within ranges observed clinically during the cardiac cycle [18] [52].

4.6 Variable Annular Size Atrial Chamber

To simulate variable mitral annular area (MAA), a variable size annular model, shown in Figure 4.9, was constructed. The annulus was constructed with a wire running through a metal spring covered with foam and Dacron enabling the valve to be sutured onto the model. The Dacron cloth covered ring was then sutured onto a membrane generating the characteristic D-shape of the mitral annulus. Annular size can be varied by turning a screw on the back of the chamber which tightens the wire forcing the spring to contract, reducing the posterior segment of the annulus. A flexible silicon membrane connecting the annular ring to the plexiglass of the atrial chamber allowed the annulus to restore its size when released. The annulus in the normal position had a 3.5cm commissural diameter and 2.5cm septal-lateral diameter (MAA= 6.86cm^2). Under dilation conditions the annular septal-lateral diameter increased to 3cm (MAA=8.22cm^2), and in the contracted position the annular septal lateral diameter was 2cm (MAA=5.50cm^2). The large annulus simulated a level of annular dilation found after acute ventricular

remodeling and the small annular area was selected by linearly extrapolating the normal and dilated conditions. A similar chamber was used in previous *in vitro* studies of mitral valve function [39].

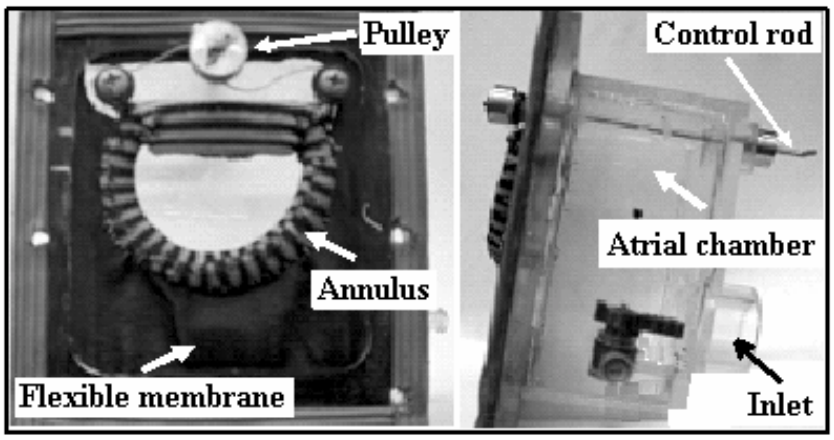

Figure 4.9. Photograph of the variable annular size atrial chamber and its components.

4.7 Strain Gauge Transducers and Force Rods

C-shaped transducers with strain gauges were used to measure the tension on individual chordae tendineae during the dynamic testing of the valve. The aforementioned c-ring transducers were constructed of a c-shaped brass ring 6mm in diameter, 2mm wide, and 0.5mm thick (Figure 4.10).

Figure 4.10. Photograph of a c-ring force transducer (scale in mm).

Two strain gauges (model: EA-06-031DE-350, Measurements Group, Raleigh, NC) were attached to the inner and outer surfaces of the ring, comprising a Wheatstone half-bridge. The overall weight of the transducer was less than 80mg. The strain gauges were coupled with an in-house amplifier box comprising the remaining half of the Wheatstone bridge. The transducers were coated to maintain electrical stability while testing inside the 0.9% saline solution media. The sensitivity (0.5 Newtons/Volt aprox.) and linearity (0-5 Newtons) of individual transducers was tested prior to and after each experiment. The minimal measurable difference in tension for these transducers was (0.5N/V*1.22mv = $6.1x10^{-4}$N) when coupled to the DAQ 1200 PCMCIA data acquisition card (National Instruments, TX, USA).The voltage baseline was zeroed immediately before dynamic testing. Applications of these c-rings force transducers have been presented in previous publications [66], [71], [120]. Details of c-ring construction, calibration, and function are shown in Appendix A.

Figure 4.11. Force rod mounted on the papillary positioning system.

The modified Georgia Tech left heart simulator used force rods (Figure 4.11), enabling the system to measure the total force (both tension and bending moments) applied on each papillary muscle. The rods were constructed of hollow brass tube with Kulite

semiconductor strain gauges (Type AGP 350-90, Teledyne Brown Eng.) arranged as Wheatstone bridges. The rods were coated with Conathane EN-12 Part B polyurethane casting resin, which maintained the electrical integrity of the rod when testing in saline solution. These rods were coupled to an independent in-house amplifier connected to a voltmeter (FLUKE 27, Everett, Washington). The sensitivity and linearity of the rods was tested before the experiments. This system was used as a reference ensuring a comparable force on both PMs and maintaining approximately the same force conditions when changing annular shape. The detailed construction and function of these rods has been described in previous publications [37], [74]. For the leaflet strain experiments described in section 5.4.2, a second set of modified force rods which use load cells (model S215, Strain measurement devices Inc, Meriden, CT) instead of strain gauges was constructed because of damage to the previously described initial set.

4.8 Echocardiographic Imaging and Video

A Diagnostic Ultrasound System SSA-270A with a 3.75MHz phased array transducer (Toshiba Corporation, Japan) was used to evaluate valve performance. Ultrasound gel (Aquasonic 10, Parker Laboratories, NJ, USA) was used between the atrial window and the ultrasound transducer to enhance the images of the valve. The imaging depth of the transducer was 5cm to 8cm from the valve's annulus and reached an additional 6-8cm downstream of the valve. Initially 2D-B-mode images of the mitral valve were acquired to observe the movement of the leaflets and closure characteristics. Image depth setting on the machine ranged from 12cm to 15cm, and gain was adjusted according to image

quality. 2D-B-mode images from the front of the atrial chamber are similar to those obtained *in vivo* from an esophageal view [37]. These images were important in assessing proper closure of the valve and location of the coaptation with respect to the septal-lateral diameter.

Color 2D-B-mode Doppler velocity mapping was used to monitor valve function and regurgitation. Color images of the flow through mitral valve were obtained at the same depth as the normal 2D-B-mode images. A scan window width angel of approximately 30 degrees was used for these images. The presence of bubbles and the absence of particle inside the fluid limited the quality of these images. Color Doppler images showed anterograde flow (away from the ultrasound probe) in blue and retrograde flow (towards the ultrasound probe) in red. Therefore, the presence of red jets across the valve while closed was characterized as regurgitation. Both echocardiographic images and lateral views of the valve in the simulator were stored on video. A digital camera (Sony Digital Handycam, Model DCR-TVR 310, Sony Corporation, Japan) was used to record these images.

4.9 High speed Camera System

In order to obtain the images for dual camera stereo photogrammetry, two high speed, high resolution cameras (Basler a504k, Basler Vision Technologies, PA) were used (Figure 4.12). Lenses (105mm f/2.8D AF Micro-Nikkor, Nikon, USA) were adjusted to achieve maximum contrast in the images. Each camera was connected to an individual EPIX high speed frame grabber card (PIXCI CL3SD Frame Grabber, EPIX Inc., USA)

which were synchronized using the EPIX software. Images were recorded simultaneously at 250 frames per second with an 8 bit gray-scale and a resolution of 1280 × 1023 pixels. A trigger signal was used to ensure that the cameras and pressure data were recorded in synchronicity.

Figure 4.12 Photograph of a Basler A504K high speed camera

4.10 Laser Micrometer

A single axis laser micrometer (model TLAser122, LaserLinc, Yellow spring, OH) was used to measure the diameter of the different types of chordae tendineae in order to calculate their cross-sectional area. The laser micrometer was coupled to a PCI interface card (model TLAser400, LaserLinc, Yellow spring, OH). This system has a resolution of 0.025µm within a functional range between 0.075mm and 22mm.

Figure 4.13 TLAser 122 laser micrometer (www.laserlinc.com)

4.11 Instrument Calibration

The trans-mitral pressure transducer was calibrated using a differential water column. Each chamber was calibrated independently and the voltage output of the pressure transducer amplifier was recorded and plotted against the water column differential pressure to obtain the sensitivity of the system. An example of a calibration curve for this transducer is presented in Figure 4.14.

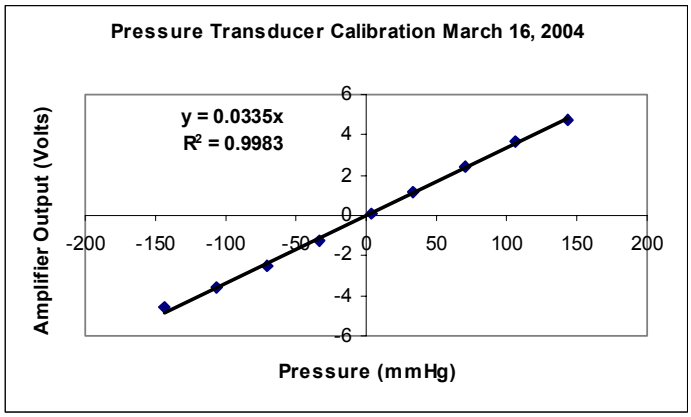

Figure 4.14. Calibration curve for trans-mitral pressure transducer.

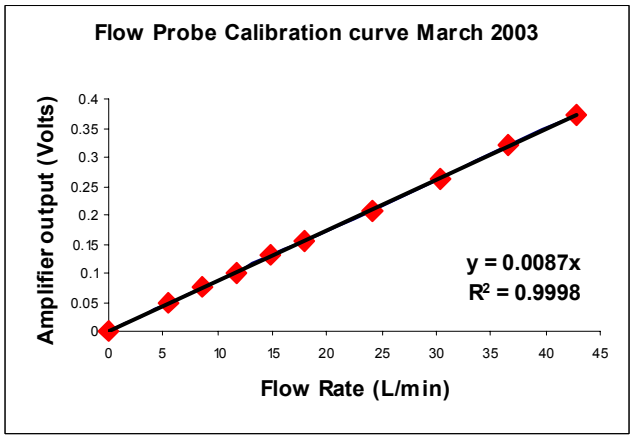

Figure 4.15 Typical calibration curve for the left heart simulator flow probe.

The flow transducer was also calibrated using a precision flow rotometer. Both the rotometer and the flow transducer were connected in series to a steady flow pump in a loop. Average flow in the system was varied and the output of the voltage of the flow amplifier and the rotometer flow were recorded. Figure 4.15 shows a typical calibration curve for the flow probe. Detailed calibration procedures for both the flow and the pressure transducer are available in a previous publication [37].

The c-ring tension transducers were calibrated before and after each experiment. After each c-ring was zeroed in the amplifier, known weights were suspended to induce a voltage variation. Output voltage was plotted against applied tension to obtain the

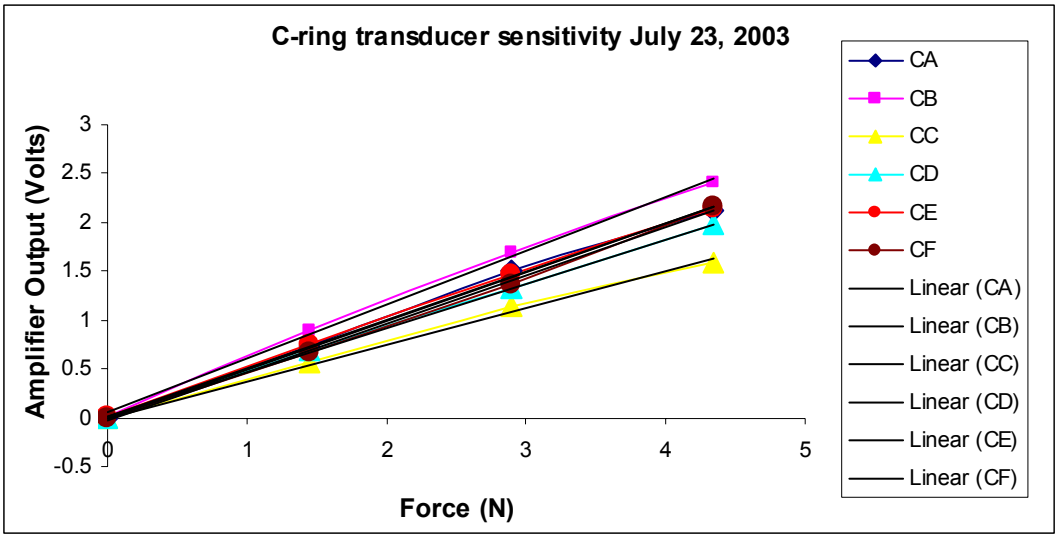

Figure 4.16 Sensitivity curves for c-ring force transducers (July 23/ 2003).

sensitivity of each c-ring (Figure 4.16). For the calibration of the PM force rods, known weights were suspended from the PM holder while monitoring the output voltage of the transducer. Details on calibration and behavior of the c-ring force transducers are presented in Appendix A.

CHAPTER V

METHODS

5.1 Preliminary Valve Instrumentation and Preparation

5.1.1 Measurements of Chordal Cross-Sectional Area

After valve extraction, the cross-sectional areas of the anterior strut chord, anterior marginal chord, posterior intermediate chord, stem of the posterior marginal chord, basal posterior chord, and commissural chord (Figure 5.1) were calculated.

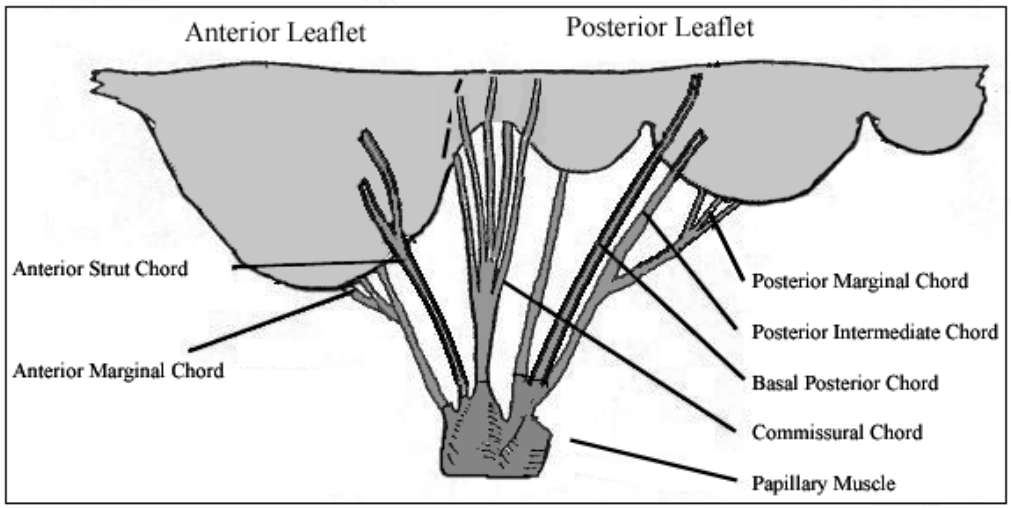

Figure 5.1. Diagram of an extended mitral valve identifying the selected chordae tendineae.

For these measurements the high resolution laser micrometer described in section 4.10 was used. Prior to each experiment the appropriate calibration from the Laserlinc proprietary software was loaded onto the system. Initially, the zero reference level was verified with only air in the path of the laser beam. Then the chorda tendinea of interest

was suspended vertically in the path of the beam. To suspend the chord in place a simple clamp on a standard laboratory mount was used. Special care was taken so the only load on the chord was its own weight. The chord was suspended by connecting a suture on one of its ends and holding the suture with the clamp (verifying that the chord was perpendicular to the laser beam). Then three measurements of chordal diameter were acquired: one 2-3mm away from the leaflet insertion, a second approximately in the middle (lengthwise) of the chord, and a final measurement near its insertion into the PM. Assuming a circular cross-section, the areas for the different regions of the chords were calculated.

5.1.2 Mounting of the Valve onto the Annular Model

As described in section 4.1, valves were extracted keeping the mitral apparatus intact. After valve extraction, the valves were kept in a refrigerator in saline solution overnight in order to preserve them moist and fresh before their instrumentation. Initially, the PMs from these extracted valves were wrapped with Dacron cloth maintaining the chordae distribution intact. This Dacron cloth was then sutured onto PM holding disks designed to attach to the left heart simulator. Each valve was then sutured onto the annulus of the appropriate atrial chamber model according to the specific experiment that would be performed (Variable annulus shape model, or Variable annular size model) using 3-0 sutures (braided silk, Ethicon, NJ, USA). During suturing, special attention was placed on preserving the annular perimeter to avoid dilation or contraction.

5.1.3 C-Ring Instrumentation for Chordal Force Measurements

For experiments which included chordal force/stress measurements, six c-rings were individually sutured onto the following chords: anterior strut chord, anterior marginal chord, posterior intermediate chord, stem of the posterior marginal chord, basal posterior chord, and commissural chord (Figure 5.1). It was not possible to attach all c-rings onto chords extending from a single papillary muscle because of spatial constraints that could cause c-ring entanglement (Figure 5.2). When suturing the c-rings onto the chords, 5-0 sutures (braided silk, Ethicon, NJ, USA) were used to fasten to the chord preventing the ring from slippage or detachment. Details of the attachment method are presented in appendix A.

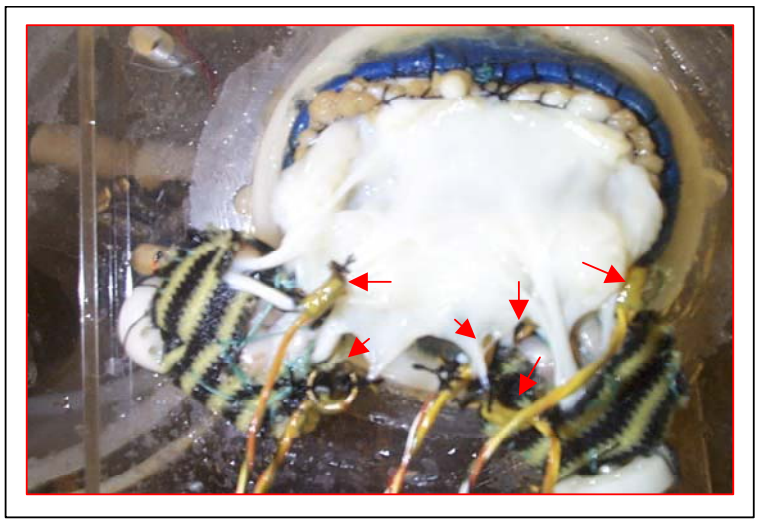

Figure 5.2. Mitral valve sutured onto an annulus board. Red arrows indicate c-ring force transducer. Four transducers are attached to chords extending from the anterior papillary muscle, while two are implanted on chords from the posterior papillary muscle.

5.1.4 Valve Preparation for Leaflet Strain Measurements

In order to use the marker technique to measure the strain on the anterior leaflet an array of ink markers was used. The surface of the leaflet onto which the markers would be placed was dried using a cotton swab. A thin needle was used to draw dots on the surface

of the leaflet. A 5x8 (circumferential x radial) marker array was sketched on the center of the anterior leaflet covering the whole radial distance from the annulus to 5mm from the tip of the leaflet as shown in Figure 5.3.

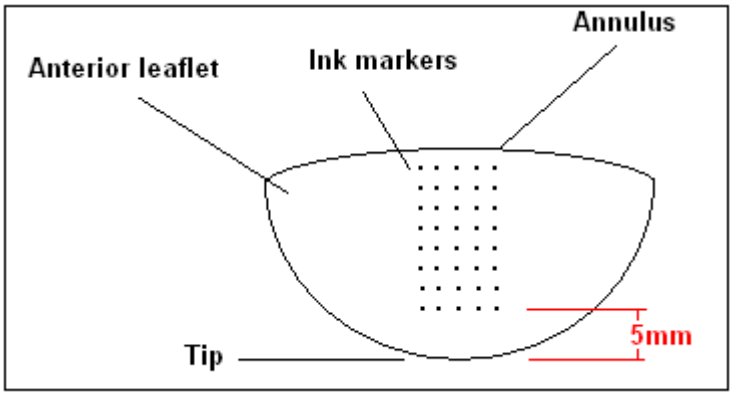

Figure 5.3. Diagram of the marker array used for the leaflet strain experiments.

The markers were allowed to dry for 2-5 minutes and then the valve was placed in saline solution so that the tissue would not dry out.

5.2 Experiments on the Normal Mitral Valve – Specific Aim 1

The objective of this section of the study is to better understand the function and mechanics of the mitral valve under normal conditions. These measurements will not only provide fundamental information but may also be used as a baseline to analyze alterations under pathological and repair conditions.

For these experiments 6 human (chordal force experiments) and 10 porcine mitral valves (leaflet strain experiments) were independently sutured onto the variable annular shape atrial chamber. As described in section 5.1.3, six chordae tendineae were instrumented with c-ring force transducers. The variable annular shape model was then coupled onto

the Georgia Tech Left Heart Simulator. The c-ring cables were connected to the in-house c-ring amplifier box using the same channels they were calibrated with. The PMs were attached to the force rods and the left heart simulator was then filled with 0.9% saline solution. All transducers and c-rings were zeroed and connected to an in-house interface box; which was then connected to a laptop computer.

The mitral annulus was then set to a physiological saddle height to commissural diameter ratio (SR=20%) using the control rods in the atrial chamber. The PMs were then placed in the defined as normal position (Figure 5.4). The normal position was defined by [84].

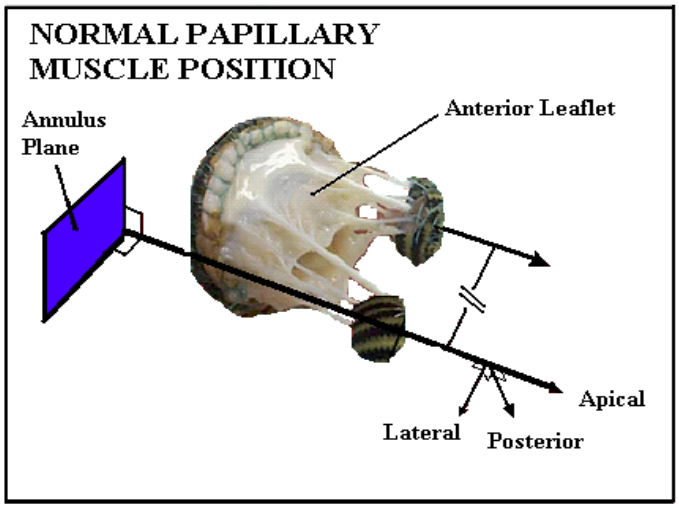

Figure 5.4. Descriptive diagram of the normal papillary muscle position

- *Basal-apical location*: The papillary muscle rods were moved towards the annulus to a point where slack was observed in all the chordae tendineae. The papillary force rods were zeroed at this location. Each force rod was pulled backwards until a change in voltage of 0.02volts (0.09Newtons) was achieved for that particular rod. This was the minimal significant change that may be observed by the system. This defined a position with no slack or apparent tension on the chordae tendineae.

- *Lateral Location*: The papillary muscles arranged parallel to each other and directly aligned with the valve's annulus on each commissure. The commissural chords should insert perpendicularly to the annular plane.
- *Septal-lateral location*: The rods were moved septal laterally until an even extension of the commissural chords inserting into the annulus was observed. Normally, this point was a couple of millimeters below the annular height midpoint.

Valve function in the normal PM position was confirmed under pulsatile flow by observing appropriate leaflet coaptation using 2D echocardiografic images, and color Doppler images of the flow. Valve function was filmed through the ventricular chamber using the digital camera.

The simulator ran under physiologic conditions with the valve in the normal position (cardiac output: 5 l/min, peak trans-mitral pressure: 120 mmHg, heart rate: 70 BPM, systolic duration: approx. 300ms). Mitral flow, chordal force, and pressure curves were saved on a laptop computer for offline processing. Data representing ten cardiac cycles for each variable was stored. Dual camera photogrammetry images were obtained for a single cardiac cycle.

5.3 Alterations to Mitral Valve Function and Mechanics Associated with Papillary Muscle Repositioning – Specific Aim 2

After ventricular dilation associated with conditions such as ischemic heart disease and dilated cardiomyopathy several changes to the geometry of the mitral apparatus have been observed. Under these pathological conditions annular dilation, annular flattening,

and papillary repositioning are simultaneously present. Previous research showed the independent effect of annular dilation [39] on valve function and/or mechanics. Further studies have shown the combined effects of annular dilation and PM repositioning [21], [39] on valve function and mechanics. Therefore, the present section of this study was aimed at understanding the independent and combined effects of annular flattening and papillary muscle repositioning on valve function and mechanics.

Six human mitral valves and five porcine mitral valves were used in this section of the study. After acquiring the initial baseline parameters described in section 5.2 each valve was then tested again in seven other papillary muscle positions. The reference for all these displacements was the normal PM position [84].

Table 5.1. Vectorial decomposition for the different papillary muscle positions.

Papillary Muscle Position	Apical Displacement (mm)	Lateral Displacement (mm)	Posterior Displacement (mm)
000	0	0	0
005	0	0	5
050	0	5	0
055	0	5	5
500	5	0	0
505	5	0	5
550	5	5	0
555	5	5	5

All displacements were symmetrical; therefore both PMs were displaced equally to reach each position. Only symmetric positions were tested because it was not possible to attach all six c-rings on the same PM; therefore, special care was taken on having the same average force on the PM in the normal position. The seven different positions are presented in Table 5.1, with their corresponding vectorial displacement from the normal position. A schematic of the spatial reference system is presented in Figure (5.5).

Mitral flow rate, transmitral pressure, chordal force, video, and Doppler recordings were performed for all the previously described PM positions using the same physiological flow conditions (Cardiac output: 5 l/min, peak trans-mitral pressure: 120 mmHg, heart rate: 70 BPM, systolic duration: 300 ms). Data were recorded for ten cardiac cycles and subsequently averaged offline.

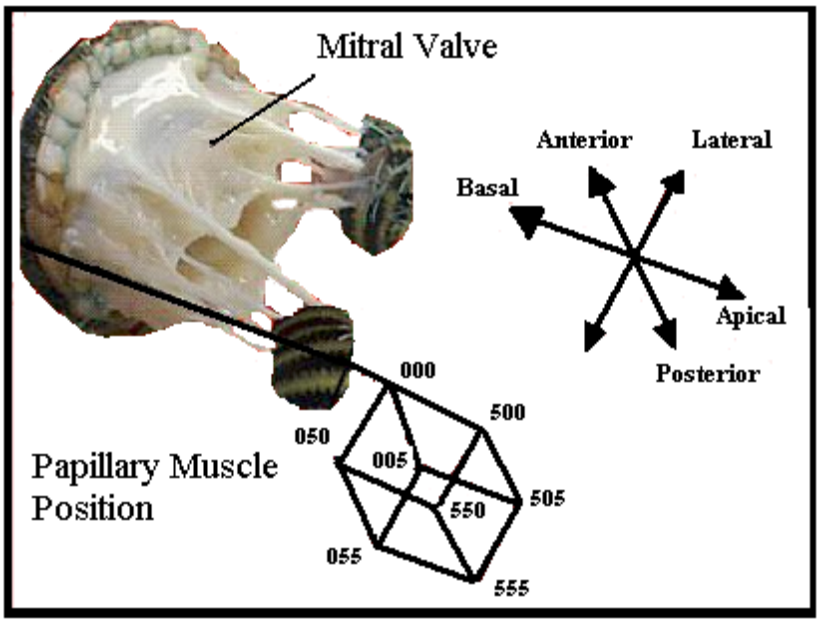

Figure 5.5. Spatial reference system based on the normal papillary muscle position. The edges of the cube represent the eight different experimental positions used in the study.

5.4 The Repaired Mitral Valve – Specific Aim 3

5.4.1 Mitral Valve Mechanics and Function after the Alfieri Repair

To improve the understanding of mitral valve mechanics after the edge-to-edge repair several studies have recently been performed. Variables of valve function such as regurgitation volume [94-95] and trans-valvular pressure gradient have been studied in the past [95-96]. The first parameter describes the effectiveness of the technique in alleviating mitral insufficiency. The second parameter describes the level of occlusion caused by the

presence of the stitch during diastole, and may be used to calculate the effective orifice area (EOA) of the valve. Other variables of valve mechanics after the edge-to-edge repair such as leaflet stress [99] and Alfieri stitch force (F_A) [100-101] have also been studied. Although edge-to-edge stitch failure is uncommon, these are important parameters which may affect repair durability. The present section of this study aimed to expound the relation between F_A and variables such as annular area, trans-mitral pressure, and mitral flow rate in an *in vitro* model of mitral valve function. The *in vitro* approach will allow control over the variables of interest and thus provide an understanding of their individual contributions to F_A. Additionally, effective orifice area and regurgitation volumes will also be determined in order to assess the efficacy of the edge-to-edge procedure in the studied annular conditions.

Data were obtained from 15 fresh porcine MVs with normal anatomical features and similar orifice areas ($6.8\pm0.3cm^2$). Ten of these valves were used for the pulsatile experiments and five were used for the steady flow experiments.

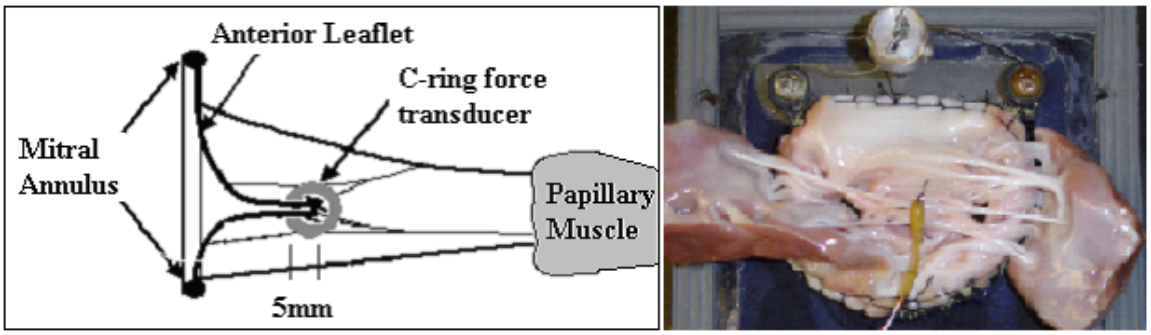

Figure 5.6. (Left) Schematic of a C-ring force transducer mounted onto the mitral valve. (Right) Photograph of c-ring transducer mounted on a mitral valve.

Each MV was sutured onto the variable size annular model with 3-0 suture. Holding disks were sutured to the PMs allowing the valve to be mounted onto the left heart

simulator [13], [37], [39]. A C-ring force transducer was then sutured onto the anterior and posterior leaflets 5mm from their tips as shown in Figure 5.6. This assembly was then coupled onto the left heart simulator.

5.4.1.1. Steady Flow Experiments

For the initial experiments a steady flow pump was adapted to the Georgia Tech Left Heart Simulator instead of the pulsatile system described earlier. Forward flow rates across the valve were controlled by increasing the resistance in the loop using a clamp, and by electrically controlling the pump speed with a voltage regulator.

Flow rates were monitored with the electromagnetic flow transducer of the left heart simulator described earlier. The pressure drop across the valve and F_A were monitored at the different mitral flow rates. The pressure drop across the valve was measured using a manometer and F_A was measured using a C-ring transducer. Saline solution (0.9%) was used as the blood analog fluid and the PMs were set to their normal position [84].

To obtain a baseline for the EOA of the MVs, initial experiments were carried out at flow rates from 0L/min to 30L/min in 5L/min increments, with the valve in the different annulus configurations, but without the edge-to-edge repair. After baseline EOAs were measured for the different annuli, the force transducer was sutured onto the leaflets. The C-ring was zeroed under static flow conditions. F_A and pressure drop across the MV were measured for flow rates from 0 to 20L/min in 2L/min intervals. A final measurement was also obtained at 30L/min.

5.4.1.2 Pulsatile flow Experiments

The mitral valve with the C-ring force transducer was mounted onto the Georgia Tech Left Heart Simulator. The valve was placed in the defined normal PM position and the C-ring was zeroed under static flow conditions. The PMs were then displaced 5mm apicaly, 5mm laterally, and 5mm posteriorly from the normal position. The simulator was operated under physiologic conditions (heart rate: 70 beats/min, systolic duration: 300ms). F_A data were collected at peak transmitral pressures of 100 mmHg, 120 mmHg, and 140 mmHg, while maintaining a cardiac output of 5L/min. Data were also obtained at cardiac outputs of 4L/min and 6L/min at a peak transmitral pressure of 120mmHg. All of these measurements were acquired at three annular sizes: dilated, normal, and contracted. The valves were initially tested in the dilated annular configuration. Annular size was then decreased to the normal and contracted configurations. Mitral flow rate, transmitral pressure, and F_A data were acquired on-line over ten cardiac cycles, and subsequently averaged offline.

5.4.2 The Effects of Annuloplasty Ring Geometry on Anterior Leaflet Strain.

The normal geometry and material properties of MV are thought to elicit an optimal stress distribution. Previous research has shown to some extent that the 3D saddle shape of the native MV may reduces stresses on the anterior leaflet [8] and produces a uniform force distribution among chordae tendineae [7]. This optimal configuration is lost after alteration in the annulus and subvalvular apparatus associated with different pathologies. In order to improve repair durability it is necessary not only to correct valve function, but also to reduce residual or altered stresses associated with the specific repair technique.

Annuloplasty is the most common component of surgical procedures designed to correct MR by reducing the size of a dilated annulus or stabilizing it's geometry after a reconstruction procedure. In the current market different shapes of annuloplasty rings are available. One of the geometrical parameters which vary within the different rings is the saddle height. A simplified finite element model [8] of the mitral valve showed that systolic leaflet stress may depend to some extent on saddle curvature. Therefore, the objective of this section of the study was to quantitatively associate changes in saddle curvature to changes in the strain field of the central region of the anterior leaflet.

Ten porcine mitral valves of similar orifice areas ($6.9\pm0.4cm^2$) were used for these experiments. The mitral valves were sutured onto the variable annular size atrial chamber as described in section 5.1.2. Ink markers were drawn onto the central region of the anterior leaflet as described in section 5.1.4 and figure 5.3. The atrial chamber containing the mitral valve was the coupled to the Georgia Tech Left Heart Simulator.

Strains on the central regions of the anterior leaflet were quantified using the marker technique [12-13]. The marker technique uses dual camera stereo photogrammetry (DSCP) to obtain pairs 2D images of markers or targets. The 3D spatial coordinates of these markers are then calculated using a direct linear transform. The strain distribution and principal stretches are then computed from these 3D coordinates.

For the DCSP imaging, two high speed cameras (section 4.9) were positioned at an angle of 30 degrees from each other in front of the atrium chamber window (aprox. 25cm from window) to capture the ink markers on the atrial face of the leaflets. This camera configuration allowed for the imaging of the whole mitral orifice during the entire cardiac cycle. Light and lens were adjusted in order to obtain optimum contrast and focus of the

markers in the images during valve closure. Synchronous images from both cameras (250 fps at a resolution of 1280x1023 pixels) were acquired for one cardiac cycle under physiological pulsatile flow conditions (Cardiac output: 5 l/min, peak trans-mitral pressure: 120 mmHg, heart rate: 70 BPM, systolic duration: 300 ms). The images from the cameras were synchronized to the pressure a flow signals through a digital trigger. DSCP images for a single cardiac cycle, and mitral flow and transmitral pressure data for ten cardiac cycles were recorded.

Initial experiments were carried out with the annulus in the flat configuration. The experiment was then repeated at saddle heights of 3mm, 6mm, and 9mm corresponding to saddle height to commissural diameter ratios of 10%, 20%, and 30%, respectively. When changing from one annular configuration to another, the PMs were displaced apically to compensate the forward motion of the commissural sections of the annulus. In all positions special care was taken so that both papillary muscles held the same load (0.2N). For all the different saddle configurations DCSP images for a single cardiac cycle and mitral flow and pressure signals for ten cardiac cycles were recorded.

5.5 Data Acquisition and Analysis

5.5.1 Transmitral Pressure, Mitral Flow, C-Ring Force

To acquire data, the left heart simulator uses an in-house interface box, which receives analog voltage signals from the transducers. The interface box transfers these signals to a PCMCIA data acquisition card (Daq-card 1200, National Instruments, TX, USA). This card has eight different channels, which may be synchronized by a trigger. During the experiments one channel was used for flow, a second channel was used for pressure and

the other six channels were used transferred readings from the c-ring force transducers. DAQ-ANAL 2.1, an in-house data collection program based on LabVIEW 5.0, was used to store the flow, pressure, and c-ring force curves on a laptop computer. This program acquired data every 2ms from the eight channels. The program automatically stored data for ten cardiac cycles for each variable. The curves for the ten stored cardiac cycles were averaged and analyzed offline using the data analysis tool of DAQ-ANAL, which generated excel spreadsheets. The data analysis tool also allowed the user to delete curves that appeared to be deficient before averaging. The data acquisition system and the Daq-Anal 2.1 software have been described in detail in previous publications [37], [39].

Excel was employed to organize, analyze, plot, and store the averaged curves of each of the recorded variables. Macros in Excel were used to correct the diastolic baseline for all the chordal force curves and find the peak values for each variable during the cardiac cycle.

Mitral flow rate, transmitral pressure and c-ring force were obtained directly from transducer readings with their associated calibration. Diastolic pressure drop across the valve was directly read from the manometer in the static flow experiments and from the pressure transducer in the pulsatile experiments. Mitral regurgitation volume was calculated by integrating the systolic negative volume from the flow curve, which included both the closing and leakage volumes. Chordal stress (engineering stress) was calculated by dividing the measured chordal force by the cross-sectional area of the corresponding chord. In order to calculate effective orifice area for the experiments described in section 5.4.1 the following formulas were used:

Steady flow experiments

$$EOA = \frac{Q}{\sqrt{\frac{2\Delta p}{\rho}}} \quad \text{(Equation 5.1)}$$

Pulsatile flow experiments

$$EOA = \frac{\bar{Q}}{\sqrt{\frac{2\Delta \bar{p}_{rms}}{\rho}}} \quad \text{(Equation 5.2)}$$

EOA = Effective orifice area (cm^2)
Q = Flow rate (cm^3/s)
Δp = pressure drop ($dynes/cm^2$)
1mmHg = 1333 $dynes/cm^2$
ρ = density of saline
$\bar{Q}$ = mean forward diastolic flow (cm^3/s)
$\Delta \bar{p}_{rms}$= Average root mean square diastolic pressure drop ($dynes/cm^2$)

5.5.2 Leaflet Strain Acquisition and Analysis

The marker technique uses 2D images from dual camera stereo photogrammetry (DSCP) to obtain the 3D spatial coordinates of markers using a direct linear transform. The strain distribution and principal stretches are then computed from these 3D coordinates.

Images from the two high speed cameras described in section 4.9 were acquired as a sequence of TIFF files using EPIX high speed frame grabber cards (PIXCI CL3SD frame grabber, EPIX Inc., USA). The images from the frame grabber were synchronized to the DAQ-ANAL 2.1 data collection tool through a 5V trigger signal, allowing simultaneous acquisition of images from the cameras and flow and pressure information from the corresponding transducers. After the DCSP images were acquired, an additional image of a calibration cube (10mm on edge) was acquired with each camera. The cube was placed in the area of the markers so that the seven corners were clearly observable from both cameras.

Following image collection, a commercial digitizing software package (Sigmaplot; Jandel Scientific, San Rafael, CA, USA), was used to determine the x, y pixel coordinates of each marker from the sequential 2D images. A direct linear transform method implemented in Math Lab 7.0 was used to recover the 3D spatial reconstruction from the recorded 2D images utilizing the calibration cube images as reference [12], [119], [121-122].

Biquadratic finite element interpolation was used to perform the surface fit to the resulting 3D marker array [12]. The principal stretches, areal stretch, principal angles, and surface curvatures were calculated for the area of interest in the reconstructed surface.

The marker technique, its different steps, and the software used to calculate the strains on the anterior leaflet of the mitral valve have been described in detail in previous publications [12], [13], [119]. The accuracy of the marker technique has also been reported [12]. The surface fitting technique was able to fit the spatial positions of calibrated markers very well (R^2>97%). The net spatial accuracy was determined to be ±0.1mm, which lead to errors of 0.01±0.005 in principal stretch and 0.026±0.01 in areal stretch.

The aforementioned data analysis steps for the marker technique were used on the DCSP images of the eight mitral valves. The complete array of (5X8 markers) was not visible during the entire cardiac cycle for all valves. Marker array size was generally diminished in the radial direction since leaflet coaptation covered some of the markers. Therefore, the largest array which was visible during the entire cardiac cycle was used. The minimum marker array which was evaluated was (5X5).

5.6 Statistical Analysis

All data are reported as the mean $\pm$ 1 standard deviation unless otherwise stated. The Anderson- Darling test was used to analyze the normality of the different sets of data. A p-value ≤ 0.05 was considered to be statistically significant for all the comparisons in this study. All statistical analyses were carried out using Minitab 14 software (Minitab Inc, USA) and the data analysis tool from Excel spread sheets (Microsoft, USA).

Regurgitation volumes were calculated by integrating the negative systolic flow from the average mitral flow curve (10 cardiac cycles). Regurgitation fractions were calculated by dividing the regurgitation volume by the average stroke volume (10 cardiac cycles). Mean regurgitation fractions for the different papillary muscle positions were compared using two tailed paired t-tests as these data were normally distributed and natural pairing was present.

Chordal force/stress distributions were compared using the peak systolic force/stress values (peak systolic force-PSF, peak systolic stress-PSS). Peak systolic force and peak systolic stress data did not follow normal distributions. Therefore, differences in force/stress due to PM position or annular configuration were compared using the one sample Wilcoxon test. A 3-way unbalanced ANOVA was also conducted as suggested by a statistician. To be able to employ this test a Box-Cox transformation with λ's ranging from 0.1 to 0.22 was used to transform the data into a normally distributed set. After transformations in the described range for λ, the Anderson-Darling and Kolmogorov-Smirnov tests showed that the distribution was normal. This ANOVA model used species, chordal type and papillary muscle position as predictor variables and used PSF as

the response. The model showed that PM position and chordal type significantly affected chordal force ($p<0.01$). Species or any interaction between species and other variables did not affect chordal force ($p>0.1$). The interaction between chordal type and PM position did affect chordal force, showing how PSF on distinct types of chords is affected differently by different PM positions. Although this model could provide further details on how PM position affects force distribution, the model showed lack of fit ($R^2<0.6$). However, the model agreed with the general conclusion obtained from the Wilcoxon tests. Furthermore, six one way ANOVAs, one for each type of chord with the transformed data (predictor variable = PM position, response = chordal force) were conducted. These ANOVAs were complemented by using the Dunnett test for multiple comparisons. The Dunnett tests were used to compare the seven different PM positions to a reference position (normal PM position). Although the ANOVAs still showed lack of fit, they demonstrated the importance of PM position with respect to PSF on the different chords ($p<0.05$). The Dunnett tests which compare the forces when the PMs were displaced to those present in the normal PM positions agreed with the Wilcoxon non-parametric tests in most of the cases. They completely agreed for the tests on the anterior strut chord, posterior intermediate chord and posterior marginal chord. For the anterior marginal chord it showed no significant difference for any of the tested positions (previous Wilcoxon tests showed a significant difference for one position). This difference does not disagree with the general conclusions for this study, since they state that the marginal chords are those least affected by PM displacement. The commissural and basal posterior chords were less sensitive to PM displacement using the Dunnett test instead of the Wilcoxon, but still these chords were the most sensitive to PM

displacement when compared to the other chords. Therefore the conclusions using the Wilcoxon tests hold. In the results chapter the statistical comparisons for PSF and PSS in the different PM positions use the Wilcoxon test, since it is the most appropriate for the non-normally distributed PSF data.

For the Alfieri experiments, multivariate ANOVA analysis was conducted to observe if mitral flow rate, transmitral pressure and mitral annular area had a significant effect on Alfieri stitch force. A single ANOVA model could not be constructed for the whole cardiac cycle using mitral flow rate, transmitral pressure, and mitral annular area as predictor variables and Alfieri stitch force as response since this approach lead to lack of fit for the regression model (R^2<0.5). The single model approach did not work since Alfieri stitch force during systole and diastole depends on different predictor variables. In order to solve this problem two independent models, one during systole and one during diastole, were created. Both of these models demonstrated excellent correlation (R^2=0.8 Systole, R^2=0.9 Diastole). For the Alfieri repair experiments, paired t-tests were used to compare the average regurgitation volumes, average effective orifice areas, and average peak Alfieri forces under the different conditions since these data were normally distributed and natural pairing was present.

For the anterior leaflet strain experiments percentage differences in principal stretches and areal strains were calculated using the flat annulus configuration as the reference. The data for the major principal stretch, minor principal stretch and areal stretch were normally distributed. Therefore, differences in these variables associated with the different annular configurations were compared using paired t-tests since natural paring between groups was present.

The power rank test was used on two main data sets which showed no statistically significant differences among any of their groups. The first data set was that of PSFs for the marginal chords in the different PM positions (both the anterior marginal and posterior marginal chord). These data sets were characterized by large standard deviations and only a single position of the fourteen (seven for each chord) demonstrated a significant difference in force. Because of the large standard deviation the results showed low power for these tests. These test also proposed an unrealistic number of samples (>100) in order to obtain 95% statistical power for the standard deviations that these chords presented. Analysis of the data demonstrated that statistical power is not the determinant factor which restricted the results for these particular experiments. The relatively small sensitivity for the forces on these chords (the magnitudes in force were near to the lower measurable boundary for the C-ring transducers) implies that different transducers must be used in order to obtain better results. More sensitive transducers should lead to smaller standard deviations and increased statistical power for the results.

The second data set which was analyzed for statistical power was that of the minor principal stretch for the leaflet strain experiments. For the 10% and 20% saddle height to commissural diameter ratio configurations the tests showed high statistical power (>95%). For the 30% saddle height configuration the statistical power was not as high, since the presence of abnormal strain patterns in two of the valves increased the standard deviation for this set.

CHAPTER VI

RESULTS

6.1 Overview

The results of this study are divided into three main sections corresponding to each specific aim. Since the experiments in specific aim 1 were focused on the normal mitral valve, the results from this aim were used as a reference baseline to analyze changes associated with pathological (specific aim 2) and repair (specific aim 3) conditions. Chordal diameter/area measurements are presented in a subsection of specific aim 1, although these measurements were also used to calculate the chordal stresses for specific aim 2.

In all experiments, mitral flow, transmitral pressure, chordal force and Alfieri stitch force data were acquired for ten cardiac cycles and averaged offline. Strain was calculated from marker coordinates obtained during a single cardiac cycle for a specific set of experimental conditions. Strain measurements were acquired during a single cardiac cycle because of limitations associated with the size of the data sets.

In this study, measurements were only excluded due to technical limitations of the transducers or substandard data acquisition. For experiments on chordal force distribution, peak systolic force measurements under 0.01N were discarded, as they could not be distinguished from electrical crosstalk. The C-rings were calibrated before and after each experiment to assess transducer functionality and linearity. Measurements for

individual chords were discarded after each experiment only if the transducer showed malfunction during post-experimental calibration. Leaflet strain data sets were discarded if all the markers of interest were not clearly visible during initial valve closure, full coaptation, and subsequent leaflet separation (90 - 110 frames). Strain data was also discarded if leakage orifices were observed during coaptation.

6.2 The Normal Mitral Valve

6.2.1 Chordal Cross-sectional Area

Six different chords from each valve (12 valves) were measured at three different locations as described in section 5.1.1. Chordal diameters were used to calculate chordal area assuming a circular cross-section. A summary of the chordal diameters for the different types of chords is presented in Table 6.1.

Table 6.1. Average chordal diameters for different chordal types and locations.

Chordal region	Anterior strut Diameter (mm)	Anterior marginal Diameter (mm)	Posterior marginal Diameter (mm)	Posterior intermediate Diameter (mm)	Basal posterior Diameter (mm)	Commissural Diameter (mm)
Leaflet insertion	1.611 ± 0.200	0.686 ± 0.202	0.600 ± 0.118	0.965 ± 0.216	1.286 ± 0.491	0.898 ± 0.225
Central area	1.450 ± 0.264	0.653 ± 0.268	0.588 ± 0.199	0.924 ± 0.257	1.194 ± 0.341	0.946 ± 0.116
PM insertion	1.705 ± 0.198	0.633 ± 0.178	0.701 ± 0.222	1.091 ± 0.193	1.013 ± 0.374	1.082 ± 0.321
Average	**1.589 ± 0.241**	**0.657 ± 0.214**	**0.630 ± 0.187**	**0.993 ± 0.229**	**1.164 ± 0.412**	**0.975 ± 0.242**

Table 6.2 presents a summary of the chordal cross-sectional areas calculated from diameters presented in Table 6.1. Paired t-tests were used to compare the different chordal diameters, as the data was normally distributed (Anderson-Darling test). When comparing the marginal chords to the intermediate chords, the results showed that the intermediate chords had a significantly ($p<0.01$) larger cross-section than the marginal

chords on their respective leaflets. The chords which insert near the annulus (commissural & basal posterior) had areas smaller than the marginal chords but greater than the intermediate chords.

Table 6.2 Average cross-sectional areas for the different types of chords in the corresponding sub-regions.

Chordal & Measurement Location	Anterior Leaflet		Posterior Leaflet		Annulus	
	Anterior strut Area (mm^2)	Anterior marginal Area (mm^2)	Posterior intermediate Area (mm^2)	Posterior marginal Area (mm^2)	Basal posterior Area (mm^2)	Commissural Area (mm^2)
Leaflet insertion	2.07 ± 0.52	0.40 ± 0.22	0.77 ± 0.32	0.29 ± 0.11	1.47 ± 1.05	0.67 ± 0.35
Central area	1.70 ± 0.63	0.39 ± 0.37	0.72 ± 0.40	0.30 ± 0.22	1.20 ± 0.71	0.71 ± 0.17
PM insertion	2.31 ± 0.49	0.34 ± 0.19	0.96 ± 0.34	0.42 ± 0.26	0.91 ± 0.71	0.99 ± 0.53
Average	**2.03 ± 0.59**	**0.37 ± 0.27**	**0.82 ± 0.36**	**0.34 ± 0.21**	**1.19 ± 0.85**	**0.79 ± 0.40**

As shown in Table 6.2 the chordae tendineae did not have a uniform thickness throughout their length. The anterior strut chord was significantly ($p<0.01$) thinner in the central region of the chord when compared to its PM insertion end. In contrast, there was no significant difference ($p>0.05$) in thickness for the studied regions of the anterior marginal chord. The posterior intermediate chord was significantly ($p<0.05$) thicker in the PM insertion end when compared to the central region. Similarly, the posterior marginal chord was significantly ($p<0.05$) thicker in the PM insertion end when compared to the leaflet insertion end. On the contrary, the basal posterior chord was significantly ($p<0.02$) thicker in the leaflet insertion end of the chord. Finally, the commissural chord was significantly ($p<0.02$) thicker in its PM insertion region when compared to the leaflet insertion end.

6.2.2 Valve Function

Six human mitral valves were studied at 120±2mmHg peak trans-mitral pressure and cardiac output of 5.0±0.1 L/min using the variable annulus shape atrial chamber in the Georgia Tech Left heart simulator. In the defined normal PM position and normal saddle height to commissural diameter ratio (SR=20%), the valves coapted well showing no regurgitation orifices along the coaptation line or leakage jets in the echocardiographic images.

6.2.3 Chordae Tendineae Force and Stress Distribution

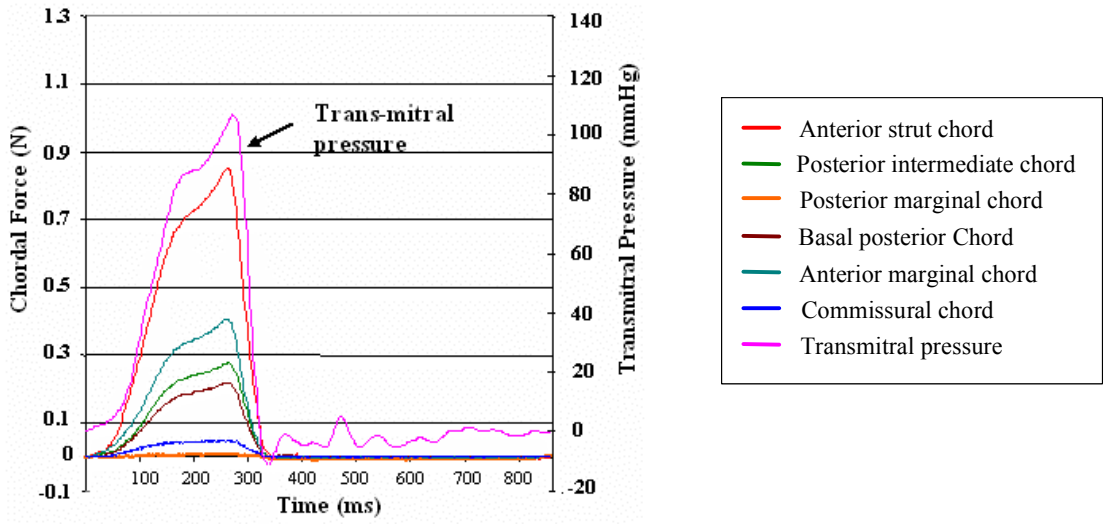

Figure 6.1. Plot of chordae tendineae force and trans-mitral pressure during one cardiac cycle. The graph shows that the force curves follow the trans-mitral pressure curve.

As shown in Figure 6.1 the chordae tendineae force curves followed the trans-mitral pressure curve. This trend was observed in all the valves studied. The averaged (10 cardiac cycles) chordae tendineae force curves were plotted against time (860ms). Diastolic force was considered as baseline for the chordal force curves [71]. Summary tables of all processed data sets for all specific aims are presented in Appendix B. Raw

data and processed excel spreadsheets for all experiments are cataloged and available on CD1.

Six valves were instrumented with C-rings for the chordal force distribution experiments in specific aim 1. Chordal force was compared using peak systolic force (PSF) values for individual chords. Of the six valves tested with C-rings, data from the posterior marginal chord from valve 1 was discarded because of a strain gauge malfunction detected during the experiment and confirmed during post-experimental calibration. Table 6.3 presents a summary of chordae tendineae peak systolic force for specific aim 1. This table shows the average PSF for the individual chords of the six valves, for the normal (SR 20%) saddle annulus configuration. When comparing the peak systolic forces on the different chords, the secondary chords (anterior strut and posterior intermediate chords) held significantly ($p<0.05$) larger loads on each of their respective leaflets when compared to the primary chords (anterior marginal and posterior marginal chords). The force on the basal posterior chord and the commissural chord was not significantly ($p>0.05$) different.

Table 6.3. Average chordal area, peak systolic force and peak systolic stress for the studied chords in the normal PM position and (SR=20%) saddle configuration.

Chord	Average Chordal Area (mm^2)	Peak Systolic Force (N)	Peak Systolic Stress (MPa)
Anterior Strut	2.03 ± 0.59	0.95 ± 0.35	0.47 ± 0.17
Anterior marginal	0.37 ± 0.27	0.35 ± 0.16	0.94 ± 0.42
Post. Intermediate	0.82 ± 0.36	0.30 ± 0.18	0.37 ± 0.22
Post. Marginal	0.34 ± 0.21	0.06 ± 0.04	0.17 ± 0.13
Basal Posterior	1.19 ± 0.85	0.31 ± 0.25	0.26 ± 0.21
Commissural	0.79 ± 0.40	0.11 ± 0.20	0.14 ± 0.25

Peak engineering stresses were calculated by dividing peak systolic chordal forces by the respective average chordal cross-sectional area. As shown in Figure 6.2, the intermediate

chords carried the largest forces on their respective leaflets when compared to the marginal chords. In contrast, the anterior marginal chord was subjected to the largest peak systolic stress (PSS) when compared to the PSS held by the anterior strut chord. The significantly ($p<0.05$) higher stress on the anterior marginal chord was a direct result of its relatively small cross-section. There was no significant difference in peak stress between the posterior intermediate chord and the posterior marginal chord, although as previously stated the posterior intermediate chord carried the largest load.

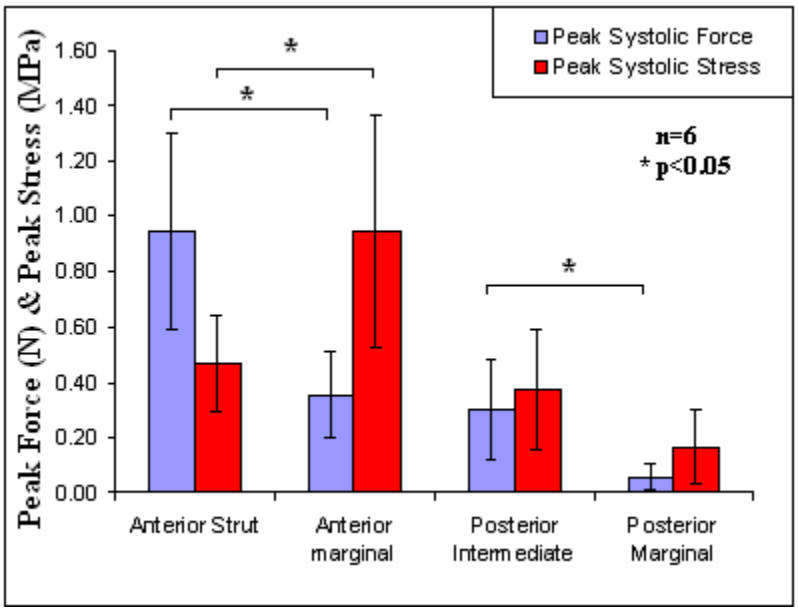

Figure 6.2. Plot of peak systolic forces and stresses for the intermediate and marginal chords on their respective leaflets. Comparisons between groups are based on paired t-tests.

6.2.4 Anterior Leaflet Strains

Eight porcine mitral valves were tested in order to characterize the strain on the central region of the anterior leaflet. During systole there was a rapid raise in stretch followed by a plateau which lasted approximately 200ms (Figure 6.3A). After the plateau, stretch decreased with valve aperture. The plateau corresponded to the maximum deformation of

the tissue while the valves were closed and fully loaded. This behavior was observed in all the studied valves. For all valves, the central section of the anterior leaflet demonstrated a highly anisotropic behavior with the major principal stretch oriented in the radial direction while the minor principal stretch was oriented in the circumferential direction. Figure 6.3 shows the anisotropic behavior of the studied valves.

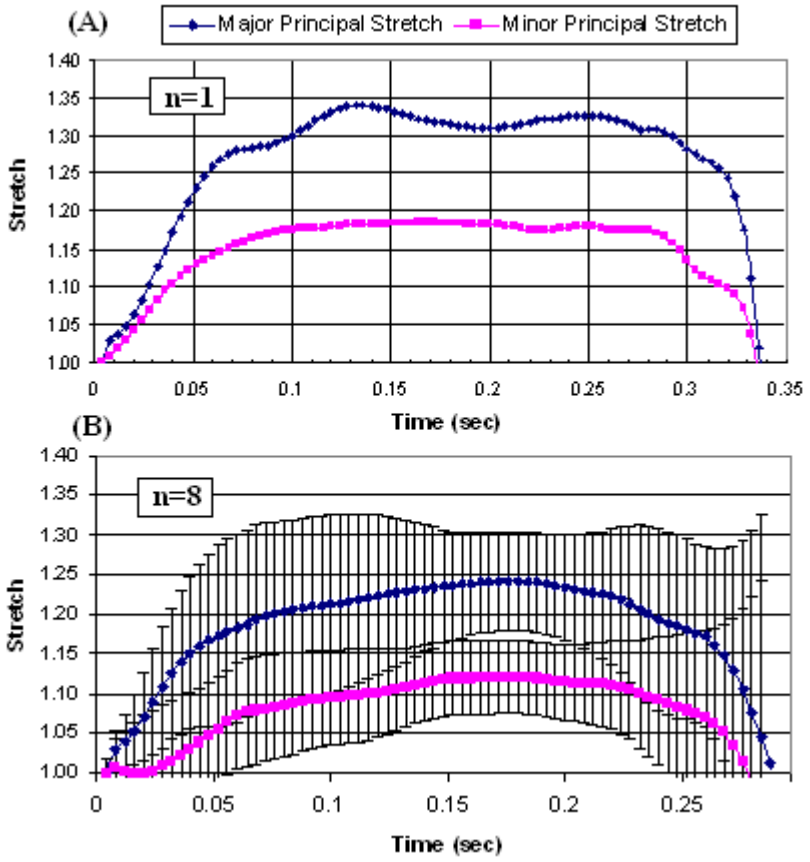

Figure 6.3. (A) Plots of the major and minor principal stretch during the systolic phase of the cardiac cycle for a typical porcine mitral valve (valve #3). (B) Average major and minor principal stretch for the eight valves studied during the systolic phase of the cardiac cycle. Bars represent one standard deviation.

Averaged values (n=8) showed that during valve closure the major principal stretch rate was 21.25±1.95s^{-1} while the minor principal stretch rate was 19.34±1.5s^{-1} (Figure 6.3B).

Maximum stretch was reached while the valves were fully loaded. The maximum mayor principal stretch was 1.22±0.07, whereas maximum minor principal stretch was 1.11±0.049, demonstrating the highly anisotropic nature of the material with the major principal stretch being twice as large as the minor principal stretch (Figure 6.3B). The maximum areal stretch was 1.36±0.14 representing the overall maximum deformation of the central region of the anterior leaflet. After the systolic stretch plateau, stretch decreased rapidly with valve aperture. During valve aperture the major principal stretch rate was 29.75±2.73s^{-1}, while the minor principal stretch rate was 27.01±2.1s^{-1}. The progression of stretch was followed until the markers of interest were no longer visible.

6.3 The Pathological Mitral Valve

6.3.1 Valve Function

Figure 6.4. Doppler image of mitral valve subjected to papillary muscle displacement. The mitral valve is closed, but with observable regurgitation jets (red).

Six mitral valves were studied at 120±2mmHg peak trans-mitral pressure and cardiac output of 5.0±0.2 L/min using the variable annulus shape atrial chamber in the Georgia

Tech Left heart simulator. In the defined normal PM position and flat annular configuration (SR=0%), the valves coapted well showing no regurgitation orifices along the coaptation line or leakage in the echocardiographic images. When the PMs were displaced regurgitation orifices appeared along the coaptation line producing regurgitation jets as shown in Figure 6.4.

Regurgitation volumes were calculated by integrating the negative systolic volume of the flow curve. Regurgitation volumes in the different PM positions were then compared to the closing volume of the valve in the normal position. The difference between the regurgitation volume of the valve in the displaced PM position and the closing volume of the valve in the normal position quantified valve leakage. Regurgitation fractions were calculated by dividing the regurgitation volume by the stroke volume.

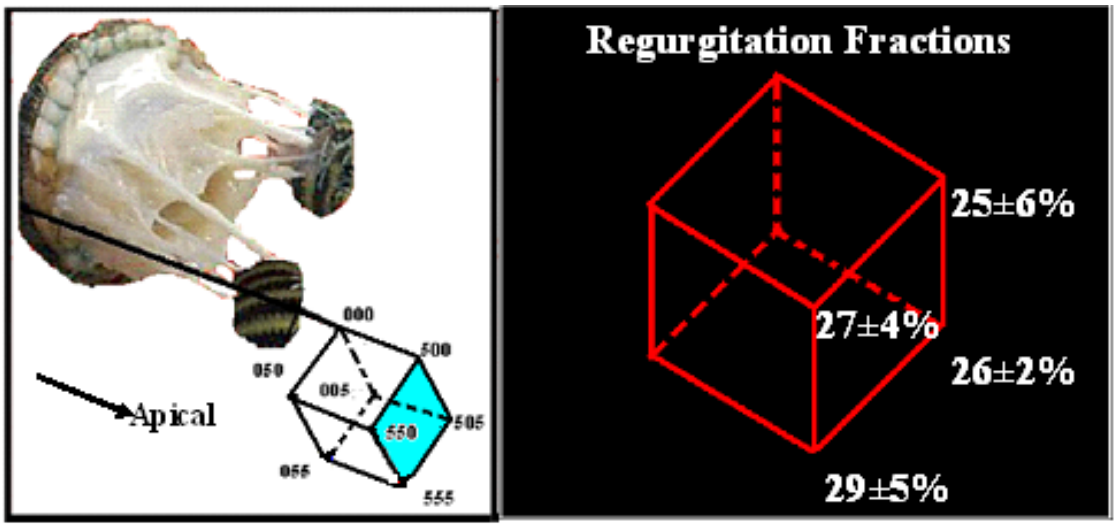

Figure 6.5. (Left) Diagram of the mitral valve with the different PM positions. The aquamarine face of the cube describes those positions associated with apical displacement. (Right) Clinically significant regurgitation volumes for the different PM positions.

Four different PM positions demonstrated significant increases in regurgitation volume. As shown in Figure 6.5, positions 500, 505, 550 and 555 had clinically significant

regurgitation fractions (>20%). All of these increases in regurgitation were statistically significant ($p<0.05$) when compared to the closing volume in the normal PM position.

As observed in Figure 6.5, all positions with increased and clinically significant regurgitation volumes were associated with apical displacement of the papillary muscles. Echocardiographic images of the valves with mitral regurgitation after PM displacement showed restricted leaflets with tented geometries during valve closure. These alterations to leaflet coaptation geometry lead to MR. Position 055 associated both with lateral and posterior displacement demonstrated an increase in regurgitation, but this increase was not clinically significant.

6.3.2 Chordae Tendineae Force and Stress Distribution

The chordae tendineae tension curves were observed to follow the trans-mitral pressure curve for all valves (Figure 6.1). All valves coapted correctly with no observable regurgitation orifices in the normal PM position. No chordal rupture was observed in any of the studied valves. Chordal force distributions were compared using peak systolic force (PSF) values for individual chords. The force present on the individual chord during diastole was considered as the baseline.

Peak systolic force measurements under 0.01N were discarded because they could not be distinguished from electrical crosstalk. The C-rings were calibrated before and after the experiment to assess transducer functionality and linearity. Measurements for individual chords were discarded after each experiment if the transducer showed malfunction in post-experimental calibration. Data for positions 005 and 505 were not obtained for all experiments because of geometrical restrictions in the PM displacement apparatus. The

PM holders used in this study have a limited range of posterior motion. When the normal PM position for a specific valve was already near to the limit of this range, it was not possible to move the PM 5mm posteriorly from this normal position. No other criterion was used to discard measurements.

For all chords, percentage variations in PSF and PSS used as reference the normal papillary muscle position unless otherwise stated. Differences in PSF and PSS for the different PM positions were compared using the Wilcoxon test since the data was not normally distributed.

Table 6.4. Chordal area, peak systolic force and peak systolic stress for the studied chords in the normal papillary muscle position and flat annulus configuration.

Chord	Average Chordal Area (mm^2)	Peak Systolic Force (N)	Peak Systolic Stress (MPa)
Anterior Strut	2.03 ± 0.59	1.22 ± 0.52	0.60 ± 0.25
Anterior marginal	0.37 ± 0.27	0.31 ± 0.17	0.84 ± 0.46
Post. Intermediate	0.82 ± 0.36	0.25 ± 0.14	0.30 ± 0.17
Post. Marginal	0.34 ± 0.21	0.03 ± 0.04	0.10 ± 0.12
Basal Posterior	1.19 ± 0.85	0.19 ± 0.09	0.16 ± 0.08
Commissural	0.79 ± 0.40	0.17 ± 0.18	0.22 ± 0.23

Table 6.4 presents the chordal force distribution for the flat annulus configuration and normal PM position. As shown in this table the intermediate chords carried the largest PSF on their respective leaflets when compared to the marginal chords ($p<0.05$). There was no significant difference in PSS between the anterior strut chord and the anterior marginal chord. In contrast, the posterior marginal chord was subjected to a higher ($p<0.05$) PSS when compared to the stress held by the posterior intermediate chord. Therefore, although the forces followed the same pattern as those presented in Table 6.3 for the valve in the normal annulus (SR 20%) and PM configurations, the stress

distribution behaved differently. In the flat annulus configuration the chords which inserted into the anterior leaflet were subjected to statistically similar stresses, whereas the posterior intermediate chord was subjected to a significantly ($p<0.05$) larger stress when compared to the stress on the posterior marginal chord.

When comparing the chordal stress/force distributions for the saddle and flat annulus configurations in the normal PM position significant differences could be observed. For all valves, the PSS on the anterior strut chord was lower 18.5±16.1% in the saddle configuration when compared to the flat configuration ($p<0.05$). The PSS on the posterior intermediate chord was 22.3±17.1% higher in the saddle configuration when compared to the flat annulus configuration. Measurements on the commissural chord showed a decrease of 59.0±32.2% in PSS for the saddle configuration when compared to the flat configuration. For all of the other chords studied the differences in PSS associated with differences in annular configuration were not statistically significant.

6.3.2.1 Anterior Strut Chord

As reported in Table 6.4, the average PSF on the anterior strut chord was 1.22±0.52N whereas the peak systolic stress (PSS) was 0.60±0.25MPa in the normal PM position. Although the force/stress appeared to decrease in position 005, this variation was not statistically significant (Figure 6.6). When the PMs were moved to position 050 and position 055, PSS for this chord did not significantly vary from that measured in the normal position. In contrast, significant ($p\leq0.05$) increases in PSS of 40%±23%, 43%±24%, and 39%±33% were observed when the PMs were moved to position 500, position 550, and position 555, respectively. Comparing position 505 to position 500,

there was a decrease in stress ($p \leq 0.05$), whereas the apparent increase between positions 505 and 005 was not statistically significant (p=0.1).

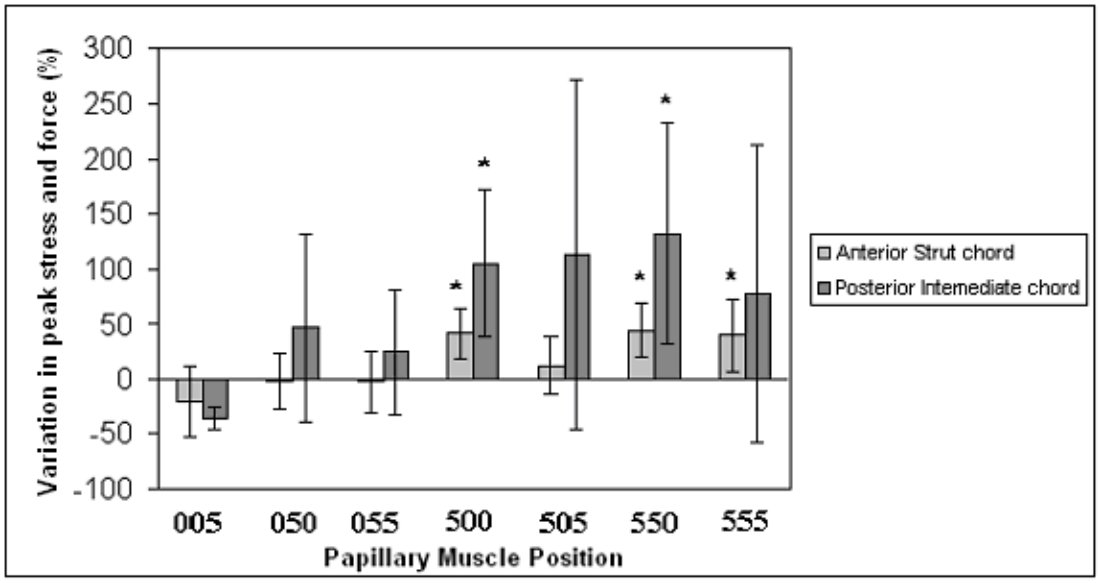

Figure 6.6. Average variations in peak systolic stresses of the different papillary muscle positions for the anterior strut chord and posterior intermediate chord. The bars represent the mean values ± standard deviation. The asterisk (*) represents statistically significant ($p \leq 0.05$) differences between the median of the stresses present in the different papillary muscle positions with those present in the normal papillary muscle position.

6.3.2.2 Posterior Intermediate Chord

The average PSF (0.25±0.14N) and PSS (0.30±0.17MPa) on this chord in the normal position decreased ($p<0.05$) by 37%±10% with the posterior displacement of the PMs to position 005. Position 500 showed a significant ($p<0.05$) increase in PSS of 105%±68% when compared to the stresses in the normal PM position. Similarly, PSS had a significant ($p<0.05$) increase for position 550. Although there was an apparent reduction in PSF and PSS when going from position 500 to position 505, this result was not statistically significant. Position 555 showed a similar stress to that present in the normal

PM position. The average variations in PSS for the anterior strut chord and posterior intermediate chord are presented in Figure 6.6.

6.3.2.3 Anterior Marginal Chord and Posterior Marginal Chord

For the anterior marginal and posterior marginal chords, there was no significant ($p>0.05$) difference in PSS for any of the PM positions used in this study, with the exception of position 550 for the anterior marginal chord where there was a reduction of 26%±32%. The PSS for these chords was relatively uniform for all positions as shown in Figure 6.7.

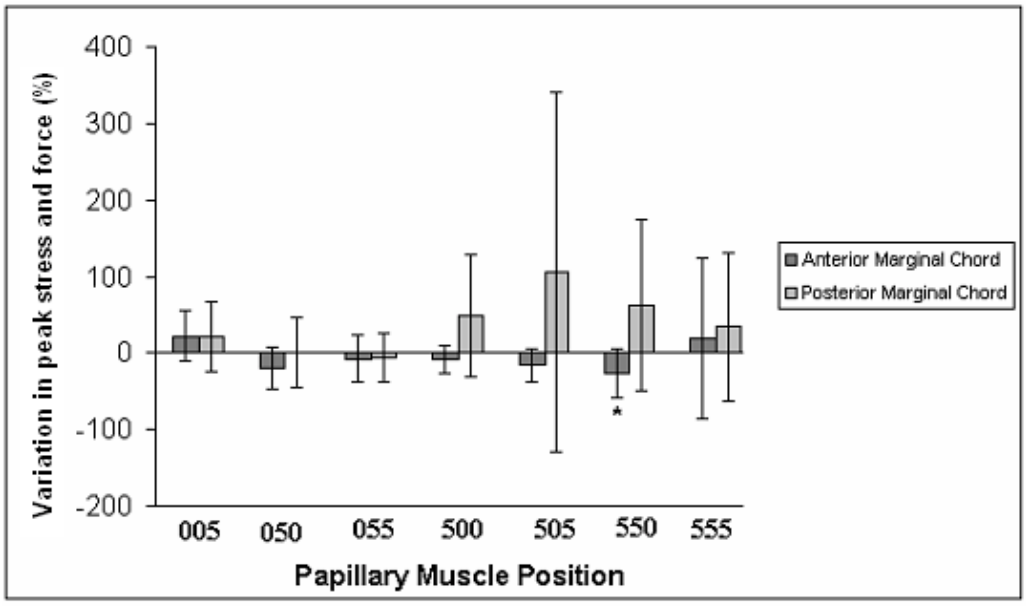

Figure 6.7. Average variations in peak systolic stresses of the different papillary muscle positions for the anterior marginal chord and posterior marginal chord. The bars represent the mean values ± standard deviation. The asterisk (*) represents statistically significant ($p \leq 0.05$) differences between the median of the stresses present in the different papillary muscle positions with those present in the normal papillary muscle position.

6.3.2.4 Basal Posterior Chord

The basal posterior chord was very sensitive to changes in PM position; there were six different positions with statistically significant variations (Figure 6.8). Position 005 and position 050 showed significant decreases in PSSs of 40%±16% and 20%±20% respectively when compared to the PSS present in the normal PM position (PSS= 0.16±0.08MPa, PSF = 0.19±0.09N). In addition, position 055 also demonstrated a significant decrease in stress of 43%±22%. In contrast, relocation of the PMs to position 500 increased the stress by 107%±45%, whereas relocation to position 550 induced an increase in stress of 109%±50%. Position 555 also showed an increase in stress, although this variation was smaller to those observed in position 500 and position 550. When comparing position 500 with position 505, there was a decrease in stress of 30%±9% associated with the posterior motion of the PMs ($p \leq 0.05$).

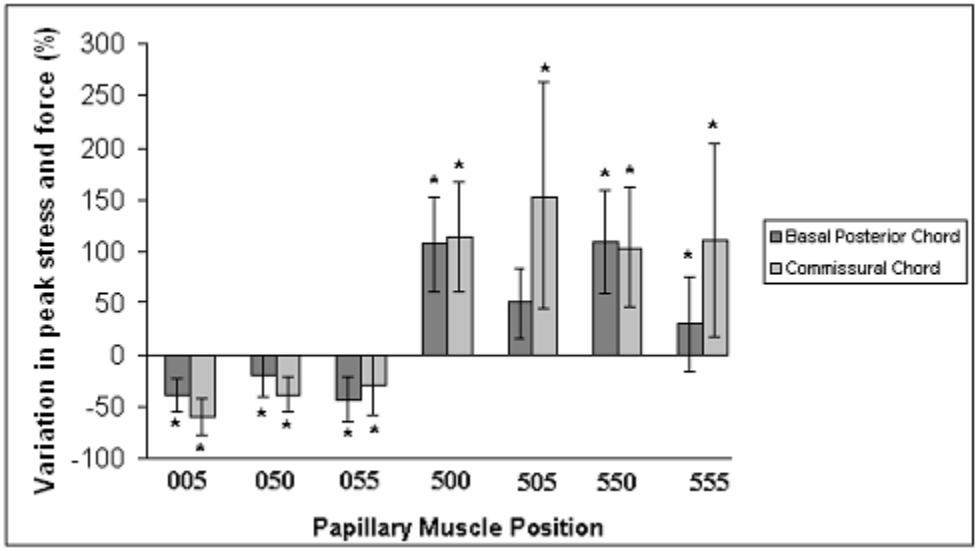

Figure 6.8. Average variations in peak systolic stresses of the different papillary muscle positions for the basal posterior chord and commissural chord. The bars represent the mean values ± standard deviation. The asterisk (*) represents statistically significant ($p \leq 0.05$) differences between the median of the stresses present in the different papillary muscle positions with those present in the normal papillary muscle position.

6.3.2.5 Commissural Chord

The commissural chord showed high sensitivity to PM displacement (Figure 6.8). Position 005, position 050, and position 055 showed decreases in PSSs of 60%±17%, 38%±17%, and 30%±28% respectively when compared to the PSS in the normal PM position (PSF = 0.17±0.18N, PSS = 0.22±0.23MPa). In contrast, position 500, position 505, position 550, and position 555 had increases in force of 114%±52%, 153%±110%, 104%±58%, and 104%±93%. All of the variations were statistically significant ($p<0.05$).

6.3.2.5 Stress/Force Distribution and Papillary Muscle Position

When comparing PSF or PSS for the different PM positions for each individual chord, the results presented the smallest percentage standard deviation in PSF and PSS for the posterior marginal chord (± 15%). The anterior marginal chord also showed a relatively small variation from the average PSF and PSS for all PM positions (±20%). The anterior strut had a standard deviation of ±28%, and the posterior intermediate chord had a standard deviation of ± 48% for the force present in the different PM positions. The largest variations in PSF and PSS for the different PM positions were observed in the basal posterior chord (±56%) and in the commissural chord (±61%).

6.4 The Repaired Mitral Valve

6.4.1 Mechanics of the Alfieri Repair

In section 6.4 results for experiments under steady and pulsatile flow conditions are presented. Experiments were conducted under both of these flow conditions in order to discern the relation between the different variables and elucidate direct mathematical

relations. Five mitral valves were tested under steady flow conditions, whereas ten mitral valves were tested under pulsatile flow conditions.

6.4.1.1. Steady Flow Experiments

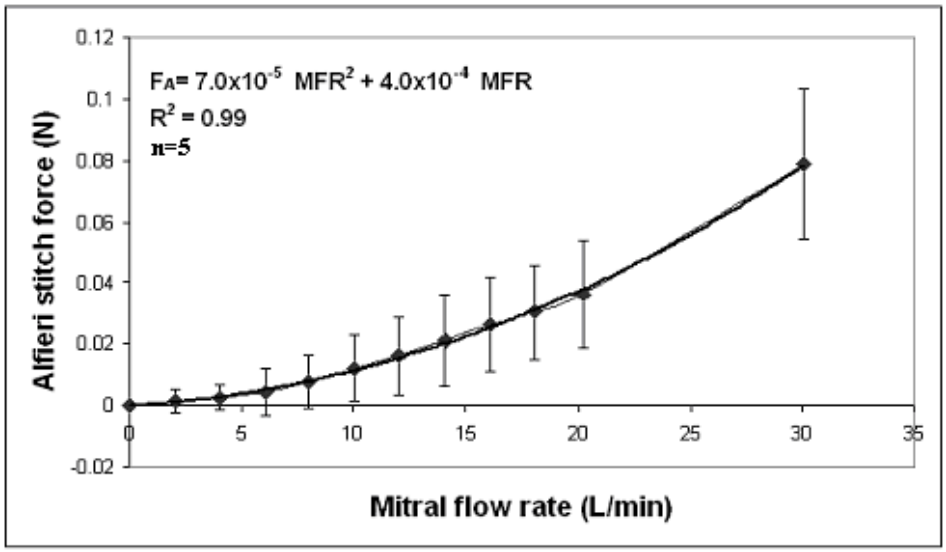

Figure 6.9. Plot of Alfieri stitch force at different mitral flow rates (MFR) in the normal annulus configuration using the steady flow model. The graph shows a non-linear relationship between mitral flow rate and Alfieri stitch force (F_A).

All valves demonstrated a non-linear relation between Alfieri stitch force (F_A) and Mitral flow rate (MFR) in the normal annulus configuration as shown in Figure 6.9. Figure 6.10 shows the effect of mitral annular area (MAA) on F_A (N) under steady flow conditions. The curves once more present a non-linear relation between F_A (N) and MFR (L/min). In addition, increased MAA (cm^2) resulted in decreased F_A. Multivariate ANOVA analysis demonstrated that for the steady flow experiments, both MAA and the square of MFR had a significant effect on F_A:

$$F_A = (8.1\times10^{-5})MFR^2 - (3.1\times10^{-3})MAA + 2.3\times10^{-2} \quad (R^2=0.98)$$

The square of MFR was used as a variable, since all the experiments showed a non-linear relation between MFR and F_A.

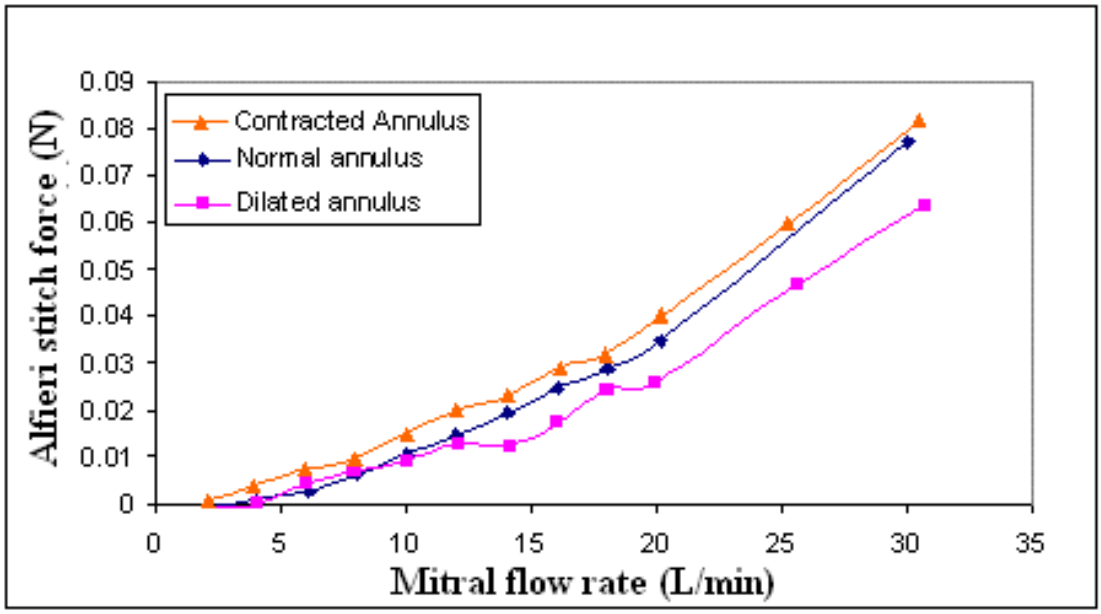

Figure 6.10. Plot of Alfieri stitch force at different mitral flow rates for the different annular configurations under steady flow conditions (n=5). Mitral flow rate and F_A present a non-linear relation. F_A decreases with increasing annular area at the different mitral flow rates.

The pressure drop across the valve (ΔP-mmHg) was linearly related to the force on the Alfieri stitch F_A(N):

$$F_A = (1.84\times10^2)\Delta P \quad (R^2=0.94)$$

Using the pressure drop (mmHg) and the respective MFR (L/min), the EOA (cm^2) was calculated. As shown in Figures 6.11A and 6.11B, EOA increased rapidly with increasing MFR and leveled out after 20L/min. Before the edge-to-edge repair the EOA was 4.06±0.27cm^2, 5.24±0.24cm^2, and 6.31±0.66cm^2 with the contracted, normal, and dilated annuli, respectively, at 30L/min. After the edge-to-edge repair

the EOA was 3.67±0.21cm^2, 4.64±0.24cm^2, and 5.50±0.31cm^2 with the contracted, normal, and dilated annuli, respectively (30L/min).

The average EOA (over flow rates from 5 to 30L/min) decreased significantly ($p<0.05$) after the edge-to-edge repair: 13.16±7.38%, 17.54±11.28% and 18.93±5.11% for the contracted, normal, and dilated annuli, respectively. There was no significant difference between the reductions for the different annular configurations.

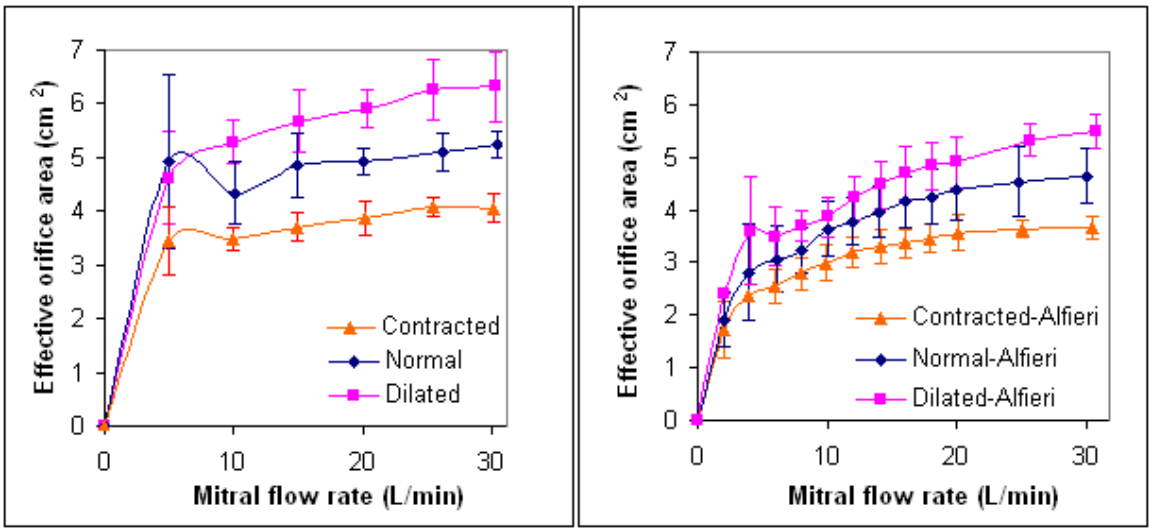

Figure 6.11. Plot of EOA for physiological mitral flow rates using the steady flow model. (A) EOAs for the different annular configurations before the edge-to-edge repair (n=5). (B) EOAs for the different annular configurations after the edge-to-edge repair (n=5).

Therefore, the edge-to-edge repair alone induced an average level of stenosis of 16.55±8.22%, which was independent of annular size. The MVs in the contracted annular configuration after the edge-to-edge repair presented a level of stenosis of 32.80±8.09% compared to the normal MV. Therefore, the edge-to-edge repair in conjunction with annular contraction resulted in a moderate level of MV stenosis.

6.4.1.2. Pulsatile Experiments

The average regurgitation fraction (25.2±7.7%) in the dilated annular configuration was significantly larger than that observed in the normal annular configuration ($p<0.05$). In contrast, there was no significant difference between the regurgitation fractions in the normal (18.2±7.4%) and contracted (16.8±8.3%) annular configurations.

The average diastolic pressure drops through the MV were 2.49±1.49mmHg, 1.61±2.02mmHg, and 1.69±2.11mmHg; corresponding to effective orifice areas of 3.88±1.75cm^2, 5.78±3.15cm^2, and 6.29±4.63cm^2, for the contracted, normal, and dilated annuli, respectively.

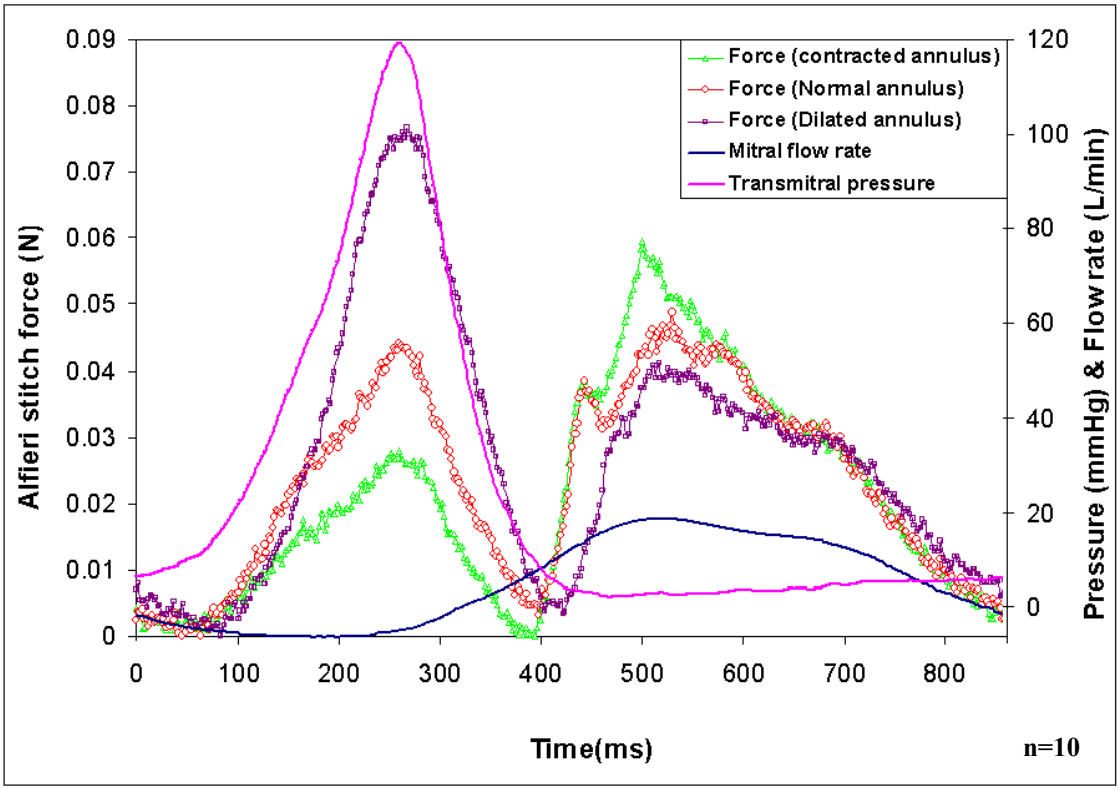

Figure 6.12. Average mitral flow rate, transmitral pressure and Alfieri stitch force during the cardiac cycle for the different annular configurations (n=10). Alfieri stitch force follows the mitral flow rate curve during diastole and the transmitral pressure curve during systole. Increased annular area increases Alfieri stitch force during systole, but decreases Alfieri stitch force during diastole.

The F_A curves showed two distinctive peaks during the cardiac cycle as shown in Figure 6.12. The first peak coincided with the peak trans-mitral pressure and the second peak occurred at maximum forward flow during diastole.

Peak diastolic F_A was dominant when compared to peak systolic F_A in the normal (0.072±0.021N) and contracted (0.071±0.020N) annulus configurations. In contrast, peak systolic F_A (0.092±0.030N) was significantly higher ($p<0.05$) than peak diastolic F_A (0.068±0.024N) in the dilated annulus configuration. There was no significant difference ($p>0.05$) in peak diastolic F_A between the three different annular configurations. On the contrary, peak systolic F_A increased linearly with MAA:

$$F_A = 1.95\times10^{-2}\,MAA - 7.1\times10^{-2} \quad (R^2=0.98)$$

with significant ($p<0.05$) differences in F_A between the contracted (0.039±0.017N), normal (0.059±0.024N) and dilated (0.092±0.030N) annuli (Figure 6.13).

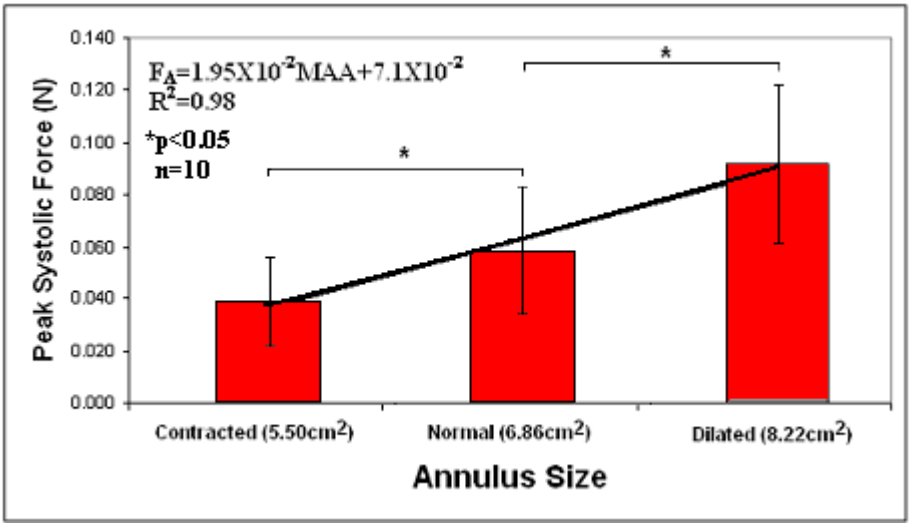

Figure 6.13. Peak systolic Alfieri stitch force for the different annular configurations. There is a linear relation between annular area and peak systolic Alfieri stitch force. The asterisk represent statistically significant differences (*p<0.05). Bars represent the standard deviation of the different groups. F_A – Alfieri stitch force, MAA- Annular area.

F_A was also recorded at peak transmitral pressures of 100 mmHg, 120 mmHg, and 140 mmHg at a constant cardiac output of 5 L/min. As peak transmitral pressure increased, peak systolic F_A increased from 0.051±0.018N to 0.063±0.022N to 0.065±0.025N, respectively, in the normal annulus configuration. Peak systolic F_A increased from 0.081±0.027N to 0.092±0.03N to 0.096±0.034N as peak transmitral pressure increased from 100 mmHg, to 120 mmHg, to 140 mmHg, respectively, in the dilated annulus configuration. .The increases in F_A from 100 mmHg to 120 mmHg were statistically significant ($p<0.05$), whereas the increases from 120 mmHg to 140 mmHg were not significant for both annular configurations. There was no significant difference ($p>0.05$) in mean diastolic F_A for cardiac outputs of 4L/min (0.040±0.021N), 5L/min (0.037±0.019N) and 6L/min (0.038±0.018N), at a constant transmitral pressure of 120mmHg.

Multivariate ANOVA analysis showed that transmitral pressure, MFR and MAA had a significant ($p<0.05$) effect on F_A during the cardiac cycle. As observed in Figure 6.11, F_A followed the MFR curve during diastole and the transmitral pressure curve during systole. Additionally, F_A increased with MAA during systole, but decreased with MAA during diastole, with the most significant variation occurring during systole. Because F_A changed from diastole to systole in a complex fashion, a single statistical model for F_A could not be fit ($R^2<0.6$) over the entire cardiac cycle. Therefore, two different functions were derived, one for systole and one for diastole. During systole ANOVA analysis showed that both transmitral pressure (TP- mmHg) and mitral annular area (MAA - cm^2) had significant ($p<0.05$) effects on F_A(N):

$$F_A = (4.40\times10^{-4})TP + (5.0\times10^{-3})MAA - 0.05 \quad (R^2=0.80)$$

As observed in the steady flow experiments, F_A correlated well with the square of MFR. Therefore, MAA (cm^2) and MFR^2 (L^2/min^2) were used to construct the ANOVA model for diastole:

$$F_A = (1.03\times10^{-4})MFR^2 - (1.60\times10^{-3})MAA + 0.02 \quad (R^2=0.90)$$

Similar ANOVA models may be obtained using transmitral pressure (TP) and annular septal-lateral diameter (SL-cm) as independent variables during systole:

$$F_A = (4.40\times10^{-4})TP + (1.3\times10^{-2})SL - 0.05 \quad (R^2=0.80)$$

And MFR and annular septal-lateral diameter (SL-cm) as independent variables during diastole:

$$F_A = (1.03\times10^{-4})MFR^2 - (4.40\times10^{-3})SL + 0.02 \quad (R^2=0.90)$$

These equations may be used to approximate F_A during the entire cardiac cycle using MFR, transmitral pressure and MAA (or SL) as independent variables.

6.4.2 The Effects of Annuloplasty Ring Geometry (Saddle Height) on Anterior Leaflet Strain.

The marker technique was used on fresh porcine MVs in order to characterize the effect of annular saddle height to commissural diameter ratio (SR) on anterior leaflet strain. Experiments were conducted on ten mitral valves in the Georgia Tech Left Heart Simulator under physiological pressure (TP = 120±2mmHg) and flow (CO = 5.0±0.2L/min) conditions. Only eight of the ten data sets of the experiments were used in the results presented in this section. One data set was discarded because a leakage orifice was observed in the coaptation line. The presence of the leakage orifice did not allow for the valve to maintain a physiologic pressure gradient across its leaflets. A second data set

was discarded because a wrinkle was present in the central area of the anterior leaflet. This wrinkle did not allow for complete visualization of all the markers during coaptation.

6.4.2.1 Characteristics of Leaflet Strain Under a Normal (SR=20%) Peak Systolic Annular Curvature.

Anisotropy was observed in the central region of the anterior leaflet in the normal annulus configuration (Figure 6.3). The major principal stretch was directed in the radial direction, whereas the minor principal stretch was directed in the circumferential direction for all annular configurations.

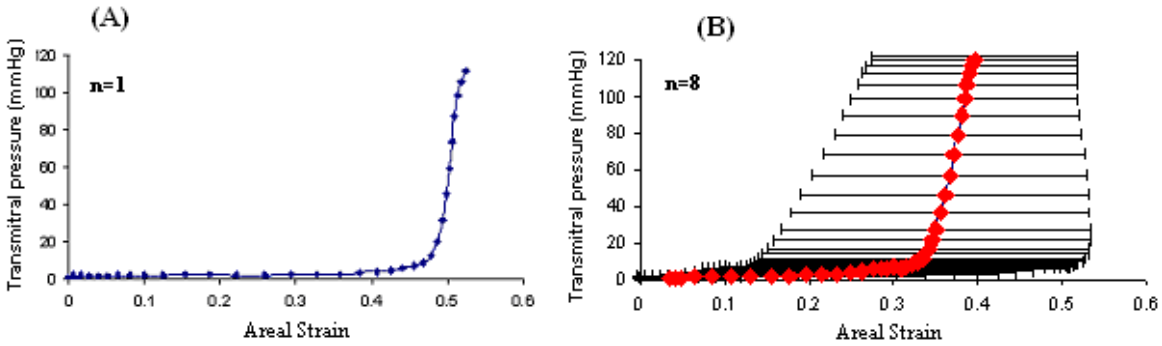

Figure 6.14. (A) Plot of transmitral pressure against areal strain for a typical MV (valve 4) under normal conditions (SR=20%). This plot describes the systolic loading period. (B) Plot of transmitral pressure against average areal strain (n=8) for the valves in the normal annulus configuration. Error bars represent one standard deviation.

The central region of the anterior leaflet was also characterized by a non-linear load-strain response. The load-strain relation is described in Figure 6.14 in plots of transmitral pressure (load) against areal strain. Figure 6.14 represent the loading phase of the cardiac cycle in which the stiffness of the leaflet increases with increasing transmitral pressure. Figure 6.15 present both the loading and unloading strain paths for one of the studied valves. As shown by Figure 6.15, the loading and unloading curve did not follow the

same path, and therefore the material presented hysteresis. This characteristic of the material response was observed in all of the studied valves. As observed in Figure 6.15, the valve does not completely recover during the unloading phase; therefore, the reference frame for this valve does not correspond to the smallest time dependent area for the region of interest.

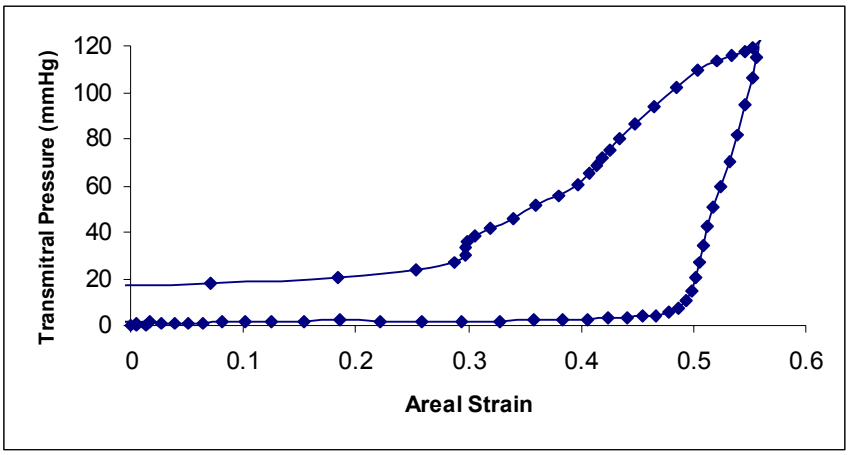

Figure 6.15. Loading and unloading strain curves for a porcine mitral valve under physiological conditions. Hysteresis is observed since the loading and unloading paths are different.

As described in specific aim 1, there was a rapid rise in stretch during initial closure followed by a deformation plateau which lasted during most of systole (Figure 6.2). The valve then recovered when the leaflet started to open (time > 250ms). During the systolic stretch plateau there was no observable creep while the leaflets were fully loaded.

For the normal mitral valve (SR=20%), the peak major principal stretch was 1.22±0.07, whereas peak minor principal stretch was 1.11±0.04. During valve closure the major principal stretch rate was 21.25±1.95s^{-1} while the minor principal stretch rate was 19.34±1.5s^{-1}. During the unloading phase of the cycle (time>250ms) the major stretch rate was 29.75±2.73s^{-1} while the minor principal stretch rate was 27.01±2.1s^{-1}.

6.4.2.2 Changes in Leaflet Strain Associated with Annular Curvature

The mitral valves were tested with four different saddle heights to commissural diameter ratios (SR): 0% (Flat annulus), 10%, 20% and 30%. The experiments were carried out under physiological transmitral pressure (TP = 120±2mmHg) and mitral flow (CO = 5.0±0.2L/min) conditions for all the annular configurations. For all annular configurations the anterior leaflet material showed anisotropy with the major principal stretch in the radial direction and the minor principal stretch in the circumferential direction. The material also demonstrated hysteresis, no creep, and a non-linear load-strain relation under all annular configurations, with similar characteristics to those presented in section 6.4.2.1.

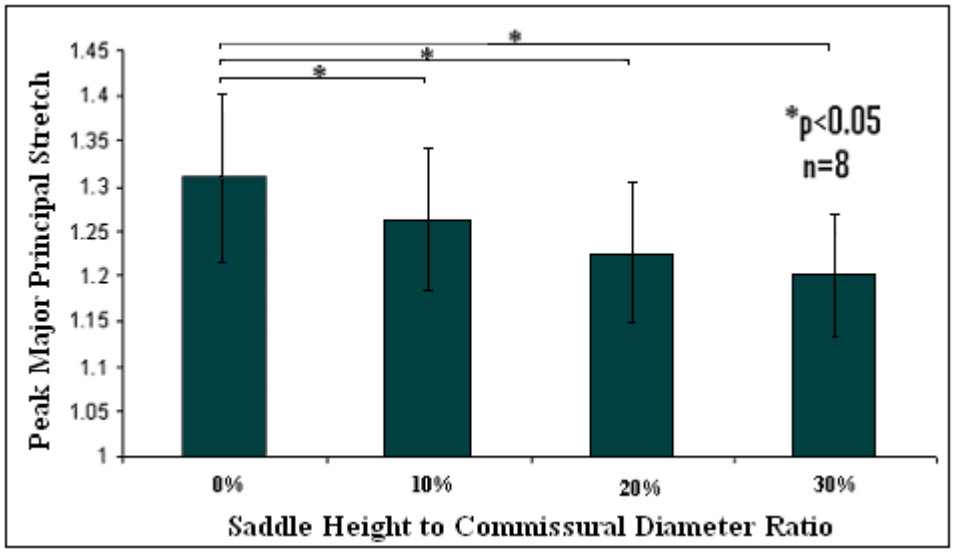

Figure 6.16. Average peak major principal stretch for the different annular configurations. Paired t-tests were used for statistical comparisons. Bars represent one standard deviation.

For the different annular configurations, groups were compared using paired t-tests since the data provided natural pairing and followed a normal distribution (Anderson-Darling Test). As observed in Figure 6.16 the major principal stretch (radial direction) was

reduced with increasing SR. The major principal stretch was reduced 3.43±3.38%, 6.30±3.28%, 8.05±6.92% for the 10%, 20% and 30% SR configurations, respectively, when compared to the flat annulus configuration. These reductions in major principal stretch implied reductions of 13.52±12.79%, 27.53±13.65%, and 29.72±29.79% in the major principal strain for the respective annular configurations. All of these differences were statistically significant. There was a linear relation between the peak major principal stretch (PMPS) and SR:

$$PMPS = -0.37SR + 1.30 \quad (R^2 = 0.98)$$

Figure 6.17 shows the average minor principal stretch (circumferential) for the different annulus configurations. As shown in the figure there was no significant difference in minor principal stretch for the different SR configurations.

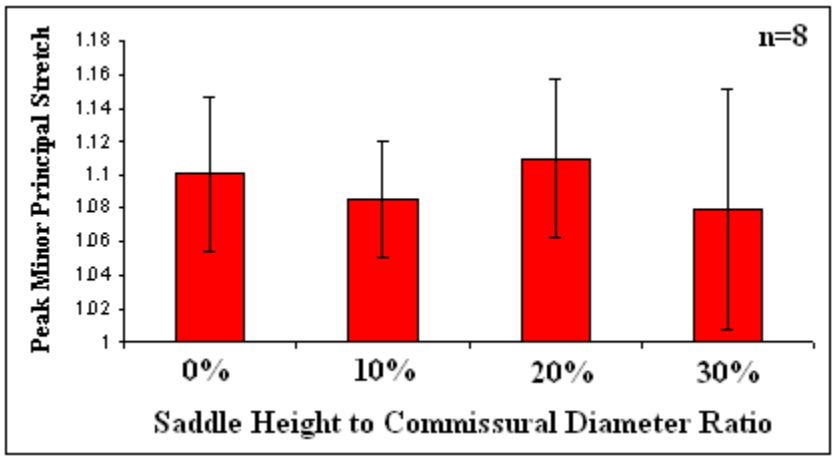

Figure 6.17. Average peak minor principal stretch for the different annular configurations.

Although there was no significant reduction in minor principal stretch associated with different SR configurations, two of the valves studied showed circumferential

compression in the 30% SR configuration. Compression was not observed in any of the other SR configurations. Figure 6.18 shows the minor principal stretch for one of the valve which demonstrated compression.

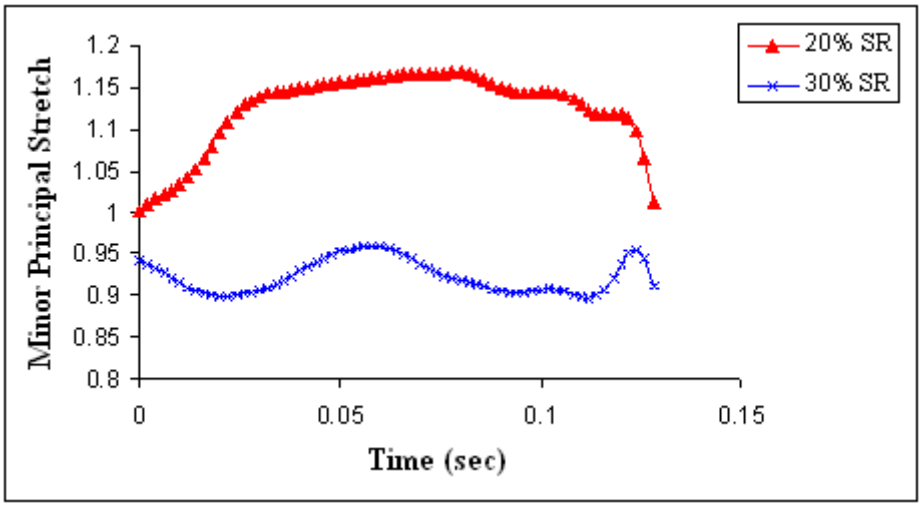

Figure 6.18. Minor principal stretch for valve 6 in the 20% and 30% saddle height to commissural diameter ratio (SR) configurations during systole.

As observed in Figure 6.18, although the valve stretched circumferentially in the 20% SR configuration, it underwent compression in the 30% SR configuration. The onset of compression for these valves was responsible for the large standard deviation in this group and was associated with a significant increase (39.96±29.49%) in circumferential curvature of the leaflet surface.

Variations in SR were also associated with changes in the areal stretch of the central region of the anterior leaflet of the mitral valve. As shown in Figure 6.19, there were significant reductions in areal stretch for the 20% and 30% SR configuration when compared to the flat (0%SR) annulus configuration. These reductions correspond to changes in areal strain of 18.62±18.98% and 27.97± 35.01% for the 20% and 30% SR

configurations, respectively. Although the 10% SR configuration appeared to induce a reduction in strain when compared to the flat annulus, this reduction was not statistically significant (p=0.62).

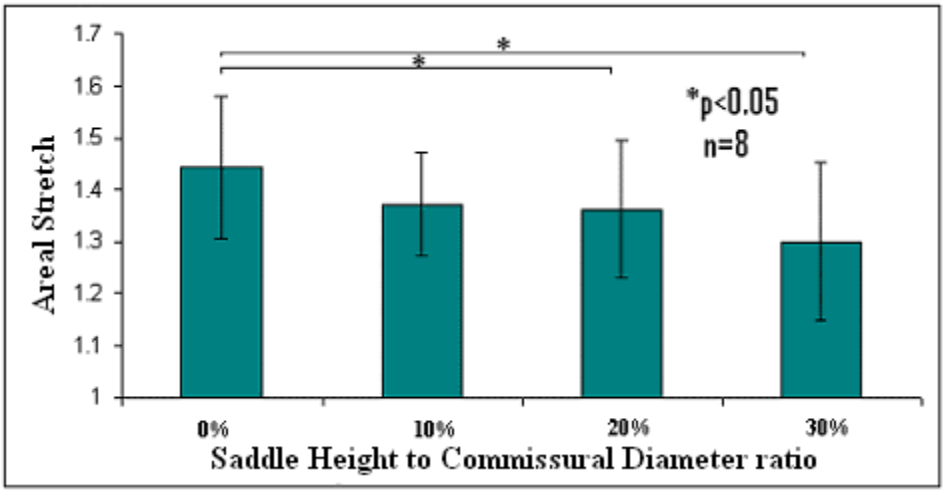

Figure 6.19. Average peak areal stretch for the different annular configurations. Paired t-tests were used for statistical comparisons. Bars represent one standard deviation.

CHAPTER VII

DISCUSSION

7.1 Overview

Currently, mitral valve (MV) repair techniques have shown substandard mid-term and long term results [4-6]. In order to improve the efficacy of these repair techniques, detailed knowledge of the normal function of the mitral valve and the alterations to the valvular and subvalvular apparatus which occur under pathological conditions is required. Furthermore, current techniques may be optimized through a better understanding of the function and mechanics of the MV after a particular repair. The current study provides basic information which may guide clinicians and engineers in the design of new repair techniques or implants, or in the improvements of existing therapies.

The experiments which comprise this study were designed using an *in vitro* approach since this technique has the clear advantage of isolating and independently controlling specific parameters that are of importance to valvular mechanics and function. Furthermore, *in vitro* experimentation can provide detailed quantitative information on the mechanics of the normal, pathological and repaired mitral valve. By controlling independent variables, the mechanics and function of individual components can be characterized providing important information for the development of improved and focused repair techniques. *In vitro* techniques also have cost related advantages when compared to *in vivo* approaches. Although the proposed advantages of the *in vitro* approach in this study are clear, the experiments were designed based on clinical or *in vivo* animal data. The correlation between the *in vitro* data

obtained in this study, and the *in vivo* animal data and clinical data from other research, provides the framework for the clinical relevance of the current study. A fundamental paradigm of biomedical research lies in the synergistic use of *in vitro*, *in vivo*, animal, and clinical data in order to explain complex problems. Therefore, the analysis of the results of this study must be evaluated within the context provided by *in vivo* animal studies and clinical observations.

The results from this study demonstrate how the normal geometric configuration of the mitral valve is mechanically optimized. The normal PM position and annular saddle curvature (SR=20%) provide a more even distribution of loads among the chordae by reducing the force on the most heavily loaded chords (Anterior strut). Additionally, normal annular geometry reduces the strain on the central region of the anterior leaflet which is the most heavily loaded area of the mitral leaflets [67].

The data from this study elucidate how changes in the geometrical configuration of the mitral valve associated with ventricular dilation lead to decreased functionality and unfavorable mechanics on the different components of the mitral valve. Apical displacement of the papillary muscles was shown to increase the loads on the intermediate chords of the mitral valve leading to leaflet restriction and subsequent regurgitation.

Finally, the analysis of some of the factors associated with the Alfieri stitch and rigid ring annuloplasty showed that mitral regurgitation may be partially or completely corrected using these techniques, although abnormal mechanical loading may still be present. The abnormal loading left behind may reduce the durability of these repairs.

7.2 The Normal Mitral Valve

The mitral valve is a multi-component and complex structure with a dynamic geometry that varies throughout the cardiac cycle [7-9], [11]. Previous studies have clearly identified the normal geometry of the mitral valve and its individual components within the left ventricle under physiologic conditions [9-11], [18-21]. Although this geometry has been well characterized, researchers have just begun to understand its functional and mechanical relevance.

The shape of the mitral annulus has been characterized as a three-dimensional saddle because it resembles a non-planar, three-dimensional ellipse. In addition to its position, its area, eccentricity, and non-planarity (or curvature) vary during the cardiac cycle describing a dynamic structure [9], [21], [47-49]. Mitral annular geometry and dynamics have been studied *in vivo* in animals [21], [48-50] and humans [11], [45], [51-53] both in normal and pathologic subjects. Although the exact origin and function of the shape of the mitral annulus is not clear, studies have proposed that this shape may be important as part of the valve's closure mechanism [9] and in the distribution of loads on the mitral valve leaflets [8] and chordae tendineae [7].

A previous study in our laboratory demonstrated that the normal saddle geometry of the mitral valve did not reduce mitral regurgitation when compared to a flat annular geometry [7]. This same study also proposed that the saddle shape of the annulus provided a more even distribution of loads among the chords, and therefore provided a mechanical benefit. Therefore, since the saddle shape of the mitral annulus did not show a direct hemodynamic benefit, the focus of the current study was on the relation between the

saddle shape of the mitral annulus and the mechanics of the valvular and subvalvular components of the MV.

7.2.1 Chordal Force and Stress Distribution in the Normal Mitral Valve

The chordae tendineae prevent leaflet prolapse during systole and subsequent mitral regurgitation. Chordal failure is a common and morbid condition which poses significant obstacles for repair. The causes of chordal failure may be divided into two main groups. The first group is associated with congenital malformations and diseases such as rheumatic fever, infective endocarditis, and myxomatous degeneration among others. This first group is characterized by abnormal tissue structure or tissue degeneration [1], [38], [78-80] which lead to reduced mechanical properties of the chords [82]. The second group of conditions that may lead to chordal failure is associated with ventricular disease and subsequent abnormal load distribution on the chordae tendineae. This second group is characterized by abnormal loading and chordal tissue remodeling. The mechanism of chordal failure due to ventricular dilation is not well understood. Stresses distribution as related to ventricular dilation have not been reported in literature. Therefore, there is no basis for comparative analysis with the failure stress for chords [56], [68]. Although these essential data have not been reported, complementary research suggests that chordal failure in ischemic or dilated cardiomyopathy patients may be due to a combination of tissue remodeling [87] and accumulated damage [88]. Therefore, further understanding of chordal force/stress distribution under normal and pathological conditions is warranted and has direct clinical relevance.

The forces on the marginal and intermediate chordae in the defined normal conditions were comparable to those obtained previously in an *in vivo* porcine model [71]. For the intermediate chordae, the *in vivo* porcine model had an average peak systolic force of 0.7N [71]. The results of the present study showed peak forces of 0.65±0.43N for the MV in the normal configuration. For the marginal chordae, the *in vivo* model reported a peak force of 0.2N [71]. The results of the present study showed an average peak systolic force of 0.23±0.19N. Therefore, peak loads were within physiological ranges for these chords. There is no published *in vivo* data of the force present on the basal chords.

The results presented in section 6.2.3. portray a chordal force distribution for the mitral valve that is characterized by the secondary chords carrying most of the load on their respective leaflets. This characteristic distribution has been observed and analyzed by other researchers [71]. Additionally, the results from chordal area measurements presented in Section 6.2.1 show that the chords which carried the largest loads are those with the largest cross-sectional areas. When calculating chordal stresses from the measured forces and areas the results are quite different. On the posterior side of the valve, the posterior intermediate chord carried stresses which are comparable and not statistically different from those held by the posterior marginal chords. Furthermore, on the anterior side of the valve the marginal chord carried significantly higher stresses than the strut (intermediate) chord. Results from a previous mechanical characterization [56] of the chordae tendineae (Table 2.1) reported that the marginal chords held the largest failure stresses on the anterior side of the valve. In contrast, on the posterior side of the valve the largest failure stresses were held by the intermediate chords [56]. Therefore, the chordal stress results from the current study follow engineering logic since the chords which hold the largest

stresses in the normal valve configuration are those with higher failure limits. When comparing the failure stresses in Table 2.1 to the measured loads in Table 6.3, safety factors of approximately 14, 20, 47 and 29 were obtained for the anterior marginal chord, anterior strut chord, posterior marginal chord, and posterior intermediate chord, respectively. Therefore, failure stresses are at least one order of magnitude greater than the stresses these chords sustain under normal conditions. These high safety factors imply that even under cyclic loading healthy chordae in a normally configured MV should not fail under physiological loading. Therefore, in a normal ventricle (in absence of dilation), chordal failure is probably related to MV tissue degeneration due to disease or congenital structural deficiencies.

7.2.2 Anterior Leaflet Strain in the Normal Mitral Valve

The marker technique has been used successfully to characterize the strain field on mitral valve leaflets under physiological conditions [12], [13]. As in previous studies, the results from the current study demonstrated that the central region of the anterior leaflet is highly anisotropic and has a non-linear load-strain relationship. The major and minor principal stretches measured in the current study are quantitatively similar to those observed in previous research [12]. Previous studies have demonstrated that the higher stiffness in the circumferential direction of the central region of the anterior leaflet [12], [13], [41] is associated with the preferentially circumferential orientation of the collagen fibers in this area [12]. Similarly, previous studies have also associated the non-linear load-strain response to collagen fiber orientation and crimping [12], [41]. As shown in Figure 7.1, during the first phase of MV closure, when the leaflets are coming together, there is a

rapid rise in stretch since most of the load is sustained by the highly deformable elastin fibers.

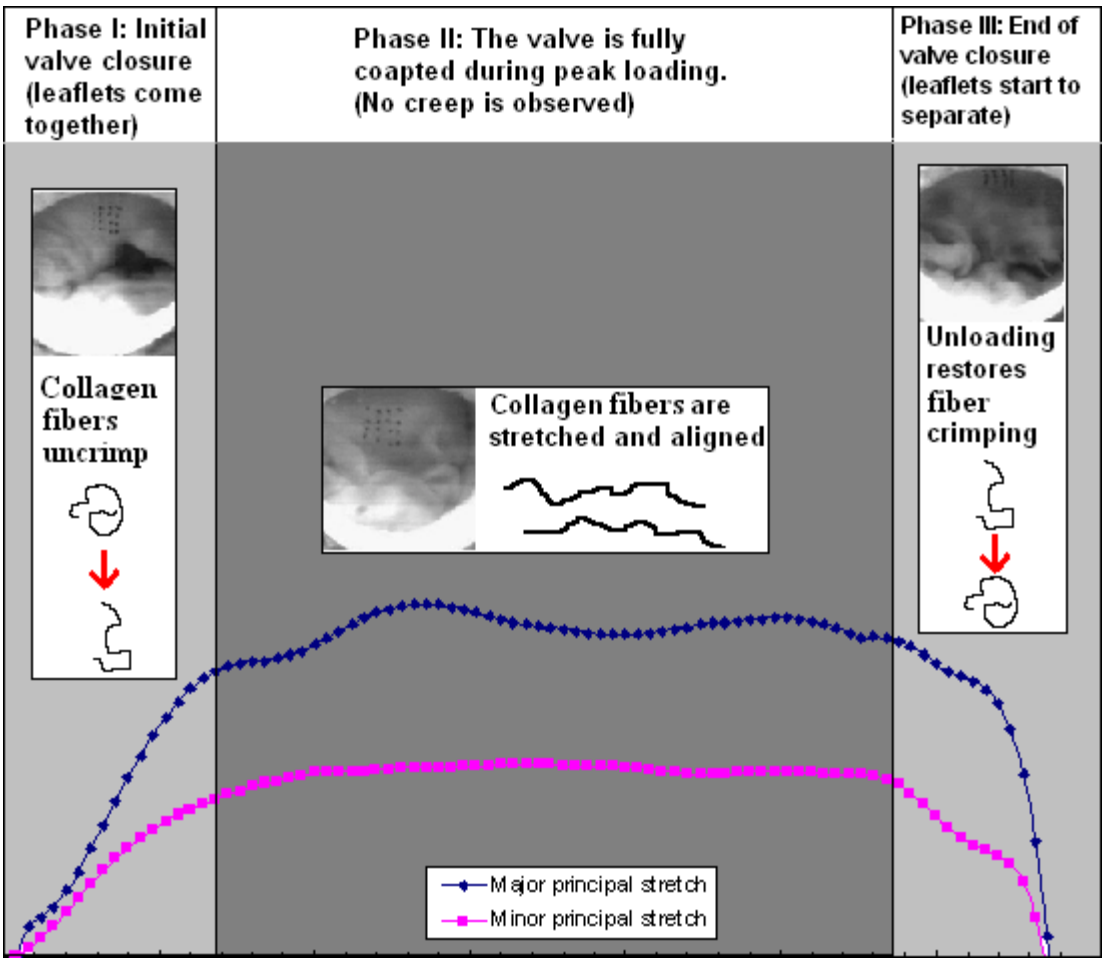

Figure 7.1. Schematic of the different phases of systolic valve closure. The schematic describes how the major and minor principal stretches increase rapidly as the collagen fibers uncrimp during initial valve closure. During Phase II there is a cessation of stretch since the collagen fibers are completely stretched and aligned. Finally when the valve starts to open (Phase III), crimping is restored while the tissue is unloaded.

During this phase (Phase I) the collagen fibers start to uncrimp and align in a preferential direction (circumferential). Increased alignment of the collagen fibers implies increased tissue stiffness in the preferential direction. After the valve is fully closed there is a plateau in strain while the valve is fully loaded (Phase II). During this plateau the

collagen fibers sustain the load on the leaflet since they are fully aligned and stretched. Since collagen fibers are relatively stiff [12], [41], there is a cessation in the deformation of the central region of the leaflet. During the unloading phase of valve closure (Phase III), the leaflet starts to relax and separate. During this period the stretch on the central region of the anterior leaflet decreases rapidly, while the collagen fiber crimping is restored.

The anterior leaflet of the MV is highly adapted to its function since it stretches both in the radial and circumferential directions during the initial phase of closure, aiding coaptation and complete occlusion of the mitral orifice. Furthermore, after the valve is closed, the leaflets maintain a fully coapted state during systolic loading, since there is a cessation in the deformation of the leaflets.

Previous studies have associated changes in the stress on the anterior leaflet with variations in annular geometry [8]. Salgo *et. al*. 2002 used a computational model to show how normal annular geometry (SR=20%) reduced leaflet stress [8]. The results of the current study (which will be discussed in further detail in Section 7.4) demonstrated reduced anterior leaflet strain in the normal annulus configuration. This reduction in strain should be associated with reduction in stress.

7.3 The Pathological Mitral Valve

Though mitral leaflet malcoaptation is the end point through which mitral regurgitation (MR) occurs [84], several topological changes within the left ventricle have been associated with mitral valve malfunction [85]. Ventricular dilation [123-125] and sphericity [126-128], papillary muscle contractile malfunction [50], and motion abnormalities of the left ventricle have been associated with leaflet malcoaptation resulting in mitral regurgitation.

Alterations in the geometry or motion of the left ventricle results in the repositioning of the papillary muscles within the LV. Recent studies both in animal models [21], [50] and human subjects [10] have quantified the displacement of the PMs in pathologies such as ischemic mitral regurgitation (MR) and dilated cardiomyopathy. The results from one of these studies have shown that even subtle (1-2.5mm) alterations in the position of the PMs during the cardiac cycle may lead to leaflet malcoaptation in sheep [21]. The objective of this part of the study was to characterize valve function and chordal force/stress distribution under controlled variations in PM position in order to better understand mitral valve insufficiency in pathologies which induce papillary muscle relocation or discoordination. Clinical observations of extensive LV infarction or LV dilation have shown that both PMs move in the radial direction away from the axis of the LV. The symmetrical apical, posterior and lateral PM displacement (position 555) performed in this study simulated this condition. The other PM positions evaluated in this study were used to assess the independent effects of lateral, posterior or apical motion of the PMs on chordal force distribution and MV function.

The 5mm PM displacement used in this study may appear to be large when compared to the 2.5mm PM displacements observed *in vivo* in ischemic sheep [21]. However, losses of PM contractility on the order of 2-3mm have been observed in humans with cardiomyopathy [10], and increases in end systolic LV endocardial radius of 5mm have been observed in ovine dilated cardiomyopathy models [20]. Therefore, after coupling displacements due to loss of PM contraction, ventricular dilation, ventricular remodeling, and the larger size of the human heart when compared to sheep models, PM dislocations of 5mm are expected to be within pathological range for humans.

The absolute force on the chordae tendineae has two different contributors: a baseline force, which is dependent on the static tethering of the chords, and a dynamic component which is a result of valve and leaflet motion due to trans-valvular pressure. The forces measured in this study were only those associated with trans-mitral pressure as diastolic force was considered baseline. The tethering component of the force can be observed in baseline shifts when repositioning the PMs. Although electrical drift in the transducers was small, the tethering force was not measured since stress relaxation due to the viscoelastic nature of the chords induced baseline shifts, which are significant over the course of an eight hour experiment. In addition, this tethering force is highly dependent on the force resulting from PM contraction. To our knowledge there are no accurate physiological measurements of this force during the cardiac cycle.

A rigid flat annulus was selected for this section of the study because in pathologies such as ischemic mitral regurgitation and dilated cardiomyopathy, which are related to PM displacement, there is a loss of annular dynamics, and flattening and/or dilation of the annulus [18]. Furthermore, to correct annular dilation an annuloplasty ring may be implanted, the presence of these rings also tends to decrease annular dynamics and flatten the annulus [25].

7.3.1 Pathological Mitral Valve Function

The results of the current study demonstrated that clinically significant regurgitation occurred in those positions associated with apical displacement of the PMs (positions: 500,505,550 and 555). Therefore apical PM displacement is the major factor that induces mitral regurgitation. Apical PM displacement causes leaflet tethering during systole

leading to a reduction in the coaptation length, and subsequent leakage gaps in the central region of the valve [65], [84]. Mitral valve regurgitation due to leaflet restriction in patients with pathologies associated with ventricular dilation or remodeling has been observed clinically (Figure 7.2), confirming the findings of the current study [51], [129-131].

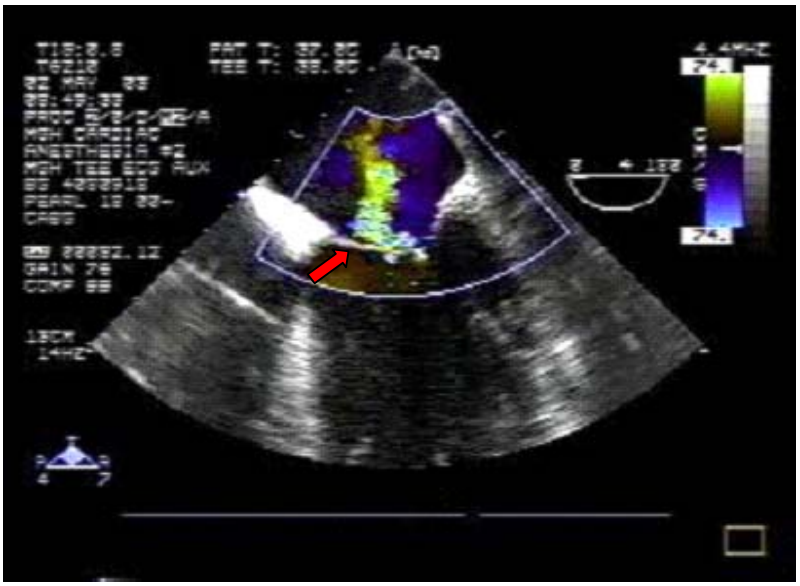

Figure 7.2. Color doppler image of patient with ischemic mitral regurgitation. The red arrow shows a tethered anterior leaflet in the area of strut chord insertion. This tethering results in regurgitation jets as shown by the yellow retrograde flow.

7.3.2 Chordal Force and Stress Distribution after Ventricular Remodeling or Dilation

The PSFs measured for the different PM positions varied from results presented in a previous *in vitro* study [66]. These differences may be attributed to variations in the PM displacements used in the two studies and the use of glutaraldehyde to preserve the valves in the aforementioned study, as glutaraldehyde has been shown to affect valve mechanics [132]. The average PSFs for the primary (marginal) and secondary (intermediate) chords in the defined normal PM position were within ranges observed previously *in vivo* [71].

Therefore, the pressure driven loading on these chords were within physiological ranges [71].

Apical displacement, as expected, significantly increased the force and subsequent stress on the anterior strut chord. When the PMs are displaced apically, the coaptation geometry of the mitral valve changes. Apical displacement generates tented leaflet geometries, as observed in previous studies [65], [51], [84], [129-131]. With a tented geometry, the intermediate chords restrict leaflet motion, and therefore these chords hold higher loads during valve closure. The results of this study for the anterior strut chord were in clear agreement with the aforementioned phenomenon as apical displacement of the PMs tented the leaflets, and significantly increased the load on the anterior strut chord. The decrease in force when repositioning the PMs from position 500 to position 505 was probably related to the redistribution of the load between chords as a consequence of the posterior motion of the PMs. In addition to the increase in force (41±23% or 0.4±0.28N) and subsequent stress associated with apical displacement, the transition from a saddle annulus to a flat annulus induced an additional increase in load of approximately 0.27N (18.5±16.1%). Therefore, when coupling the effects of variation in annular shape and PM repositioning, there was an increase of approximately 42% in stress reaching a peak value of 0.69±0.45MPa in position 555 when compared to the stress in the normal annular configuration (SR=20%) and normal PM position. Considering a 42% change in functional load and a constant failure stress, simultaneous annular flattening and PM relocation to position 555 decreases the safety factor for this chord from 20 to 14.

Posterior PM displacement decreased the force and subsequent stress on the posterior intermediate chord by approximately 37%. Posterior motion of the PMs shifted the

coaptation line posteriorly, reducing the area of the orifice covered by this leaflet and decreasing the insertion angle of this chord (Figure 7.3).

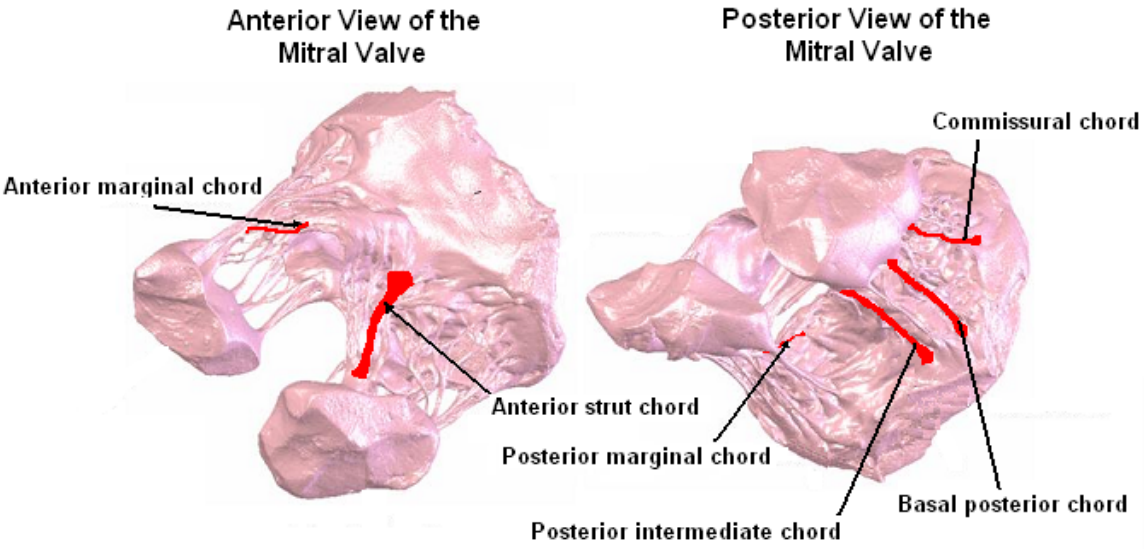

Figure 7.3. Anterior and posterior view of microCT reconstruction of a porcine mitral valve. The chords which were instrumented with C-ring force transducers are identified and highlighted in red.

Both of these alterations reduced the resultant force vector. The increase in force/stress associated with position 500 is explained by the same tenting described for the anterior strut chord. Combined apical-lateral displacement induced a significant increase in force due to tenting of the leaflet and the stretching and redirection of the posterior intermediate chord. This effect was reduced in position 555 because of the posterior motion associated with this position. When evaluating for the posterior intermediate chord with simultaneous annular flattening and apical PM relocation, the results show how the increase in force due to apical PM displacement (positions 500 and 550) is compensated by the decrease in force associated with annular flattening (transition from saddle to flat annulus). This compensation in force explains why there was no significant

difference between the valve in the normal PM position and 20% SR saddle configuration when compared to the valve in positions 500 and 550 in the flat annulus configuration.

The forces and associated stresses on the anterior marginal and posterior marginal chords were relatively unchanged for the different PM positions. Since the marginal chords control coaptation at the tip of the leaflets (Figure 7.3), loading on these chords may be less sensitive to changes in PM position. Peak systolic forces for these chords were small in magnitude considering that measurements under 0.01N could not be distinguished from electrical crosstalk. Hence, small variations in force for these chords may not be detectable by the methods used in this study.

The force/stress on the posterior basal chord was highly sensitive to PM displacement. Posterior displacement reduced the force and therefore the stress on the posterior basal chord as it redirected the angle of the chord. This motion reduced the septal-lateral component of force, and thus, reduced the overall resultant force. As chordae tendineae have a non-linear mechanical response to elongation [56], [57], prestraining due to apical displacement increased the force and therefore stress on the basal posterior chord. A prestrained chord will be subjected to a higher force (compared to an unstrained chord) for a similar strain during coaptation. Lateral displacement of the PMs reduced the force on the basal posterior chord. This reduction was probably due to a redistribution of the load among other chords.

The commissural chord selected for these experiments inserted near the annulus and below the septal-lateral midpoint of the valve (posterior section of the valve- Figure 7.3). Therefore, trends in force/stress variation due to PM displacement are similar to those present in the basal posterior chord. Similarly, prestraining increased the force and

subsequent stress on the commissural chord during apical motion of the PMs. In addition, both posterior and lateral relocation of the PMs decreased the force and therefore the stress on these chords. The relative contributions of these motions (lateral-posterior) to the force on the commissural chord should be different than the contributions to the force of the basal posterior chord because their orientation with respect to the annulus plane and the location of their insertion into the valve differ (Figure 7.3).

During the cardiac cycle, the valve is in a very dynamic environment characterized by annulus displacement, ventricular motion, and PM contraction. Within this environment, the basal chords maintain a relatively constant distance from the tips of the PMs to the annulus [71], [128], aiming to maintain overall valve geometry and isolating the motion of the leaflets from the movement of the surrounding environment. The geometric and anatomical construction of the mitral valve must ensure that the chords controlling coaptation, particularly the marginal chords that control the appropriate seal of the valve, are less sensitive to the changing environment. Therefore, as expected the intermediate chords were less sensitive to changes in PM position than the basal chords, whereas the marginal chords were the least sensitive of all chordal types to variations in PM position. These characteristics were clearly shown by the variability of the forces associated to different PM positions for a specific chord.

The direction of the displacement of the PMs was directly related to what type of chord was subjected to altered forces and to the level of mitral regurgitation. Apical displacement affected the force on the secondary chords of both leaflets while inducing at the same time tented leaflet geometries and regurgitation. Posterior displacement of the PMs tended to reduce the force on chords which inserted into the posterior leaflet.

Posterior and lateral displacements by themselves did not increase regurgitation, although combined lateral and posterior displacements did increase regurgitation, but not to clinically significant levels. The forces on the chords which inserted near the annulus were affected by displacement of the PMs in all directions.

The maximum stress measured in any of the different papillary muscle positions were on average 0.86MPa (position 550) for the anterior strut chord, 1.02MPa (position 005) for the anterior marginal chord, 0.7MPa (position 550) for the posterior intermediate chord, and 0.2MPa (position 505) for the posterior marginal chord. The safety factors calculated for these maximum pathological stress based on the failure stresses in Table 2.1 were 11, 12, 16, and 39, respectively. Therefore, even under pathological conditions associated with ventricular dilation spontaneous chordal failure due of overloading should not occur. These results support previous research, which associated chordal failure in ischemic or dilated cardiomyopathy patients to a combination of tissue remodeling [87] and accumulated damage [88].

7.4 The Repaired Mitral Valve

7.4.1 Alfieri Stitch Repair

Several clinical studies have demonstrated that without concomitant annuloplasty the long-term results of edge-to-edge repair are suboptimal [98]. The results of this study showed that after symmetrical displacement of the PMs and with approximately 20% dilation of the mitral annulus, significant regurgitation was still present after the edge-to-edge repair. Although decreasing annular size resulted in a significant decrease in mitral regurgitation (MR), modest regurgitation still persisted in the normal annulus

configuration. Further contraction of the annulus did not significantly decrease this modest residual MR resulting from PM displacement.

The current study also demonstrates that on average the Alfieri stitch alone decreased effective orifice area (EOA) by approximately 16%, which may be characterized as an insignificant to mild level of MV stenosis. When both annular under-sizing and the Alfieri stitch were present, the EOA is reduced by approximately 33%, which represents a moderate level of MV stenosis. Therefore, although concomitant annuloplasty improves the efficiency of the edge-to-edge repair, correct sizing of the annuloplasty ring is essential. These results agree with previous clinical and animal studies which showed that the edge-to-edge repair when correctly performed did not cause functional MV stenosis [95], [96]. Nielsen *et. al.* 2001 and Timek *et. al.* 2004 used force transducers similar to those used in the present study to measure Alfieri stitch force (F_A) in sheep during the cardiac cycle. F_A curves in these *in vivo* studies and in the current *in vitro* study showed two peaks during the cardiac cycle: one peak during systole, and a second during diastole. Peak F_A values obtained in the present study are smaller than those observed in the aforementioned *in vivo* studies, but are of the same order of magnitude. Most of the discrepancy in the magnitude and differences in the F_A curves are due to the location of the force transducer.

In the *in vivo* studies the transducers were attached to the atrial side of the leaflets, whereas in the current *in vitro* study the transducers were placed on the ventricular side. In the present study, the transducer was zeroed under zero flow and zero transmitral pressure conditions in the simulator, since in the normal valve configuration the leaflets do not need to be pulled together. In the *in vivo* studies [100], [101] under normal annular

conditions, the leaflets are brought together (on-pump – passive heart) and thus there was a static force under zero flow and zero trans-valvular pressure. Thus, the *in vivo* F_A curves show a minimum F_A magnitude of approximately 0.1N during the entire cardiac cycle (Figure 7.4A). This offset (static force) is associated with bringing the leaflets together in order to position the transducer on the ventricular side. In order to prove that the discrepancy between the curves was mostly associated with transducer placement, an experiment was conducted following the protocol used by the researchers in the *in vivo* studies [100], [101]. As shown in Figure 7.4, when the transducer was placed on the atrial side of the leaflets the F_A curve was similar to that observed *in vivo* [101].

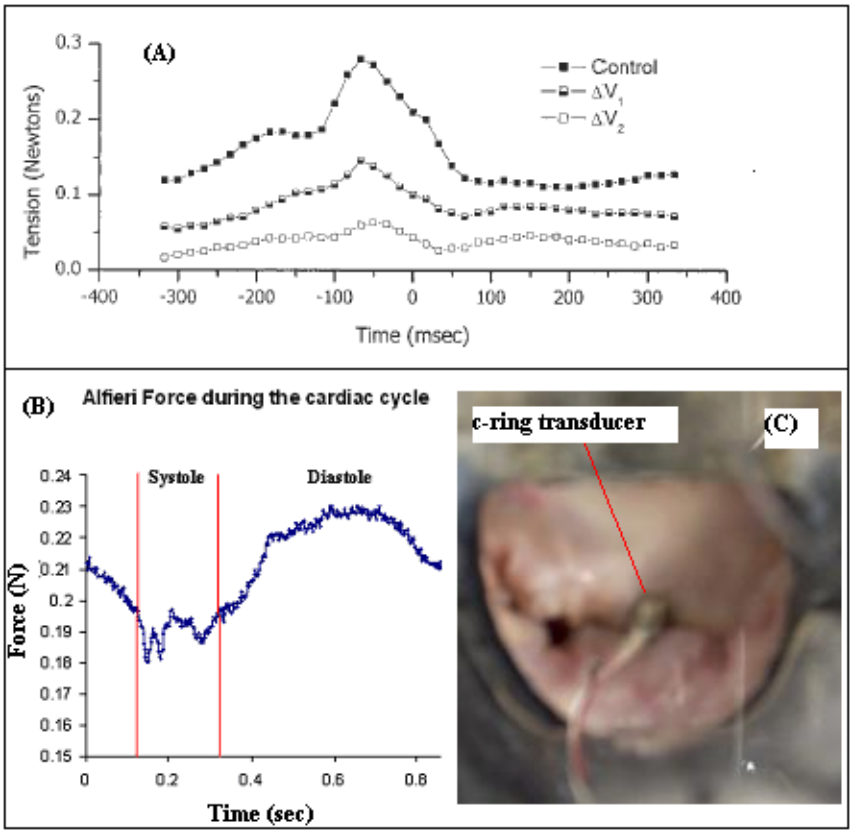

Figure 7.4. (A) Alfieri force curves from *in vivo* ovine model Timek *et. al.* 2004 [101]. (B) Alfieri force from an *in vitro* experiments using the same transducer location described by Timek *et. al.* 2004. This experiment was conducted using a CO: 5L/min and a transmitral pressure of 120mmHg. (C) Photograph of the mitral valve and c-ring force transducer from the atrium of the Georgia Tech left heart simulator.

The change in transducer location induces a baseline shift that increases F_A to similar magnitudes to those obtained *in vivo* [101]. Therefore, most of the discrepancies between the present study and previous *in vivo* studies were due to transducer location. The *in vitro* transducer location was aimed at minimizing interference with leaflet motion, which Nielsen acknowledged as a possible limitation of their *in vivo* experiments [100]. *In vivo* annular contractility and differences in valve size may have also contributed to the aforementioned differences in F_A magnitude between the studies.

These *in vivo* studies [100], [101] also showed that the diastolic peak was dominant during the cardiac cycle. This was also observed in the present study under normal annular conditions. In the same study, Nielsen *et. al.* 2001 showed that in sheep with ischemic mitral regurgitation F_A increased during both systole and diastole, when compared to normal sheep. The most significant increase was observed at end systole [100]. These results agree with the present study as the results showed that peak F_A during systole increases linearly with mitral annular area (MAA).

Nielsen *et. al.* 2001 reported end-systolic mitral annular areas of $720\pm40mm^2$ and $820\pm50mm^2$ in normal and ischemic sheep, respectively, corresponding to an annular dilation of approximately 14%. In Nielsen's study the left ventricular pressure decreased in the ischemic sheep, and the level of dilation was smaller compared to the annular dilation used in the current study. These two differences may explain why Nielsen did not observe that peak systolic F_A becomes dominant in the presence of annular dilation, as demonstrated in the present study. Under normal annulus conditions the Alfieri stitch only helps the tips of the MV leaflets to initially coapt. With annular dilation coaptation length decreases [84], and therefore the leaflets are brought together with the stitch. In

such conditions, a non-zero baseline in F_A is present due to the force needed to bring the leaflets together. In the present study, the non-zero baseline associated with pulling the leaflets together was not present due to the relatively small increase in annular septal-lateral diameter in the dilated configuration of the annulus model.

Nielsen *et. al.* 2001 and Timek *et. al.* 2004 also reported a positive correlation between annular septal-lateral diameter and diastolic F_A [100], [101], contradicting the findings of the present study in which a negative correlation between diastolic F_A and MAA was revealed. During diastole the leaflets are pulled apart by the flow through the valve, and the force on the leaflets is directly related to the surface area of the leaflets and force imparted by the passing fluid. During diastole the Alfieri stitch prevents the tips of the leaflets from separating completely. Thus, F_A is determined to a large extent by mitral flow rate (MFR). Under normal *in vivo* conditions the mitral annulus expands during diastole. Therefore, the positive correlation between septal-lateral diameter and F_A found in previous studies [100], [101] was mostly due to the increase in flow through the valve. To some extent this positive correlation was also due to annular expansion. But the component of force associated with annular expansion is artificially magnified due to transducer placement, since the stitch has a non-zero baseline in the normal valve configuration. The negative correlation found between F_A and MAA in the present study may be explained by physics. At a constant flow rate, decreased orifice cross-sectional area will result in increased velocity. The increase in velocity during diastole will increase the force on the leaflets and subsequently F_A.

7.4.2 The Effects of Annuloplasty Ring Geometry on Anterior Leaflet Strain

The marker technique has been used in previous studies in order to calculate the strain and stretch on the leaflets of the mitral valve [12], [13], [133]. Previous *in vitro* [12] and *in vivo* [133] studies have shown that mitral valve leaflet material exhibits anisotropy, a non-linear load-strain relation, and hysteresis. As a result, these studies had characterized the material as viscoelastic. Further analysis of *in vitro* [12] and biaxial data [41] demonstrated that although mitral valve leaflet material exhibits the aforementioned characteristics, it does not exhibit creep or strain rate dependence for its response, and therefore, this material should not be characterized as viscoelastic, but rather as quasi-linear-elastic. In the current study, the central region of the anterior leaflet presented anisotropy, non-linearity, and hysteresis in agreement with previous literature [12]. As described in Section 7.1 and in previous studies [12], [13] the anisotropy, increased circumferential stiffness, and non-linear load-strain relationship are associated with collagen fiber orientation and crimping. In addition, the peak areal stretch of 1.44±0.14 (flat annulus) measured in the current study agrees well with the 1.47 peak areal stretch obtained in a previous study [12] under similar conditions using a flat annulus configuration. The systolic stretch curves have similar loading characteristics as those observed *in vivo*, presenting rapid deformation rates followed by a stretch plateau [133]. The peak stretches in the current study were smaller than those observed *in vivo* in sheep, but these differences may be mostly attributed to methodological and inter-species variability [133].

As demonstrated by results of this study there was a significant reduction in the areal stretch in the central region of the anterior leaflet as a result of increasing saddle curvature. Most of the reduction in stretch occurred in the radial direction. The decreased

septal-lateral diameter associated with increasing saddle height reduces the radial distance between the coaptation line and the anterior annulus. Therefore, the unsupported length of the anterior leaflet decreases, limiting its radial deformation.

In contrast, the circumferential stretch appeared to be less sensitive to saddle curvature, although at 30% SR compression appeared in two of the specimens. In the circumferential direction, peak strains were relatively small (between 7-10%), and therefore may be reached rapidly. Additionally, the constant commissural diameter for the different SR configurations and the symmetric insertion pattern of the chords, severely restricted the circumferential curvature of the leaflets. The small strain range and the restrictions to circumferential leaflet curvature may both be responsible for the relative insensitivity of circumferential strain to saddle curvature (SR 0%-20%). At 30% SR there was a significant increase in curvature resulting in compressive strains in two of the specimens during peak systolic loading. Peak systolic circumferential compression constitutes abnormal loading for the central region of the anterior leaflet. Peak systolic compression in the central region of the anterior leaflet was not observed under normal annular (SR=20%) conditions and has not been reported by other researchers [12,] [13], [133]. Abnormal loading may lead to abnormal tissue response or remodeling. Furthermore, compressive circumferential loading in a layered structure, such as the mitral anterior leaflet, may have deleterious effects such as delamination.

Although this is the first experimental study that describes the relationship between leaflet strain and annular curvature, one computational study previously explored the relationship between saddle annular curvature and leaflet stress [8]. Salgo *et. al.* 2002 showed that both billowing and circumferential curvature, by themselves or in

combination, reduced the stress on the mitral leaflets. At a saddle height to commissural diameter ratio of 20%, leaflet stress was reduced three fold (300%) to its minimum. The reduction in strain in this study is significantly lower than the reduction in stress observed in the computational model [8].

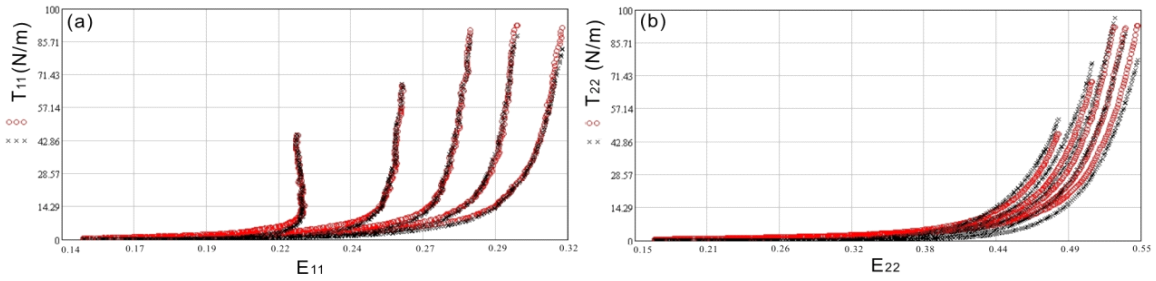

Figure 7.5. Results from biaxial testing of the anterior leaflet of the mitral valve from experiments performed by Grashow *et. al.* 2006 [41]. Structural model fit to the biaxial mechanical data for mitral valve anterior leaflets. r^2 for T_{11} (circumferential direction) is 0.993 and r^2 for T_{22} (radial direction) is 0.976. Open circle represents the experimental data.

As shown in Figure 7.5, stress increases exponentially with increasing strain. Using this biaxial data [41] and strain data from the current study, a decrease in stress of approximately 2 fold may be expected in the SR 20% configuration when compared to the stress in the flat annulus configuration. The remaining differences between the studies are related to the methodologies, but more importantly to the simplifications of the computational model [8]. The absence in the computational model of chordae tendineae, which restrict leaflet curvature, and the use of a nonlinear material constitutive model, which does not account for tissue stiffening that decreases deformation, explain the larger reductions in stress observed in the Salgo *et. al.* 2002 computational model.

As observed in the results of the current study, increasing SR reduces the strain on the central region of the anterior leaflet. In the 30% SR configuration, abnormal compressive loading (during the systolic plateau) was observed in the central region of the anterior

leaflet. Therefore, a mechanically optimal strain configuration was obtained at the 20% SR configuration, since it minimized leaflet strain without inducing compressive loading in any of the specimens.

7.5 Limitations

There are several limitations associated with both the apparatus and the methodologies used in this work. An initial limitation of this study is associated with the interspecies variability between porcine and human valves. Porcine mitral valves were used in this study because of the limited availability of human mitral valves. Unfortunately, this situation occurs in all studies that utilize human organs/tissues. Porcine mitral valves bear the closest resemblance to human mitral valves. Because of their functional similarity porcine mitral valves have been used as implants for humans. Previous studies have also shown similar chordal force distributions between porcine and human mitral valves under physiological conditions, validating the chordal force measurements in the current study [120]. Although the lengths for human and porcine chords are similar [58], differences in chordal thickness may exist. Therefore the magnitudes of chordal stresses in human valves may be slightly higher or lower depending on human chordal cross-sectional area. Although the chordal stress magnitudes may vary, stress distributions and chordal stress variations associated with PM positions or annular geometry should be similar since they are directly dependent on variations in load. Leaflet strain fields have not been measured in human mitral valves under physiological loading; therefore, there is no data to directly validate these results. Similarities in the microstructure, composition, and geometry of human and porcine leaflets suggest that comparable leaflet strain behaviors may be

expected from normal human mitral valves. In pathologies such as myxomatous disease [77-80], dilated cardiomyopathy [86], [87] and ischemic mitral regurgitation [86], [87], changes in the mechanical properties of human mitral valve tissue have been reported. Therefore, further research is warranted to observe how these changes in mechanical properties affect the mechanical and hemodynamic function of the mitral valve under pathological conditions.

Even though the same six chordae tendineae were carefully selected for C-ring implantation, their size and branching varied from valve to valve. MV leaflet geometry, coaptation geometry, and coaptation line location also varied from valve to valve although a standard normal position was used. Because of this natural variability, the standard deviations for the chordal force results were high. Normalizing force distributions using the loads measured under normal conditions aided in reducing this variability.

As described in section 7.3, the forces measured in this study were only those associated with trans-mitral pressure as diastolic force was considered baseline. The baseline tethering force for the different PM positions was not measured since stress relaxation due to the viscoelastic nature of the chords induced baseline shifts that were significant over the course of an eight hour experiment. Since diastolic force was considered as baseline, the force offset induced by the minimal weight (<80mg in air) of the C-ring force transducers should not have affected the chordal force measurements. Peak systolic forces for the marginal chords were small in magnitude considering that measurements under 0.01N could not be distinguished from electrical crosstalk. Thus, small variations

in force for these chords may not be accurately characterized with the methods used in this study.

The left ventricle heart simulator had several limitations, but it has successfully been used in several pioneering studies [7], [12], [13],[65], [68]. Although the pressure and flow conditions generated in this loop are physiological, it does not reproduce phenomenon such as ventricular, atrial, annular, or papillary muscle contractions since it is a rigid model. Therefore, force measurements, in particular those on the basal chords, may have different magnitudes to those found *in vivo*.

Although under the pathological conditions of interest, most annular dynamics is lost, sphincteric annular contraction may have a significant influence on F_A under normal annular conditions. This annular contraction was not replicated by the *in vitro* model. In the current study annular dilation is relatively moderate and thus the baseline F_A required to pull the leaflets together under pathological conditions was minimal. Thus, further research with larger levels of dilation is warranted. The use of a transducer to hold the leaflets together instead of a single stitch may not completely simulate the clinical setting. Nevertheless, we believe that the current transducer location obstructs leaflet motion and flow less than the placement used by other researchers in previous studies [100], [101].

The regurgitation volumes measured in specific aim 2 are clinically small, representing a range of regurgitation fractions of 14% to 30%. These volumes are relatively small considering the large PM displacements used under the pathological conditions. Generally, under pathological conditions, several alterations occur simultaneously (annular dilation, papillary muscle dis-coordination, ventricular malfunction, etc.). Therefore, varying a single variable within the valve, as in this study, may lead to lesser

regurgitation volumes. In parallel, symmetric displacements of the PMs have been shown to cause less regurgitation than asymmetrical displacements [84]. Therefore, the strict control in the symmetrical displacement may have also lead to smaller regurgitation volumes.

The marker technique has been validated to measure mitral leaflet strain both *in vivo* and *in vitro* [12-13], [133]. Optical access is the major limitation associated with the marker technique since only discrete regions of the valve may be studied at a given time. In addition, because of the size of the data sets, strain measurements could only be acquired for a single cardiac cycle. Averaging over several cycles may provide more representative results.

The present *in vitro* methodology provided good control over the variables of interest, and since this is a comparative study, the shortcomings of the model should not have a significant impact on the conclusions.

7.5 Clinical Relevance

The clinical relevance of this study is associated with cardiac device design and surgical technique development. Annular flexibility and dynamics have been shown to be important to mitral valve function and mechanics [9]. Although previous studies have shown that annular shape does not significantly affect mitral regurgitation [7], the normal shape of the mitral annulus should be restored after repair procedures. Restoring annular geometry may optimize the mechanical loading on the valve according to the results of this study. Repair procedures such as annuloplasty should try to restore the normal configuration and flexibility of the annulus. An optimal annuloplasty ring should restore

both annular size and curvature, but be flexible enough not to interfere with annular dynamics. This type of ring could have an impact on repair techniques for diseases such as myxomatous degeneration, since restoring saddle curvature could reduce stresses on the central region of the leaflets. In most myxomatous valve repairs, leaflet resections are performed leaving suturelines in the central regions of the leaflets. Thus, the use of saddle shaped annuloplasty rings may reduce sutureline stresses and may consequently improve repair durability. Since in myxomatous MV disease some annular dynamics may still be preserved, repairs using flexible annuloplasty rings may provide functional benefits, if they do not restrict these dynamics (Currently most flexible rings restrict annular dynamics [25]).

In patients with ischemic mitral regurgitation and dilated cardiomyopathy most of annular dynamics are lost due to changes in ventricular dynamics [18]. Therefore using a flexible or rigid annuloplasty ring for repairs associated with these pathologies should not make a significant difference in terms of annular mechanics or function. Additionally, a saddle shape annuloplasty ring may not contribute as significantly to leaflet stresses in a dilated ventricle since the leaflets are tethered and tented because of PM displacement. In order to provide some insights for these points of discussion, further research on the effects of annular shape on leaflet stress/strain under conditions associated with ventricular dilation is warranted.

The effects of PM displacement are transmitted to the leaflets through the chords. Therefore, physicians have proposed surgeries such as chordal cutting or translocation as a solution to different types of regurgitation. Surgeons have observed that cutting the marginal chords induces severe regurgitation, but that in some pathologies cutting the

intermediate chords may decrease leaflet tenting leading to better coaptation and decreasing regurgitation [109]. Some surgeons are reluctant to use these procedures because cutting the secondary chords may induce significantly higher loads on other chords that may eventually fail due to structural deterioration. As shown by the results of this work, the secondary chords do carry the highest loads and therefore are structurally relevant to mitral valve function. The increased load on other chords (such as the marginal chords) generated by cutting the intermediate chords may have deleterious effects on valve mechanics.

This study also provides important information that may be used to improve the durability of chordal transfer procedures. The results show how different types of chords (marginal, intermediate, and basal) are subject to different degrees of loading. Previous research has shown that marginal, intermediate, and basal chords had different microstructures, which translated into differences in mechanical properties [56-57]. Therefore, chords that are transferred to repair a damaged valve should probably be of the same type as the chord they will replace. Also, since chordal types are designed for bearing different loads, a transferred chord, if not of the appropriate type, may rupture under its new loading conditions, completely obliterating the objective of the surgery. Since anterior leaflet chords are relatively thicker and may sustain higher loads before failure [56], transferring anterior chords to the posterior leaflet may prove to be safer than transferring chords from the posterior leaflet to the anterior leaflet (the latest being common practice for anterior leaflet prolapse). Because of the elevated security factors associated with the normal and pathologic function of these chords there is some laxity in terms of which chords may be transferred to different locations. Still, normal,

pathological loading conditions, and failure stress should be considered in the selection of the chords to be transferred in order to improve its durability of the repair. Furthermore, since the results from this work support previous research that associated chordal failure in absence of congenital, degenerative, or infective valvular disease to remodeling [87] and accumulated damage [88], long term follow up for patients with transferred or repaired chords is warranted.

For years PM displacement has been identified as an important contributor to mitral regurgitation [10], [21], [39] ,[65], [84]. The results of the current study propose that apical displacement of the PM is a major determinant of mitral regurgitation in patients with ventricular dilation or remodeling. Thus, surgical procedures or implants should restore the apical distance between the annulus and tips of the PMs. Restoring this distance may alleviate leaflet tenting and subsequent regurgitation. Currently some repair techniques [33] and devices such as the Coapsys system [34] are used to restore the position of the PMs. But in most cases these systems or techniques restore their lateral position. These new techniques may increase their efficacy if they were aimed at restoring the apical position of the PMs.

Generally, the edge-to-edge repair is accompanied by concomitant annuloplasty, since recent studies have shown suboptimal results when performing the edge-to-edge technique without annular resizing [98]. The development of edge-to-edge techniques without concomitant annuloplasty is important because this increases the feasibility of repairing the MV using less invasive approaches [102-103]. Therefore, understanding the effects of annular size on MV function and mechanics after the edge-to-edge repair is fundamental not only to understanding current repair procedures, but also for the

development of future techniques and implantable clips. The results from the present study confirmed previous clinical findings which demonstrated that under dilated annular conditions, an isolated edge-to-edge repair will not be sufficient to address mitral regurgitation [94], [97], [98]. Moreover, with increasing mitral annular area, peak systolic F_A increased and became dominant. Therefore, annular dilation negatively impacts the efficacy and durability of the edge-to-edge repair. The previous statements imply that the Alfieri technique, even in minimally invasive embodiments, should be accompanied by some sort of annular resizing or stabilization.

CHAPTER VIII

CONCLUSIONS

Although not all conditions of mitral annular mechanics were replicated, this study measured the chordal stress distribution and anterior leaflet strain of the normal mitral valve. The current study also elucidated the effects of PM displacement on chordal stress distribution and mitral valve function, simulating conditions found in pathologies associated with ventricular remodeling and dilation. In addition, the effects of annular size, transmitral pressure, and mitral flow rate on the edge-to-edge repair were explored in the section on mitral valve repair. Finally, the effect of annular shape on anterior leaflet strain was also studied in order to improve the understanding of leaflet mechanics after annuloplasty.

The chordal force distribution in the normal mitral valve is characterized by the intermediate chords holding the largest forces on their respective leaflets as compared to the forces carried by the marginal chords. In contrast, the stress on the anterior marginal chords was higher than the stress on the anterior strut chord in the normal valve configuration. The intermediate and marginal chords held similar stresses on the posterior side of the valve. The strain field on the central region of the anterior leaflet was characterized by a highly anisotropic behavior with a non-linear load-strain response under normal hemodynamic and geometrical conditions. The strain field was also

characterized by hysteresis during the loading and unloading phases of closure and cessation in deformation during peak systolic pressure.

The results presented in this study also demonstrated that apical motion is the most important contributor of PM relocation to mitral regurgitation. Apical displacement of the PMs increased the force on the intermediate chords, inducing leaflet tenting and subsequent mitral regurgitation. Chords on the posterior side of the valve were subject to a reduction in force after posterior motion of the PMs. Chords which insert near the annulus were affected by lateral, posterior, and apical displacement of the PMs. The results also revealed that variation in tension due to PM relocation decreased with increasing distance of chordal insertion from the mitral annulus. Chords which insert near the annulus are the most sensitive to variations in papillary muscle position, whereas chords which insert into the tip leaflet are the least sensitive to PM relocation.

The results from the section on the Alfieri repair established that the edge-to-edge repair alone will not eliminate mitral regurgitation in the setting of annular dilation. The edge-to-edge repair with concomitant annuloplasty does not cause significant functional mitral valve stenosis as long as the annuloplasty reduces the annulus to its normal dimensions. Mitral flow rate and transmitral pressure are the main determinants of changes in F_A during the cardiac cycle and may be used in conjunction with MAA to approximate the magnitude of the force on the Alfieri stitch. Although F_A during diastole decreases with increased annular area, systolic F_A increases and becomes dominant with annular dilation. Therefore, correctly sized concomitant annuloplasty is required to improve the long-term results of the edge-to-edge repair both in terms of efficacy and durability.

The current study also demonstrated that, independent of SR the behavior of the central region of the anterior leaflet is highly anisotropic with a non-linear load-strain relationship. Although the mitral valves had similar overall response to loading, the degree of deformation significantly varied for the different annular curvatures. There was a significant reduction in the areal stretch in the central region of the anterior leaflet as a result of increasing saddle curvature. Most of the reduction in stretch occurred in the radial direction. In contrast, the circumferential stretch appeared to be less sensitive to saddle curvature. Compression may occur at a saddle height to commissural ratio of 30% due to significant increase in circumferential curvature. Therefore, at a saddle height to commissural ratio between 20% and 30% a functionally optimal strain configuration may be obtained for the central region of the anterior leaflet. Decreased leaflet strain and associated stress resulting from increased annular saddle curvature may improve mitral valve repair durability after annuloplasty.

In summary, the normal geometry of the native mitral valve optimized its function and mechanics. Under pathological conditions associated with ventricular dilation, significant alterations to mitral valve function and mechanics were present. Although the studied repair techniques may have substantially restored valve function, severe alterations to the mechanics of the valve still persisted.

CHAPTER IX

RECOMMENDATIONS

The variable annulus shape atrial chamber was designed to mimic static geometrical conditions found during peak systole. However, a truly physiological annulus model which dynamically varies the curvature and size of the annulus during the cardiac cycle should be designed and constructed. In order to improve the force measurements on the marginal chords, smaller and more sensitive transducers should be used. In addition, animal studies aimed at measuring the force on the basal chords should be conducted as there is no *in vivo* force data available for these chords. This study will not only provide important information on chordal force distribution, but it will also provide important information on PM function and its implications. Another important factor that should be simulated in future work is PM function including contractility. This will allow the research group to study a larger range of physiological and pathological conditions. The contraction force of the PMs must be characterized *in vivo* in order to conduct these studies simulating PM function *in vitro*.

Abnormal valves should be mechanically characterized and studied under normal and pathological conditions in order to better understand the nature of the associated diseases. Repair procedures including but not limited to leaflet resection, chordal translocation and replacements, and annuloplasty with different ring geometries should be reproduced *in vitro* using diseased valves to observe the effectiveness of the proposed correction methods. To complement the work presented here, two additional studies should be

conducted: 1) A study of the effectiveness of the Alfieri repair in the setting of annular dilation and symmetric or asymmetric PM displacement; 2) A study of the effects of annular saddle curvature on leaflet mechanics and mitral valve function under conditions associated with ventricular dilation.

Finally, a computational model of the mitral valve with a realistic geometry and accurate material properties should be developed. The model should be able to simulate mitral valve function over the entire cardiac cycle for different physiological and pathological conditions. This tool will not only provide fundamental information on mitral valve mechanics, but at some point in time, may be used as a simulator for the design of new repair procedures and may aid surgeons in surgical planning.

APPENDIX A

C-RING FORCE TRANSDUCERS

Materials and Assembly

These C-transducers use the well-known Wheatstone bridge to measure force. Half of the Wheatstone bridge is active with two uni-axial strain gauges (SG) (the two R_G's in Figure A.1) and the other bridge-completing half consist of two passive resistors with the same nominal resistance as the active SG's. The passive resistors are located inside an in-house built signal conditioner (R_1 and R_2 in Figure A.1).

R_1 and R_2 are adjustable with potentiometers coupled in parallel to the passive resistors. As mentioned below, the SG's nominal resistance (350 Ohms) will change slightly when they are glued, soldered, and coated. For optimum performance, the Wheatstone bridge needs to be balanced. The balance can be achieved by adjusting the aforementioned potentiometers. A serial connected resistor, Rs in Figure A.1, is used to reduce the power dissipation in the SG's. One SG is attached to the inner surface and the other SG is attached to the outer surface of the C-frame. The C-frame is shown in Figure A.2. When the ends of the C are pulled from each other, the outer SG will compress decreasing its resistance ($-\Delta R$), whereas the inner SG will elongate so its resistance will increase ($+\Delta R$). The variation in resistance will change the output voltage, V_O, which can be then measured. As long as the C-frame is not deformed plastically and the applied force is below 6N, the output voltage, V_O, will change linearly with force.

Changes in temperature can be a problem when using SG's, however, assuming that the temperature changes are identical in the two gauges, the ratio of their resistance does not

change, and the output voltage, V_O, will not change with fluctuations of temperature. In order to prove these assumptions calibration experiments were conducted at different temperatures.

The resistance changes in the SG's are quite small. Amplification of the Wheatstone bridge output voltage is required for further data acquisition.

Strain gauge input modules (SCM5B38-03, Dataforth) are made especially for data acquisition and to be used with strain gauges in a Wheatstone half bridge. Their output range is ±5 Volts, which is a range compatible with most data acquisition cards. They provide a stable, fully isolated excitation voltage (V_{EX} on Figure A.1) of 3.333 V when assembled in half bridges with bridge resistors in the range of 100 Ω to 10 kΩ.

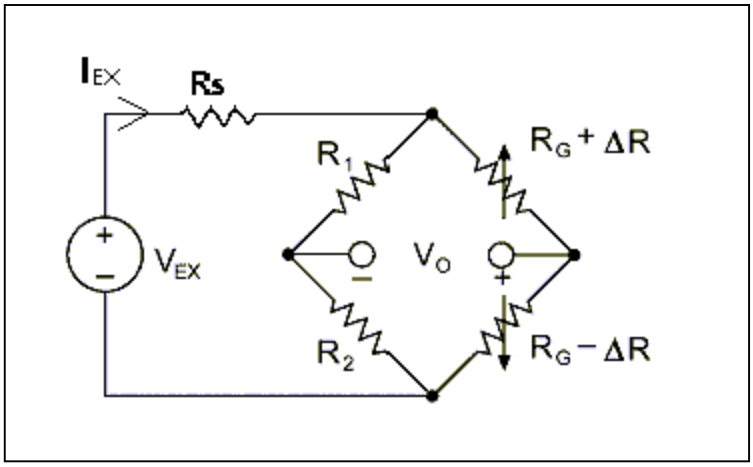

Figure A.1. Diagram of the bridge circuit with series resistor, R_S. Each of the other resistors has a nominal value of 350Ω. V_{EX} is the Wheatstone bridge excitation voltage and is provided by the SG input modules. V_O is the output voltage of the bridge.

The C-frame is made of brass as it is a ductile and corrosion resistant metal within the specified working environment. Furthermore, stresses generated by chordal forces are

within the elastic range of brass. Therefore, for this geometry, brass is mechanically appropriate.

The frame for the C-transducer is cut out from a brass pipe (Figure A.2) with an outer diameter of 6.0mm and inner diameter of 5.0mm. The pipe is sawed into rings, each with a width of 2.0mm. Four holes are drilled (diameter: 0.9mm) in each brass ring. This is accomplished by drilling through the ring twice, perforating two sets of holes, each set opposite of each other. A notch is cut in between the two holes in each end of the C-frame. Rough edges are filed down providing a smooth surface all over the plate.

Figure A.2. C-frame made of brass.

After the C-shaped brass frame has been constructed, it is cleaned with degreaser (CSM-1A Measurement Group©, Raleigh, NC, USA), which is applied with a cotton swab.

After the surface has been degreased the area where the SG will lay, is conditioned using M-Prep Conditioner A (Measurement Group©, Raleigh, NC, USA). The last cleaning step of the SG surface area serves to chemically neutralize it by applying M-Prep Neutralizer 5A (Measurement Group©, Raleigh, NC, USA). The mounting areas to which the SG's will be attached too are now chemically clean and pH neutral.

To ensure an adequately smooth surface at the attachment sites for the SG's and to ensure electric insulation, the areas are bonded using M-Bond 43 B (Measurement Group©, Raleigh, NC, USA). The bonding solution is applied to the area between the two inner holes on the concave and the convex surfaces. To cure the bonding material properly, the C- frames with the bonding solution are heated for an hour at approximately 125°C. Three coats of the solution are applied and cured sequentially. No external element should be in contact with the bonding area during curing.

When the brass frame has been bonded three times, the surface area is smooth enough for SG attachment. The miniature SG's utilized are model EA-06-031DE-350 (Measurement Group©, Raleigh, NC, USA). Their nominal resistance of 350 Ohms is appropriate for the 3.333 Volt Wheatstone bridge excitation voltage considering sensitivity, power dissipation, and noise. The SG's are attached to a foil. The foil is 2 mm x 4 mm, however; the actual gauge area is only 1 mm x 3 mm. Therefore, cutting the area around the actual gauge using a scalpel or scissors is necessary.

An appropriate amount of ordinary super glue is applied to the area where the SG will be placed on the brass frame. The SG is held down to the surface with tweezers and when in contact with the super glue it is adjusted to the right location (The middle of the gauge on the middle of the brass frame). When the SG is in the right location, a thin metal thread (for example the 134-AWP Single Conductor from Measurement Group©, Raleigh, NC, USA) is held against the SG. Making sure that when the glue is drying the SG follows the curve of the C-shaped brass frame tightly without air bubbles in between the C-frame and the SG foil (Figure A.3). The thin metal thread is moved gently from side to side while the glue is drying to minimize the chance of it getting glued onto the surface if excessive

glue has been applied to the SG foil. The SG's are glued as close as possible to the middle of the C-frame. This is the location where the largest deformation of the C-frame will occur, when longitudinal forces are applied to the C-transducer. Furthermore, the SG's should not be to close to the two innermost holes in the C-frame, which will be evident later.

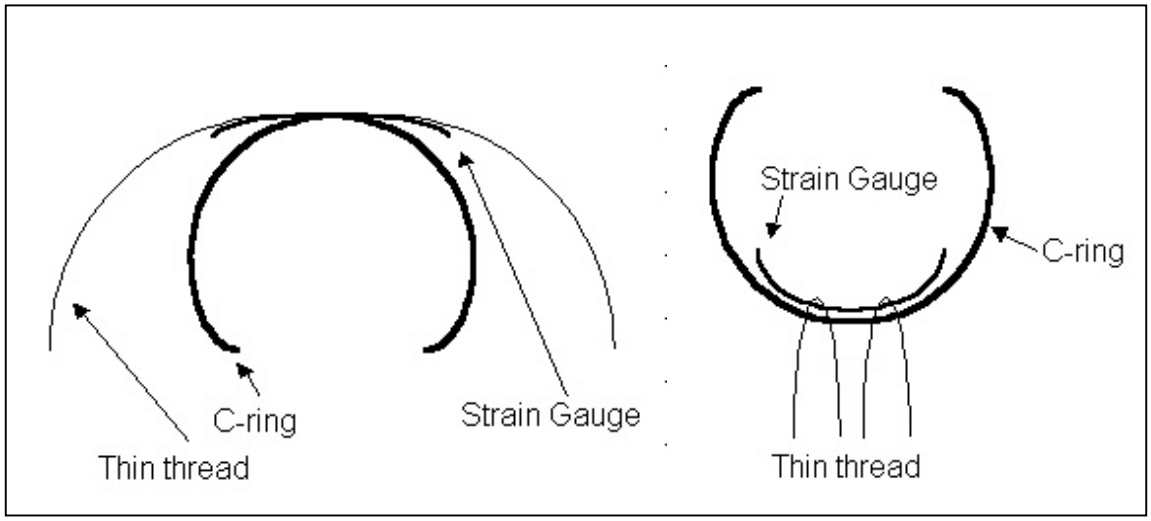

Figure A.3. Left: How the SG is held tightly to the convex surface of the SG while the super glue is drying. Right: How the SG is held to the concave surface while the super glue is curing. The threads are moved from the middle of the SG towards the ends to push out any air bubbles from underneath the SG.

After the superglue has dried, the SG's are interconnected by soldering one end of a thin conducting wire (134-AWP Single Conductor, Measurement Group©, Raleigh, NC, USA) to the leftmost terminal on the outer SG and the other end to the leftmost terminal on the inner SG when using left/right convention as in Figure A.4. In Figure A.4 the location of the interconnection is where the black conductor is soldered to the outer SG

terminal. The thin conducting wire goes around the edge of the C-frame. This interconnection is necessary to complete the Wheatstone half-bridge.

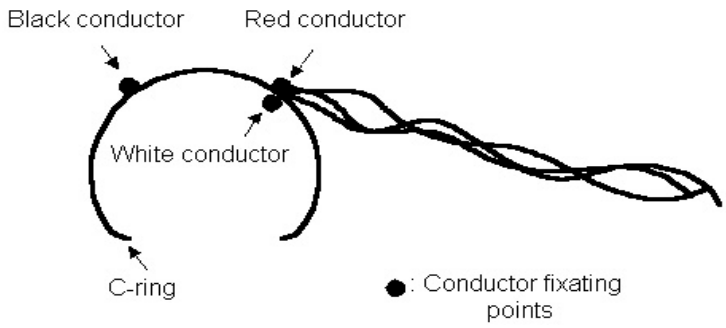

Figure A.4. Attachment sites for the three conductors on the C-frame.

One end of approximately 2 meters of the 336-FTE wire with 3 conducting cables (Measurement Group©, Raleigh, NC, USA) is attached to three of the four SG's solder terminals. The wire is oriented in the C-frame's longitudinal direction. The conducting cable has 3 conductors color coded black, red and white. The insulation around the 3 conductors is made of Teflon. The length of the 3 conductors is adjusted to match the solder terminals on the SG's as shown in Figure A.4. The black conductor follows the edge and the arch in the middle of the C-frame. The Teflon insulation makes the wire stronger mechanically and chemically compared to wires with other insulation materials. This makes it possible to use the very thin and delicate 36 gauge 336-FTE wire. In applications where the C-transducers are sutured to chordae tendineae (CT); thin, light, and flexible wires are used, so the motion of the wires caused by saline flow in the left heart simulator does not affect the CT significantly. Approximately 1.5mm of the Teflon insulation is stripped by holding the end of the conductors into a flame thereby melting

the Teflon so it retracts from the end of the metal conductor. The conductors are swiftly soldered to their corresponding solder terminals on the SG. Melting the solder more than a couple of seconds increases the risk of melting the SG foil or destroying the bonding between the SG and the C-frame.

The solder job is tested with an ohmmeter. The soldering will inevitably change the resistance in the SG. If the resistance remains in the range 350±5Ω it is considered good enough to provide a stable Wheatstone bridge.

The solder terminals are very fragile. Tying the 3-conductor cable down to the C-frame reduces stress on individual solder terminals. Therefore, the wire consisting of all three conductors are braced to the C-frame with a 2-0 suture (TI-CRON, coated braided polyester suture, USS DG Sutures) to the right of where the red and white conductors are soldered to the SG terminals in Figure A.4. The suture is placed between the SG and the nearest hole in the C-frame.

The electrical circuit requires a highly resistant coating that seals properly and prevents leakage currents as well as mechanical protection.

The area between the two innermost holes on the C-frame is bonded with the same bonding material as mentioned above, M-Bond 43 B. Furthermore, about 2cm of the three conductors are bonded also providing stability around the bracing site with the suture. Again, the bonding is cured as described above. The bonding is repeated three times. The areas around the SG's, solder terminals, and bracing site are now stiffened and sealed. To maintain a good seal and to protect the sensitive areas, another coating is applied. M-Coat B Nitrile Rubber Coating (Measurement Group©, Raleigh, NC, USA) is applied on top of where the bonding material was applied. The nitrile rubber is applied

cold (refrigerator temperature) since this reduces the viscosity. If it is too viscous, it will not cover the conductors, solder terminals, SG's, or the surrounding area properly. Figure A.5 shows a finished C-transducer with wires soldered to the SG's and with the nitrile rubber coating.

Figure A.5. A C-transducer shown next to a ruler with cm units

The coating is applied once, and cured at room temperature for about two hours. Then a second layer is applied followed by 24 hours of cure at room temperature. To further improve chemical resistance, the C-transducer is cured in an oven for one hour at 95 °C.

A connector that matches the signal conditioner is soldered onto the other end of the Teflon wire.

Attachment of Force transducer to the Chordae Tendineae

The CT is attached to the C-transducers by placing the CT in both slits and then suturing it to each end of the C by pulling suture through the holes, through the CT, and tying the

suture around the CT finishing with three or four knots. When it is attached at both ends, the CT is cut in between allowing CT force to be measured by the C-transducer (Figure A.6).

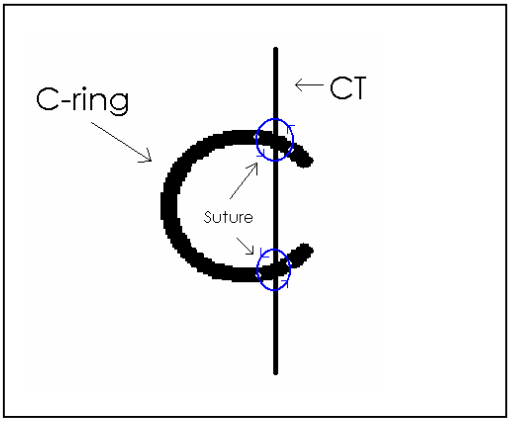

Figure A.6. Diagram of chordal attachment method to the transducer.

Sensitivity

After the C-transducer has been constructed, its sensitivity is measured. The sensitivity is calculated by reading the output voltages from the signal conditioner at known loads.

For the sensitivity calibrations the C-transducer is suspended by a thin wire. The transducer is freely hung 30cm above a given surface by pulling a wire through the two leftmost holes (left/right convention as in Figure A.4). Another piece of the wire is pulled through the right two holes according to the left/right convention in Figure A.4. Several weights up to a maximum load of approximately 500g are hung in the latter wire. The corresponding SG output voltage is measured. The voltage-load linear relationship yields a slope coefficient typically around 0.6 Volts per Newton.

Linearity

We have measured sensitivities with weights up to 542g. The maximum force measured in any CT has been close to 3 N. The C-transducers all have a good linear output voltage relationship with loads below the aforementioned 542g. No hysteresis was observed in the force range 0-6 N.

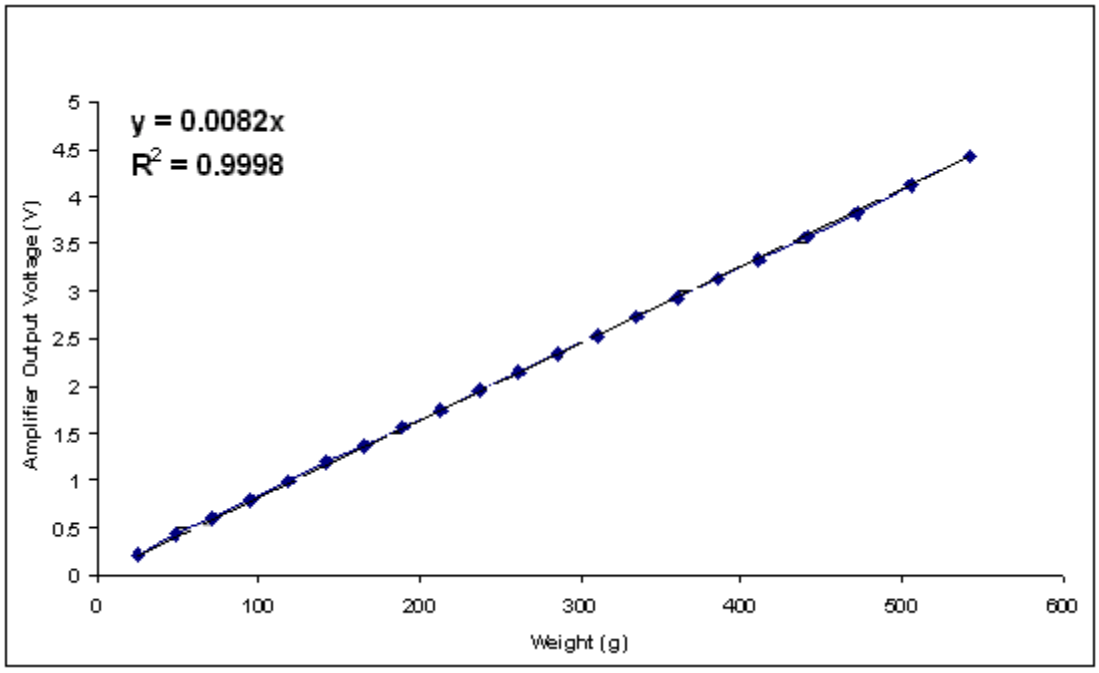

Figure A.7 C-ring transducer linearity graph with a trend line superimposed on the averaged data points.

The accuracy differs between the C-transducers and depends greatly on variations in sensitivity caused by uneven construction. The best way of describing their accuracies is by looking at their linearity.

Twenty-one weights, each weighing between 23g and 36g were used to find the linearity. One by one the weights were added and the output voltages were measured from the signal conditioner in between.

The accumulated weight was 542g. Linearity was measured three times. The output voltages measured in each of the three measurements were averaged and the standard deviations were calculated. The highest standard deviation was 0.025V. A trend line was found and the data point furthest away from the trend line was 1.9% from the linear equation of this line. The trend was linear giving $R^2 = 0.9998$ (Figure A.7)

The sensitivity range of all C-transducers varies with time. As the C-transducers age, they also tend to become more sensitive. We believe this is due to changes in mechanical resistance and strength of the bonding and coating materials on the C-transducers. The sensitivity typically starts in new C-transducers to be close to 0.5 V/N and for the older C-transducer specimens the sensitivity is closer to 0.7 V/N. The changes in the sensitivities do not happen fast. The change from ~0.5 V/N to ~0.7 V/N is a long process that comes from months of use, if used approximately once per week.

Noise

The forces measured by the C-transducer are averaged over ten heart cycles almost eliminating noise completely. However, with the in-house built signal conditioner that has a low pass filter of order 6 cutting off at 10 kHz and another 2^{nd} order low pass filter at 500 Hz has a noise level close to that which is below the critical quantization level of the 12 bit analog-to-digital converter (ADC). The quantization level is one half of the least significant bit (½LSB), so in this application with the SG input module voltage output of ±5V it corresponds to 1.22 mV. The highest noise measured with a TrueRMS multimeter (Hewlett Packard 34401A) was 2.1 mV.

Some drift of the C-transducers has been observed. The baseline shifts gradually over hours, in saline solution as well as in free air. The maximum baseline shift that has been observed was not more than 10 mV over a time of 3 hours. Before the C-transducers are used in an experiment, their offset is adjusted with the aforementioned potentiometers.
The drift is so slow that it has no impact on experimental results, as cardiac cycles are typically 860ms.

Frequency Response

The frequency response was tested using a random noise test in a model at the Engineering College of Aarhus [134]. The frequency response curve was flat from 0 to 80-120 Hz, which is sufficient for measuring the CT forces. 30 Hz is considered the upper limit of interest for intra cardiac measurements [135].

Lifespan

The C-transducers are quite small and delicate in nature. Their average life is about 90 days under weekly use. We believe that this is due to the cyclic stress on the delicate connections where the conducting wires are soldered onto the SG soldering terminals, which have a small area. This causes open circuits in the Wheatstone bridge, leading to C-transducer malfunction.

Sensitivity to Temperature

An experimental setup was designed to test the sensitivity of the C-ring transducers to fluctuations in temperature (Figure A.8). The setup consisted of a computer-controlled

linear actuator, which was used to apply axial forces onto the transducers, and a testing chamber which was filled with water at different temperatures. The free end of the linear actuator was located inside the testing chamber. The c-transducers were suspended using suture at both, their ends. One end was fixed onto a rod on the testing chamber and the other to a rod on the linear actuator. A thermometer submerged in the water in the testing chamber was used to measure temperatures adjacent to the transducers.

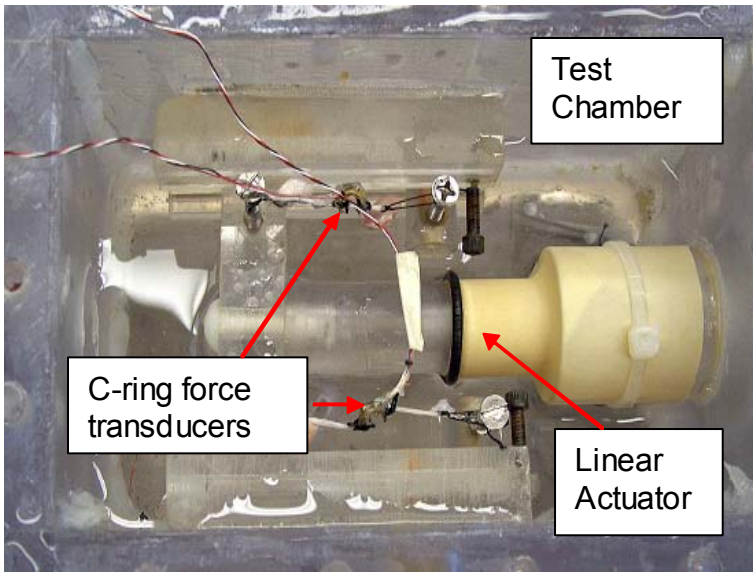

Figure A.8. Experimental setup for temperature sensitivity experiments.

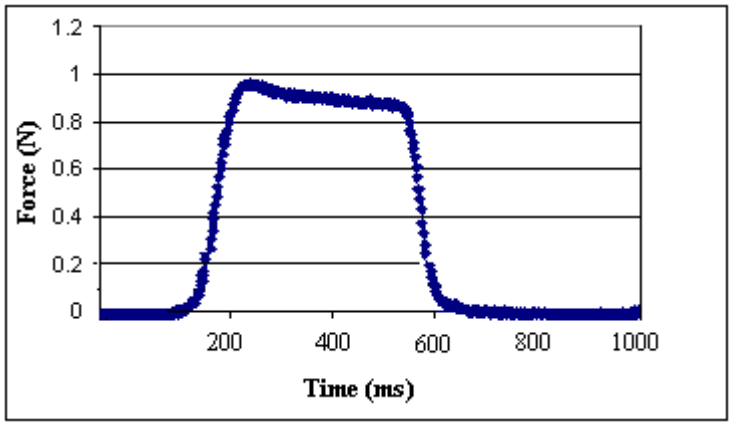

Figure A.9. Loading waveform for temperature sensitivity experiments.

The transducers were cyclically loaded at 1.1Hz up to a maximum load of 1N (maximum load held constant for 300ms). The load waveform simulates conditions found in chordal force measurements (Figure A.9). The displacement of the linear actuator was adjusted so the maximum load on the transducers was 1N. No further adjustment to the linear actuator's displacement was performed. Under these displacement conditions force measurements from the c-ring transducers were acquired for 5 cycles and averaged offline. Force readings (5 cycles) at different temperatures were then recorded while maintaining the same linear actuator displacement. The experiments were repeated at temperatures of 25°C, 31°C, and 37°C.

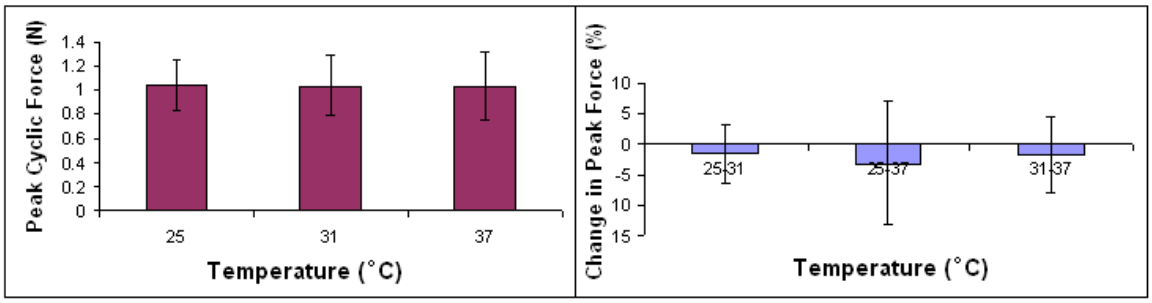

Figure A.10. (A) Average peak cyclic forces at the different temperature conditions. (B) Percentage variations in force due to temperature.

Twelve experiments were conducted using the aforementioned protocol. Cyclic forces were calculated by subtracting the maximum force in each cycle from the transducer reference baseline for the same cycle. The results for cyclic forces were averaged and compared using paired t-tests. There was a significant baseline shift for the transducers at different temperatures. However, as shown by the results in Figure A.10, there was no significant difference in cyclic force associated with changes in temperature. In chordal force experiments diastolic force was considered as baseline reference, therefore, shifts in

baseline readings associated with changes in temperature should not influence the results of the current study. The insensitivity of cyclic forces to changes in temperature (range 25°C to 37°C) validated peak systolic force measurements within this range of temperatures.

The C-transducers have been used in applications where the environment has limited space and is chemically hostile [136]. However, the technology behind the C-shaped transducers can be used in many different applications. The C-transducers are very good at measuring longitudinal forces because of their attractive properties like low noise, good linearity, and ability to work in harsh environments. The weakest part of the C-transducers is probably the connection between the wires and the soldering terminals. If the C-transducers are used in another application where they are allowed to be bigger, the problem with this weak connection would be circumvented.

APPENDIX B

DATA

This section contains data on chordal areas, peak systolic forces, peak systolic stresses, regurgitation volumes, leaflet strains, effective orifice areas, and Alfieri stitch forces for all the experiments arranged according to specific aim.

TABLE OF CONTENTS **Page**

Specific Aim 1- The Normal Mitral Valve

Table B.1. Peak systolic force (PSF) for individual chords in the saddle annulus configuration and normal papillary muscle position. Data in grey was discarded because it was below the 0.01N threshold.

Valve Number	Experiment Date	Peak transmitral pressure (mmHg)	Anterior Strut PST (N)	Post. Intermediate PST (N)	Post. Marginal PST (N)	Basal Posterior PST (N)	Anterior marginal PST (N)	Commissural PST (N)
1	18-Jun	124.2	1.384	0.449		0.075	0.516	0.008
2	21-Jun	120.4	0.879	0.332	0.019	0.315	0.450	0.005
3	28-Jun	119.6	1.310	0.003	0.015	0.738	0.392	0.010
4	9-Aug	120.7	0.436	0.443	0.007	0.040	0.306	0.042
5	29-Aug	120.8	0.919	0.011	0.101	0.404	0.386	0.053
6	30-Oct	120.8	0.752	0.273	0.088	0.298	0.068	0.463

Table B.2. Peak systolic stress (PSS) for individual chords in the saddle annulus configuration and normal papillary muscle position. Data in grey was discarded because PSF was below the 0.01N threshold.

Valve	Date	Anterior Strut PSS (MPa)	Post. Intermediate PSS (MPa)	Post. Marginal PSS (MPa)	Basal Posterior PSS (MPa)	Anterior marginal PSS (MPa)	Commissural PSS (MPa)
1	18-Jun	0.68	0.55		0.06	1.38	
2	21-Jun	0.43	0.41	0.06	0.26	1.20	0.01
3	28-Jun	0.65		0.05	0.62	1.05	0.01
4	9-Aug	0.22	0.54		0.03	0.82	0.05
5	29-Aug	0.45	0.01	0.30	0.34	1.03	0.07
6	30-Oct	0.37	0.33	0.26	0.25	0.18	0.58

Table B.3. Major principal stretch, minor principal stretch and areal stretch values for the mitral valve in the normal papillary muscle position and normal annulus configuration (SR=20%).

Valve	Date	Major Principal Stretch	Minor Principal Stretch	Areal Stretch
1	27-Jan	1.235	1.060	1.337
2	28-Jan	1.316	1.173	1.581
3	8-Feb	1.263	1.142	1.490
4	11-Feb	1.184	1.094	1.547
5	17-Mar	1.076	1.038	1.219
6	29-Mar	1.301	1.105	1.511
7	31-Mar	1.184	1.103	1.382
8	6-Apr	1.245	1.164	1.475

Table B.4. Chordal area measurements in the leaflet insertion region.

Valve	Anterior strut Area (mm^2)	Anterior marginal Area (mm^2)	Posterior marginal Area (mm^2)	Posterior intermediate Area (mm^2)	Basal posterior Area (mm^2)	Commissural Area (mm^2)
1	1.60	0.54	0.43	0.90	0.29	0.89
2	3.17	0.23	0.30	0.63	1.46	0.36
3	2.20	0.36	0.18	1.13	1.34	0.37
4	2.19	0.39	0.14	1.04	2.44	0.50
5	2.26	0.50	0.36	0.28	2.76	1.14
6	2.06	0.93	0.47	0.56	0.53	1.43
7	1.50	0.09	0.38	0.33	0.48	0.46
8	2.80	0.28	0.34	0.75	0.43	0.34
9	1.89	0.51	0.19	1.22	3.73	0.52
10	1.69	0.48	0.19	0.63	1.16	0.56
11	2.07	0.13	0.35	1.14	1.58	0.53
12	1.39	0.34	0.19	0.58	1.49	0.93

Table B.5. Chordal area measurements in the central section of the chord.

Valve	Anterior strut Area (mm^2)	Anterior marginal Area (mm^2)	Posterior marginal Area (mm^2)	Posterior intermediate Area (mm^2)	Basal posterior Area (mm^2)	Commissural Area (mm^2)
1	1.41	1.48	0.21	0.42	0.68	0.51
2	1.88	0.25	0.73	0.53	2.34	0.79
3	1.41	0.24	0.14	0.57	1.33	0.60
4	0.95	0.35	0.18	1.04	1.18	0.67
5	2.91	0.35	0.28	0.29	1.75	0.73
6	2.14	0.63	0.17	1.03	0.65	0.92
7	1.37	0.09	0.10	0.36	0.85	0.47
8	2.00	0.15	0.24	0.31	0.61	0.56
9	1.34	0.17	0.29	1.12	2.68	0.59
10	1.35	0.30	0.34	0.78	0.74	0.89
11	2.67	0.25	0.76	0.58	0.51	0.83
12	0.99	0.38	0.16	1.57	1.12	1.00

Table B.6. Chordal area measurements in the papillary muscle insertion region.

Valve	Anterior strut Area (mm^2)	Anterior marginal Area (mm^2)	Posterior marginal Area (mm^2)	Posterior intermediate Area (mm^2)	Basal posterior Area (mm^2)	Commissural Area (mm^2)
1	2.49	0.73	1.03	0.57	0.62	1.80
2	2.01	0.23	0.50	0.98	1.32	0.70
3	2.64	0.25	0.32	0.66	0.90	0.49
4	1.89	0.23	0.07	0.86	0.98	1.22
5	2.71	0.54	0.51	0.94	1.39	1.00
6	2.89	0.58	0.68	1.13	0.41	1.72
7	1.14	0.17	0.33	0.55	0.37	0.50
8	2.35	0.10	0.32	0.75	0.53	0.87
9	2.16	0.26	0.19	1.21	2.81	0.19
10	2.05	0.27	0.43	0.79	0.92	0.52
11	2.66	0.43	0.46	1.55	0.42	1.44
12	2.75	0.25	0.19	1.57	0.21	1.46

Specific Aim 2 - The Pathological Mitral Valve

Table B.7. Average peak systolic forces (PSF) for the individual chords in the eight different papillary muscle positions and flat annulus configuration (SR=0%)

Papillary muscle position	Anterior strut PSF(N)	Posterior intermediate PSF(N)	Posterior marginal PSF(N)	Basal Posterior PSF(N)	Anterior Marginal PSF(N)	Commissural PSF(N)
000	1.12 ± 0.54	0.34 ± 0.29	0.26 ± 0.24	0.21 ± 0.18	0.36 ± 0.22	0.15 ± 0.21
005	0.59 ± 0.49	0.09 ± 0.08	0.19 ± 0.25	0.08 ± 0.04	0.25 ± 0.09	0.04 ± 0.04
050	1.10 ± 0.69	0.21 ± 0.15	0.21 ± 0.24	0.10 ± 0.06	0.25 ± 0.10	0.05 ± 0.04
055	1.06 ± 0.74	0.20 ± 0.13	0.24 ± 0.24	0.06 ± 0.05	0.28 ± 0.11	0.06 ± 0.04
500	1.42 ± 0.78	0.30 ± 0.22	0.27 ± 0.34	0.29 ± 0.19	0.28 ± 0.13	0.15 ± 0.10
505	0.93 ± 0.87	0.18 ± 0.15	0.19 ± 0.27	0.21 ± 0.07	0.18 ± 0.07	0.26 ± 0.24
550	1.50 ± 0.73	0.53 ± 0.51	0.29 ± 0.36	0.38 ± 0.29	0.22 ± 0.13	0.15 ± 0.10
555	1.52 ± 0.94	0.37 ± 0.36	0.27 ± 0.34	0.24 ± 0.20	0.27 ± 0.19	0.25 ± 0.22

Table B.8. Peak systolic forces (PSF) for individual chords in the normal papillary muscle position and flat annulus configuration (SR=0%).

Valve Number	Experiment Date	Valve Type	Anterior strut PSF(N)	Post. Intermediate PSF(N)	Post. Marginal PSF(N)	Basal Posterior PSF(N)	Ant. Marginal PSF(N)	Commussural PSF(N)
1	6-Jun	porcine	1.43	0.27	0.50	0.06	0.39	0.07
2	18-Jun	human	1.82	0.27	0.40	0.03	0.63	0.12
3	21-Jun	human	0.85	0.28	0.01	0.22	0.41	0.05
4	9-Aug	human	0.41	0.29	0.51	0.08	0.22	0.14
5	6-Sep	human	0.59	0.52	0.61	0.36	0.78	
6	24-May	porcine	1.32	0.97		0.61	0.13	0.09
7	14-Jun	porcine			0.07	0.06	0.43	0.03
8	28-Jun	human	1.46		0.01	0.25	0.45	0.03
9	7-Aug	porcine	0.32	0.05		0.10	0.09	0.04
10	29-Aug	human	1.65	0.01	0.08	0.19	0.22	0.15
11	30-Oct	human	1.37	0.44	0.13	0.41	0.17	0.74

Table B.9. Peak systolic forces (PSF) for individual chords for papillary muscle position 005 and the flat annulus configuration (SR=0%).

Valve Number	Experiment Date	Valve Type	Anterior strut PSF(N)	Post. Intermediate PSF(N)	Post. Marginal PSF(N)	Basal Posterior PSF(N)	Ant. Marginal PSF(N)	Commussural PSF(N)
3	21-Jun	human	0.32	0.14	0.01	0.14	0.32	0.01
4	9-Aug	human	0.33	0.18	0.48	0.06	0.25	0.04
9	7-Aug	porcine	0.37	0.04		0.06	0.13	0.02
10	29-Aug	human	1.33	0.01	0.08	0.07	0.32	0.09

Table B.10. Peak systolic forces (PSF) for individual chords for papillary muscle position 050 and the flat annulus configuration (SR=0%).

Valve Number	Experiment Date	Valve Type	Anterior strut PSF(N)	Post. Intermediate PSF(N)	Post. Marginal PSF(N)	Basal Posterior PSF(N)	Ant. Marginal PSF(N)	Commussural PSF(N)
1	6-Jun	porcine	1.54	0.25	0.50	0.05	0.29	0.06
2	18-Jun	human	1.79	0.23	0.29	0.02	0.46	0.10
3	21-Jun	human	0.42	0.27	0.02	0.18	0.22	0.02
4	9-Aug	human	0.37	0.44	0.58	0.07	0.23	0.08
7	14-Jun	porcine			0.04	0.04	0.29	0.01
8	28-Jun	human	1.29		0.01	0.15	0.23	0.02
9	7-Aug	porcine	0.41	0.07		0.11	0.12	0.03
10	29-Aug	human	1.90	0.03	0.05	0.15	0.18	0.11

Table B.11. Peak systolic forces (PSF) for individual chords for papillary muscle position 055 and the flat annulus configuration (SR=0%).

Valve Number	Experiment Date	Valve Type	Anterior strut PSF(N)	Post. Intermediate PSF(N)	Post. Marginal PSF(N)	Basal Posterior PSF(N)	Ant. Marginal PSF(N)	Commussural PSF(N)
1	6-Jun	porcine	1.60	0.29	0.55	0.04	0.33	0.08
2	18-Jun	human	1.83	0.25	0.34	0.00	0.48	0.13
3	21-Jun	human	0.40	0.22	0.01	0.15	0.27	0.02
4	9-Aug	human	0.37	0.35	0.47	0.05	0.23	0.07
7	14-Jun	porcine			0.05	0.04	0.32	0.01
9	7-Aug	porcine	0.40	0.06		0.07	0.14	0.03
10	29-Aug	human	1.75	0.02	0.05	0.09	0.18	0.10

Table B.12. Peak systolic forces (PSF) for individual chords for papillary muscle position 500 and the flat annulus configuration (SR=0%).

Valve Number	Experiment Date	Valve Type	Anterior strut PSF(N)	Post. Intermediate PSF(N)	Post. Marginal PSF(N)	Basal Posterior PSF(N)	Ant. Marginal PSF(N)	Commussural PSF(N)
1	6-Jun	porcine	2.03	0.47	0.71	0.13	0.37	0.10
3	21-Jun	human	1.48	0.35	0.01	0.36	0.35	0.15
4	9-Aug	human	0.63	0.53	0.69	0.19	0.24	0.30
7	14-Jun	porcine			0.15	0.08	0.48	0.07
8	28-Jun	human	1.61		0.02	0.61	0.30	0.07
9	7-Aug	porcine	0.39	0.12		0.20	0.09	0.09
10	29-Aug	human	2.37	0.02	0.06	0.44	0.16	0.30

Table B.13. Peak systolic forces (PSF) for individual chords for papillary muscle position 505 and the flat annulus configuration (SR=0%).

Valve Number	Experiment Date	Valve Type	Anterior strut PSF(N)	Post. Intermediate PSF(N)	Post. Marginal PSF(N)	Basal Posterior PSF(N)	Ant. Marginal PSF(N)	Commussural PSF(N)
3	21-Jun	human	0.63	0.22	0.04	0.22	0.24	0.09
4	9-Aug	human	0.51	0.37	0.51	0.13	0.16	0.59
9	7-Aug	porcine	0.36	0.11		0.17	0.08	0.09
10	29-Aug	human	2.24	0.04	0.03	0.30	0.23	0.27

Table B.14. Peak systolic forces (PSF) for individual chords for papillary muscle position 550 and the flat annulus configuration (SR=0%).

Valve Number	Experiment Date	Valve Type	Anterior strut PSF(N)	Post. Intermediate PSF(N)	Post. Marginal PSF(N)	Basal Posterior PSF(N)	Ant. Marginal PSF(N)	Commussural PSF(N)
1	6-Jun	porcine	2.04	0.45	0.73	0.14	0.26	0.08
3	21-Jun	human	1.60	0.38	0.00	0.41	0.35	0.15
4	9-Aug	human	0.64	0.75	0.76	0.18	0.26	0.29
6	24-May	porcine	1.68	1.43		0.96	0.03	0.20
7	14-Jun	porcine			0.12	0.07	0.41	0.07
8	28-Jun	human	1.72		0.03	0.56	0.22	0.05
9	7-Aug	porcine	0.40	0.14		0.24	0.09	0.09
10	29-Aug	human	2.42	0.03	0.08	0.48	0.12	0.29

Table B.15. Peak systolic forces (PSF) for individual chords for papillary muscle position 555 and the flat annulus configuration (SR=0%).

Valve Number	Experiment Date	Valve Type	Anterior strut PSF(N)	Post. Intermediate PSF(N)	Post. Marginal PSF(N)	Basal Posterior PSF(N)	Ant. Marginal PSF(N)	Commussural PSF(N)
1	6-Jun	porcine	2.21	0.40	0.72	0.05	0.33	0.10
3	21-Jun	human	0.72	0.23	0.02	0.24	0.24	0.11
4	9-Aug	human	0.61	0.48	0.69	0.15	0.22	0.56
6	24-May	porcine	1.73	1.12		0.69	0.07	0.24
7	14-Jun	porcine			0.13	0.10	0.39	0.06
9	7-Aug	porcine	0.37	0.12		0.16	0.11	0.08
10	29-Aug	human	2.39	0.04	0.06	0.31	0.14	0.24
11	30-Oct	human	2.62	0.19	0.00	0.19	0.65	0.63

Specific Aim 3 – The Repaired Mitral Valve

Table B.16. Mitral regurgitation volumes for the Alfieri experiments.

Valve	Date	Dilated Annulus regurgitation volume (ml)	Normal Annulus regurgitation volume (ml)	Contracted Annulus regurgitation volume (ml)
1	7-Apr	-24.9	-18.1	-16.3
2	8-Apr	-30.0	-22.9	-22.0
3	17-Jun	-31.6	-29.6	-26.5
4	22-Jun	-27.0	-24.3	-18.9
5	29-Jun	-28.3	-25.0	-25.7
6	2-Jul	-29.1	-24.7	-25.5
7	8-Jul	-40.3	-36.4	-33.4
8	8-Jul	-29.3	-24.3	
9	16-Jul	-40.9	-30.0	-32.5

Table B.17. Effective orifice areas (EOA) for the steady flow experiments. Valves without Alfieri stitch and in the contracted annulus configuration.

Valve	Flow rate 0 L/min EOA (cm^2)	Flow rate 5 L/min EOA (cm^2)	Flow rate 10 L/min EOA (cm^2)	Flow rate 15 L/min EOA (cm^2)	Flow rate 20 L/min EOA (cm^2)	Flow rate 25 L/min EOA (cm^2)	Flow rate 30 L/min EOA (cm^2)
1	0.00	4.17	3.75	4.10	4.19		4.43
2	0.00	3.40	3.42	3.32	3.85	4.10	4.02
3	0.00	4.17	3.75	3.90	4.01	4.22	4.02
4	0.00	3.40	3.29	3.57	3.31	3.80	3.60
5	0.00	2.95	3.29	3.65	4.07	4.18	4.15
6	0.00	2.64	3.42	3.72	3.81	4.10	4.13

Table B.18. Effective orifice areas (EOA) for the steady flow experiments. Valves without Alfieri stitch and in the normal annulus configuration.

Valve	Flow rate 0 L/min EOA (cm^2)	Flow rate 5 L/min EOA (cm^2)	Flow rate 10 L/min EOA (cm^2)	Flow rate 15 L/min EOA (cm^2)	Flow rate 20 L/min EOA (cm^2)	Flow rate 25 L/min EOA (cm^2)	Flow rate 30 L/min EOA (cm^2)
1	0.00	5.96	5.37	5.94	5.34		5.54
2	0.00	2.67	3.80	4.46	4.78	4.93	5.14
3	0.00	5.96	4.24	4.60	4.78	4.59	4.90
4	0.00	5.96	4.24	4.60	4.68	5.19	5.04
5	0.00	2.98	3.80	4.32	5.09	5.42	5.36
6	0.00	5.96	4.54	5.15	4.98	5.42	5.42

Table B.19. Effective orifice areas (EOA) for the steady flow experiments. Valves without Alfieri stitch and in the dilated annulus configuration.

Valve	Flow rate 0 L/min EOA (cm^2)	Flow rate 5 L/min EOA (cm^2)	Flow rate 10 L/min EOA (cm^2)	Flow rate 15 L/min EOA (cm^2)	Flow rate 20 L/min EOA (cm^2)	Flow rate 25 L/min EOA (cm^2)	Flow rate 30 L/min EOA (cm^2)
1	0.00		5.97	6.76	6.46		6.96
2	0.00	4.18	5.34	5.39	5.54	6.06	6.11
3	0.00	5.92	4.88	5.39	6.04	5.83	6.03
4	0.00		5.34	5.39	5.54	5.83	6.11
5	0.00	4.18	4.88	5.16	5.86	6.46	5.45
6	0.00	4.18	5.34	5.96	6.04	7.14	7.23

Table B.20. Effective orifice areas (EOA) for the steady flow experiments. Valves with Alfieri stitch and in the contracted annulus configuration.

Flow rate (L/min)	Valve 1 EOA (cm^2)	Valve 2 EOA (cm^2)	Valve 3 EOA (cm^2)	Valve 4 EOA (cm^2)	Valve 5 EOA (cm^2)	Valve 6 EOA (cm^2)
0	0.00	0.00	0.00	0.00	0.00	0.00
2			1.23	2.46	1.42	1.74
4	2.75	2.75	1.68	2.75	2.13	2.13
6	2.92	2.92	2.06	2.53	2.38	2.53
8	3.02	3.18	2.31	2.75	2.65	2.88
10	3.43	3.18	2.48	2.97	2.73	3.18
12	3.57	3.28	2.70	3.12	3.12	3.37
14	3.75	3.42	2.80	3.17	3.23	3.50
16	3.67	3.54	2.88	3.22	3.37	3.48
18	3.79	3.62	3.00	3.39	3.39	3.57
20	4.01	3.80	3.03	3.40	3.51	3.63
25		3.71	3.43	3.52	3.71	3.86
30		3.72	3.31	3.78	3.72	3.82

Table B.21. Effective orifice areas (EOA) for the steady flow experiments. Valves with Alfieri stitch and in the normal annulus configuration.

Flow rate (L/min)	Valve 1 EOA (cm^2)	Valve 2 EOA (cm^2)	Valve 3 EOA (cm^2)	Valve 4 EOA (cm^2)	Valve 5 EOA (cm^2)	Valve 6 EOA (cm^2)	Valve 7 EOA (cm^2)	Valve 8 EOA (cm^2)
0	0.00	0.00	0.00	0.00	0.00	0.00	0.00	0.00
2	1.22	2.44			1.73		1.73	2.44
4	2.38	2.75	3.37	2.75	1.95	4.77	2.13	2.38
6	2.75	4.21	3.64	2.97	2.30	3.26	2.43	2.97
8	3.04	3.63	3.93	3.40	2.67	3.21	2.78	3.21
10	3.78	3.98	4.52	3.78	2.90	3.45	3.09	3.60
12	4.13	4.31	4.31	3.82	2.98	3.58	3.47	3.69
14	4.32	4.47	4.47	4.19	3.16	3.74	3.49	3.84
16	4.63	4.50	4.63	4.50	3.32	3.81	3.74	4.07
18	4.82	4.71	4.82	4.40	3.50	3.81	3.81	4.15
20	5.09	5.09	4.97	4.15	3.56	3.98	4.03	4.22
25	5.40	5.40		4.46	3.64	4.06	4.51	4.22
30	5.05	5.32		4.82	3.77	4.27	4.43	4.82

Table B.22. Effective orifice areas (EOA) for the steady flow experiments. Valves with Alfieri stitch and in the dilated annulus configuration.

Flow rate (L/min)	Valve 1 EOA (cm^2)	Valve 2 EOA (cm^2)	Valve 3 EOA (cm^2)	Valve 4 EOA (cm^2)	Valve 5 EOA (cm^2)	Valve 6 EOA (cm^2)
0	0.00	0.00	0.00	0.00	0.00	0.00
2					2.39	2.39
4	3.40	4.81	3.40	4.81	2.78	2.41
6	3.60	4.15	3.22	4.15	2.94	2.94
8	3.92	3.92	3.63	3.92	3.20	3.63
10	4.22	4.22	3.78	3.98	3.19	3.78
12	4.79	4.54	4.15	4.15	3.59	4.15
14	5.06	4.84	4.20	4.49	3.75	4.49
16	5.29	5.29	4.38	4.63	4.07	4.50
18	5.37	5.37	4.58	4.58	4.29	4.80
20	5.62	5.33	4.77	4.35	4.50	4.86
25	5.57	5.76	5.31	4.95	5.16	5.23
30	5.46	5.94	5.18	5.18	5.46	5.79

Table B.23. Average diastolic effective orifice areas (EOA) for the pulsatile flow experiments. Valves with Alfieri stitch in the different annulus configurations.

Valve	Contracted Annulus EOA (cm^2)	Normal Annulus EOA (cm^2)	Dilated Annulus EOA (cm^2)
1	1.44	1.68	1.98
2	3.94	5.06	5.70
3	4.67	8.83	
4	5.48	7.56	11.19

Table B.24. Peak systolic Alfieri stitch force under physiological pulsatile flow (CO: 5L/min, Peak transmitral pressure: 120mmHg) in the different annulus configurations.

Valve	Experiment Date	Peak Systolic Force (N) Dilated Annulus	Peak Systolic Force (N) Normal Annulus	Peak Systolic Force (N) Contracted Annulus
1	7-Apr	0.065	0.025	0.017
2	8-Apr	0.087	0.020	0.013
3	17-Jun	0.059	0.056	0.048
4	22-Jun	0.070	0.072	0.056
5	29-Jun	0.092	0.079	0.039
6	2-Jul	0.067	0.048	0.047
7	8-Jul	0.123	0.071	0.032
8	8-Jul	0.123	0.065	
9	16-Jul	0.142	0.093	0.059

Table B.25. Peak diastolic Alfieri stitch force under physiological pulsatile flow (CO: 5L/min, Peak transmitral pressure: 120mmHg) for the different annulus configurations.

Valve	Experiment Date	Peak diastolic Force (N) Dilated Annulus	Peak diastolic Force (N) Normal Annulus	Peak diastolic Force (N) Contracted Annulus
1	7-Apr	0.042	0.040	0.039
2	8-Apr	0.066	0.071	0.070
3	17-Jun	0.053	0.067	0.065
4	22-Jun	0.063	0.083	0.090
5	29-Jun	0.073	0.070	0.058
6	2-Jul	0.050	0.059	0.063
7	8-Jul	0.125	0.117	0.099
8	8-Jul	0.080	0.067	
9	16-Jul	0.065	0.072	0.085

Table B.26. Peak systolic Alfieri stitch force for different peak transmitral pressures (100mmHg-140mmHg) at a cardiac output of 5L/min and normal annulus configuration.

Valve	Experiment Date	Peak Systolic Force (N) at 140mmHg	Peak Systolic Force (N) at 120mmHg	Peak Systolic Force (N) at 100mmHg
1	8-Apr	0.02	0.02	0.01
2	17-Jun	0.06	0.06	0.05
3	22-Jun	0.06	0.07	0.06
4	29-Jun	0.06	0.08	0.06
5	2-Jul	0.06	0.05	0.04
6	8-Jul	0.07	0.07	0.05
7	8-Jul	0.09	0.07	0.06
8	16-Jul	0.10	0.09	0.08

Table B.27. Peak diastolic Alfieri stitch force for different peak transmitral pressures (100mmHg-140mmHg) at a cardiac output of 5L/min and normal annulus configuration.

Valve	Experiment Date	Peak diastolic Force (N) at 140mmHg	Peak diastolic Force (N) at 120mmHg	Peak diastolic Force (N) at 100mmHg
1	8-Apr	0.075	0.071	0.056
2	17-Jun	0.074	0.067	0.059
3	22-Jun	0.100	0.083	0.070
4	29-Jun	0.071	0.070	0.062
5	2-Jul	0.060	0.059	0.048
6	8-Jul	0.081	0.067	0.060
7	8-Jul	0.140	0.117	0.092
8	16-Jul	0.080	0.072	0.060

Table B.28. Peak systolic Alfieri stitch force for different peak transmitral pressures (100mmHg-140mmHg) at a cardiac output of 5L/min and dilated annulus configuration.

Valve	Experiment Date	Peak Systolic Force (N) at 140mmHg	Peak Systolic Force (N) at 120mmHg	Peak Systolic Force (N) at 100mmHg
1	7-Apr	0.062	0.065	0.051
2	8-Apr	0.094	0.087	0.068
3	17-Jun	0.065	0.059	0.051
4	22-Jun	0.068	0.070	0.066
5	29-Jun	0.118	0.092	0.082
6	2-Jul	0.059	0.067	0.070
7	8-Jul	0.148	0.123	0.102
8	8-Jul	0.125	0.123	0.113
9	16-Jul	0.125	0.142	0.124

Table B.29. Peak diastolic Alfieri stitch force for different cardiac outputs (4L/min - 6L/min) at a peak transmitral pressure of 120mmHg and normal annulus configuration.

Valve	Experiment Date	Peak diastolic Force (N) at 6L/min	Peak diastolic Force (N) at 5L/min	Peak diastolic Force (N) at 4L/min
1	8-Apr	0.069	0.071	0.080
2	17-Jun	0.065	0.067	0.076
3	22-Jun	0.066	0.083	0.084
4	29-Jun	0.067	0.070	0.069
5	2-Jul	0.051	0.059	0.074
6	8-Jul	0.069	0.067	0.074
7	8-Jul	0.095	0.117	0.122
8	16-Jul	0.071	0.072	0.072

Table B.30. Peak major principal stretch in the central region of the anterior leaflet for the different saddle height to commissural diameter ratios (SR).

Valve	Date	Major Principal Stretch SR 0%	Major Principal Stretch SR 10%	Major Principal Stretch SR 20%	Major Principal Stretch SR 30%
1	27-Jan	1.345	1.277	1.235	1.172
2	28-Jan	1.425	1.368	1.316	1.318
3	8-Feb	1.368	1.289	1.263	1.250
4	11-Feb	1.337	1.206	1.184	1.120
5	17-Mar	1.129	1.123	1.076	1.158
6	29-Mar	1.354	1.344	1.301	1.137
7	31-Mar	1.263	1.253	1.184	1.196
8	6-Apr	1.252	1.244	1.245	1.247

Table B.31. Peak minor principal stretch in the central region of the anterior leaflet for the different saddle height to commissural diameter ratios (SR).

Valve	Date	Minor Principal Stretch SR 0%	Minor Principal Stretch SR 10%	Minor Principal Stretch SR 20%	Minor Principal Stretch SR 30%
1	27-Jan	1.047	1.035	1.060	1.073
2	28-Jan	1.129	1.104	1.173	1.176
3	8-Feb	1.187	1.087	1.142	1.084
4	11-Feb	1.115	1.096	1.094	0.931
5	17-Mar	1.059	1.048	1.038	1.062
6	29-Mar	1.058	1.072	1.105	1.063
7	31-Mar	1.094	1.097	1.103	1.116
8	6-Apr	1.115	1.146	1.164	1.135

Table B.32. Peak areal stretch in the central region of the anterior leaflet for the different saddle height to commissural diameter ratios (SR).

Valve	Date	Areal Stretch SR 0%	Areal Stretch SR 10%	Areal Stretch SR 20%	Areal Stretch SR 30%
1	27-Jan	1.408	1.321	1.309	1.257
2	28-Jan	1.609	1.511	1.544	1.550
3	8-Feb	1.624	1.402	1.442	1.355
4	11-Feb	1.502	1.329	1.302	1.042
5	17-Mar	1.198	1.180	1.119	1.232
6	29-Mar	1.433	1.441	1.437	1.208
7	31-Mar	1.383	1.376	1.307	1.335
8	6-Apr	1.396	1.426	1.449	1.415

APPENDIX C:

CD & HD CATALOG

The following appendix contains the file name protocol for CD1 and HD1. CD1 contains the raw data and the processed excel spread sheets for all the experiments. HD1 contains the high speed video files for the marker technique experiments.

CD1 Main Directory

The main directory is divided into the three specific aims.

Directory	Sub-Directory & Description					
Specific Aim 1	**DATA**	**Raw**	Contains the raw Daq-anal data for transmitral pressure, mitral flow and chordal force. Raw data of leaflet strain in the normal valve is in the raw data folder for specific aim 3			
		Processed	Contains excel spread sheets for transmitral pressure, mitral flow and chordal force during the entire cardiac cycle in the different annular configurations.			
	EXCEL SUMMARIES	Contain summary Excel Spread sheets for chordal force/stress, chordal area, and leaflet strain				
Specific Aim 2	**DATA**	**Raw**	Contains the raw Daq-anal data for transmitral pressure, mitral flow and chordal force			
		Processed	Contains excel spread sheets for transmitral pressure, mitral flow and chordal force during the entire cardiac cycle in the different papillary muscle positions.			
	EXCEL SUMMARIES	Contain summary data for peak chordal forces in the different papillary muscle positions for all valves				
Specific Aim 3	**ALFIERI**	**Steady**	**Force Data**	**Raw**	Contains the raw Daq-anal data of mitral flow and Alfieri stitch force.	
				Processed	Contains the processed Daq-anal data of mitral flow and Alfieri stitch force.	
			EXCEL SUMMARY OF EFFECTIVE ORIFICE AREA	Summary tables and data for effective orifice area under steady flow		
		Pulsatile	**DATA**	**Raw**	Contains the raw Daq-anal data for transmitral pressure, mitral flow and Alfieri stitch force	
				Processed	Contains excel spread sheets for transmitral pressure, mitral flow and Alfieri stitch force during the entire cardiac cycle in the different conditions.	
			EXCEL SUMMARIES	Contain summary data for Alfieri stitch force, peak Alfieri stitch force, and regurgitation volumes		

Specific Aim 3	**SADDLE EXPERIMENTS**	**DATA**	Contains output data from the marker technique codes including the output excel spread sheets. Additionally contains the raw data for mitral flow and transmitral pressure from Daq-anal.
		EXCEL SUMMARY	Contains the processed strain data and summary tables for all the studied valves in all the annular configurations.

Processed Sub-Directory

This sub-directory is subdivided into folders for each of the studied valves. Each sub-folder is divided into the different experimental conditions which were tested. (Annular configuration, papillary muscle positions, transmitral pressure, cardiac output, etc.) In each of these folders the files have the following name format:

1) *Specific Aim 1 & 2*

Chordal Force Data (VX_XXXXX_XXX_XXX_XX.xls)
File names have four parts separated by underscores "_".

No.1 "VX" denotes the valve identification number "V1".
No.2 "XXXXX" describes the date on which the experiment was conducted "MAY23".
No.3 "XXX" describes the annulus type used in the experiment: "FLT" flat, "SAD" Saddled, "CON" contracted, and "DLT" dilated.
No.4 "XXX" denotes the papillary muscle position used in the experiment.

2) *Specific Aim 3*

a) **Alfieri – Pulsatile** (ZZ_XXX_YYY_L.xls)
File names have four parts separated by underscores "_".

No.1 "ZZ" denotes date when the experiments was conducted.
No.2 "XXX" describes the annular configuration (dilated, normal, contracted).
No.3 "YYY" describes the transmitral pressure (100mmHg – 140mmHg)
No.4 "L" Describes the cardiac output for the experiment (4L/min-6L/min)

B) **Alfieri – Steady** (ZZ_XXX_YYY_L.xls)
File names have four parts separated by underscores "_".

No.1 "ZZ" denotes flow or force measurements.
No.2 "XXXX\" denotes the date of the experiment.
No.3 "YYY" describes the annular configuration (max-dilated, pos1-normal, pos2-contracted).
No.4 "L" Describes the cardiac output for the experiment (4L/min-6L/min)

C) **Saddle Experiments**: The folder for each valve is divided into four sub-folders which describe the annular configuration used for the test (0% Saddle, 10% Saddle, 20% Saddle, 30% Saddle). Within each folder the files are named according to the standard file names that the strain code assigns.

Raw Sub-Directory

This sub-directory is subdivided into folders for each of the studied valves. Each sub-folder is divided into the different experimental conditions which were tested. (Annular configuration, papillary muscle positions, transmitral pressure, cardiac output, etc.) In each of these folders the files follow a name format similar to that described above.

2) HD MAIN DIRECTORY

The hard drive contains the raw image files from the marker technique experiments.

Directory	Description
Images	This folder contains the "tiff" image files from the high speed cameras used in the marker technique experiments.

The main "image" folder is divided into eight sub-folders which correspond to different experiments. The folders are identified according to valve number and the date of the experiment (example: VALVE1_APR12). Each experimental folder is divided into four sections according to annular configuration (0% Saddle, 10% Saddle, 20% Saddle, 30% Saddle). Inside each of these folders for the different annular configurations the "tiff" images for camera A, camera B and the calibration cube are stored.

REFERENCES

1) Otto CM. Valvular heart disease. Saunders Company 2004; second edition, Chapter 13: 344 – 367.

2) Excerpt from NHLBI, Cardiomyopathy, statistics (http://www.nhlbi.nih.gov) Accessed: August 2006

3) Grigioni F, Enriquez-Sarano M, Zehr KJ, Bailey KR, Tajik AJ. Ischemic Mitral Regurgitation: long term outcome and prognostic implications with quantitative Doppler assessment. Circulation. 2001 Apr 3; 103(13):1759-64.

4) American Heart Association. Heart disease and stroke statistics Update 2006. (http://www.americanheart.org) Accessed: July 2006

5) Gillinov AM, Faber C, Houghtaling PL, Blackstone EH, Lam BK, Diaz R, Lytle BW, Sabik JF 3rd, Cosgrove DM 3rd.Repair versus replacement for degenerative mitral valve disease with coexisting ischemic heart disease. JTCVS 2003 Jun; 125(6):1197-9.

6) Savage EB, Ferguson B, DiSesa VJ. Use of Mitral Valve Repair: Analysis of Contemporary United States Experience Reported to The Society of Thoracic Surgeons National Cardiac Database. Ann Thorac Surg 2003, 75: 820-825.

7) Jimenez JH, Sorensen D, He Z, He S, Yoganathan AP. Effects of a saddle shaped annulus on mitral valve function and papillary muscle position. Annals of Biomedical Engineering 2003, v31: 1171-1181.

8) Salgo IS, Gorman JH III, Gorman RC, Jackson BM, Bowen FW, Plappert, T, Sutton MG, Edmunds LH. Effect of annular shape on leaflet curvature in reducing mitral leaflet stress. Circulation 2002; 106:711-717.

9) Timek TA, Miller DC. Experimental and clinical assessment of mitral annular area and dynamics: what are we actually measuring? Ann. Thorac Surg 2001; 72:966-974.

10) Madu EC, Baugh DS, Cruz IA, Johns C. Left ventricular papillary muscle morphology and function in left ventricular hypertrophy and left ventricular dysfunction. Med Sci Monit 2001; 7(6):1212-1218.

11) Toumanidis ST, Sideris, DA Papamichael CM, Moulopoulos SD. The role of mitral annulus motion in left ventricular function. Acta Cardiologica 1992;4:331-348.

12) Sacks MS, He ZM, Baijens L, Wanant S, Shah P, Sugimoto H. Yoganathan AP. Surface strains in the anterior leaflet of the functioning mitral valve. Annals of Biomedical Engineering 2002; v30: 1281-1290.

13) He ZM, Sacks MS, Baijens L, Wanant S, Shah P, Yoganathan AP. Effects of papillary muscle position on the in vitro dynamic strain on the porcine mitral valve, JHVD 2003; v.12: 488-494.

14) Quick DW, Kunzelman KS, Kneebone JM, Cochran RP. Collagen synthesis is upregulated in mitral valves subjected to altered stress. ASAIO J 1997; May-Jun; 43(3): 181-186.

15) Kunzelman KS, Quick DW, Cochran RP. Altered collagen concentration in mitral valve leaflets: biochemical and finite element analysis. Ann thorac surg 1998 Dec; 66(6 Suppl): S198-205.

16) Taylor PM, Allen SP, Yacoub MH. Phenotypic and functional characterization of interstitial cells from human heart valves, pericardium and skin. J Heart Valve Dis 2000 Jan; 9(1): 150-158.

17) Chester AH, Misfeld M, Yacoub MH. Receptor- mediated contraction of aortic valve leaflets. J Heart Valve Dis 2000, 9, 250-255.

18) Kaplan SR, Bashein G, Sheehan FH, Legget ME, Munt B, Ning Li X, Sirvarajan M, Bolson EL, Zeppa M, Martin RW. Three-dimensional echocardiographic assessment of annular shape changes in the normal and regurgitant mitral valve. Amer Heart Jour 2000; 139: 243-250.

19) Flachskampf FA, Chandra S, Gaddipatti A, Levine RA, Weyman AE, Amelig W, Hanrath P, Thomas JD. Analysis of shape and motion of the mitral annulus in subjects with and without cardiomyopathy by echocardiographic 3-dimensional reconstruction. Am Soc Echocardiogr 2000;13:277-287.

20) Tibayan FA, Lai DT, Timek TA, Dagum P, Liang D, Zasio MK, Daughters GT, Miller DC, Ingels NB. Alterations in left ventricular curvature and principal strains in dilated cardiomyopathy with functional mitral regurgitation. J Heart Valve Dis 2003; 12:292-299.

21) Gorman JH III, Gorman RC, Jackson Bm, Hiramatsu Y, Gikakis N, Kelley ST, Sutton MG, Plappert T, Edmunds LH. Distortions of the mitral valve in acute ischemic mitral regurgitation. Ann Thorac Surg 1997; 64:1026-31.

22) De Oliveira JMF, Antunes MJ. Mitral Valve Repair: Better than Replacement. Heart 2006 92: 275-281.

23) Gillinov AM, Cosgrove DM., Blackstone EH, Diaz R, Arnlod JH, Lytle BW, Smedira NG. Durability of mitral valve repair for degenerative disease. JTCVS 1998 Nov; 116(5):734-743.

24) Flameng W, Herijgers P, Bogaerts K. Recurrence of mitral valve regurgitation after mitral valve repair in degenerative valve disease. Circulation 2003 Apr 1,107(12):1609-1613.

25) Dagum P, Timek TA, Green R, Lai D, Daughters GT, Liang DH, Ingels NB, Miller DC. Three-dimensional geometric comparison of partial and complete flexible mitral annuloplasty rings. J Thorac Cardiovasc Surg 2001; 11:665-673

26) Alfieri O, Maisano F, De Bonis M, Stefano PL, Torracca L, Oppizzi M, La Canna G. The double-orifice technique in mitral valve repair: a simple solution for complex problems. J Thorac Cardiovasc Surg 2001; 122(4):674-81.

27) Bhudia SK, McCarthy PM, Smedira NG, Lam BK, Rajeswaran J, Blackstone EH. Edge-to-edge (Alfieri) mitral repair: results in diverse clinical settings. Ann Thorac Surg 2004; 77(5):1598-606.

28) Maisano F, Caldarola A, Blasio A, De Bonis M, La Canna G, Alfieri O. Midterm results of edge-to-edge mitral valve repair without annuloplasty. J Thorac Cardiovasc Surg 2003; 126(6):1987-97.

29) Kinnaird TD, Munt BI, Ignaszewski AP, Abel JG, Thompson RC. Edge-to-edge repair for functional mitral regurgitation: an echocardiographic study of the hemodynamic consequences. J Heart Valve Dis 2003;12(3):280-6.

30) Timek TA, Nielsen SL, Liang D, Lai DT, Dagum P, Daughters GT, Ingels NB Jr, Miller DC. Edge-to-edge mitral repair: gradients and three-dimensional annular dynamics in vivo during inotropic stimulation. Eur J Cardiothorac Surg. 2001;19(4):431-7.

31) Votta E, Maisano F, Soncini M, Redaelli A, Montevecchi FM, Alfieri O. 3-D computational analysis of the stress distribution on the leaflets after edge-to-edge repair of mitral regurgitation. J Heart Valve Dis. 2002;11(6):810-22.

32) McGee EC, Gillinov MA, Blackstone EH, Rajeswaran J, Cohen G, Farzad Najam F, Shiota T, Sabik JF, Lytle BW, McCarthy PM, Cosgrove DM. Recurrent mitral regurgitation after annuloplasty for functional ischemic mitral regurgitation. J Thorac Cardiovasc Surg 2004;128:916-24.

33) Liel-Cohen N, Guerrero JL, Otsuji Y. Design of a new surgical approach for ventricular remodeling to relieve ischemic mitral regurgitation: insights from three-dimensional echocardiography. Circulation 2000;101:2756-2763.

34) Mishra YK, Mittal S, Jaguri P, Trehan N. Coapsys mitral annuloplasty for chronic functional ischemic mitral regurgitation: 1-year results. Ann Thorac Surg 2006; 81(1):42-6.

35) Guyton AC, Hall JE. Human Physiology and Mechanisms of disease. W.B. Saunders Company 1997; six edition, Chapter 3: 85-114.

36) Bronzino JD. The biomedical handbook. CRC Press, Inc. 1995; Chapter 1, 3-14

37) Jensen MO. Stentles mitral valve fixation: impact on hemodynamic performance. M.Sc. Thesis, Department of Biomedical Engineering, Georgia Institute of Technology, USA, 2000.

38) Kalmanson D. The mitral valve a pluridisciplinary approach. Publishing science group, Inc. 1976; Chapter 1-5: 3-45.

39) He S, Lemmon JD, Weston MW, Jensen MO, Levine RA, Yoganathan AP. Mitral valve compensation for annular dilation: *In vitro* study into the mechanisms of functional mitral regurgitation with an adjustable annulus model. J Heart Valve Dis 1999; 8:294-302.

40) Arts T, Meerbaum S, Reneman R. Stresses in the closed mitral valve: A model study. J Biomech. 1983;16:539-547.

41) Grashow JS, Yoganathan AP, Sacks MS. Biaixal stress-stretch behavior of the mitral valve anterior leaflet at physiologic strain rates. Ann Biomed Eng. 2006 Feb;34(2):315-25.

42) Parish LM, Jackson BM, Enomoto Y, Gorman RC, Gorman JH 3rd. The dynamic anterior mitral annulus. Ann Thorac Surg. 2004 Oct;78(4):1248-55

43) Davis PKB, Kinmonth JB. The movements of the annulus of the mitral valve. J Cardiovasc Surg 1963; 4:427-431.

44) Ormison JA, Shah P, Tei C, Wong M. Size and motion of the mitral valve annulus in man. Circulation 1981;64:113-120.

45) Pai RG, Tanimoto M, Jintapakorn W, Azevedo J, Pandian NG, Shah PM. Volume-rendered three-dimensional dynamic anatomy of the mitral annulus using transesophageal echocardiographic technique. J Heart Valve Dis 1995; 4:625-627.

46) Komoda T, Hetzer R, Uyama C. Mitral annular function assessed by 3D imaging for mitral valve surgery. J Heart Valve Dis 1994; 3:483-90.

47) Aikawa K, Sheehan FH, Otto CM, Coady K, Basheim G, Bolson L. The severity of functional mitral regurgitation depends on the shape of the mitral apparatus: A three-dimensional echo analysis. J Heart Valve Dis 2002; 11:627-636.

48) Glasson JR, Komeda M, Daughters GT, Niczyporuk MA, Bolger AF, Ingels NB, Miller DC. Three-dimensional regional dynamics of the mitral annulus during left ventricular ejection. J Thorac Cardiovasc Surg 1996; 111:574-585.

49) Gorman JH III, Krishanu BG, Streicher JT, Gorman RC, Jackson Bm, Ratcliffe MB, Bogen DK, Edmunds LH. Dynamic three-dimensional imaging of the mitral valve and left ventricle by rapid sonomicrometry array localization. J Thorac Cardiovasc Surg 1996; 112:712-26.

50) Gorman JH III, Jackson Bm, Gorman RC, Kelly ST, Gikakis N, Edmunds H. Papillary muscle discoordination rather than increased annular area facilitates mitral regurgitation after acute posterior myocardial infaction. Circulation 1997; 96[suppl II]:124-127.

51) Boltwood CM, Wong M, Shah PM. Quantitative echocardiography of the mitral complex in dilated cardiomyopathy: The mechanism of functional mitral regurgitation. Circulation 1983; 68:498-508.

52) Levine RA, Triulizi MO, Harrigan P, Weyman AE. The relationship of the mitral annular shape to the diagnosis of mitral valve prolapse. Circulation 1987; 75 (IV):756-767.

53) Mikami T, Hashimoto M, Kudo T, Sugawara T, Sakamoto S, Yasuda H. Mitral valve and its ring in hypertrophic cardiomyopathy. A mechanism creating surplus mitral leaflet involved in systolic anterior motion. Jap Circ J 1998; 52:597-602.

54) Rusted IE, Schiefley CH, Edwards JE. Studies of the mitral valve: I. Anatomical features of the normal mitral valve and associated structures. Circulation 1952; 6,(6):825-831.

55) Duran C. Distribution of chordae tendineae tension in the porcine mitral valve. J Heart Valve Dis 2002; 11:335-336.

56) Sedransk KL, Allen JG, Vesely I. Failure mechanics of mitral valve chordae tendineae. J Heart Valve dis. 2002; 11:644-650.

57) Liao J, Vesely I. A structural basis for the size-related mechanical properties of mitral valve chordae tendineea. J of Biomech 2003; 36(8):1125-1133.

58) Kunzelman KS, Cochran RP, Verrier ED, Eberhart RC. Anatomic basis for mitral valve modelling. J Heart Valve Dis 1994;3(5):491-496.

59) Ritchie J, Warnock JN, Yoganathan AP. Structural characterization of the chordae tendineae in native porcine mitral valves. Ann. Thorac. Surg 2005, 80 (1), 189-97.

60) Weyman AE, Principles and Practices of Echocardiography; Lea & Febiger: Philadelphia, PA 1994.

61) Kim WY, Walker PG, Pederson EM, et al. Left ventricular blood flow patterns in normal subjects: A quantitative analysis of three-dimensional magnetic resonance velocity mapping. J. Am. Coll. Cardiol 1995, 26 (1), 224-38.

62) Bellhouse BJ. The fluid mechanics of a model mitral valve and left ventricle. Cardiovasc Res 1972, 6, 199-210.

63) Reul H, Talukder, N, Muller EW. Fluid mechanics of the natural mitral valve. J. Biomech 1981, 14 (5), 361-372.

64) Yellin EL, Peskin C, Yoran C, Koenigsberg M, Matsumoto M, Laniado S, McQueen D, Shore D, Frater RW. Mechanisms of mitral valve motion during diastole. Am J Physiol. 1981 Sep;241(3):H389-400.

65) He S, Fontaine AA, Schwammental E, Yoganathan AP, Levine RA. Integrated mechanism for functional mitral regurgitation: leaflet restriction versus coaptation force: in vitro studies. Circulation 1997; 16;96(6):1826-1834.

66) Nielsen SL, Nygaard H, Fontaine AA. Chordal force distribution determines systolic mitral leaflet configuration and severity of functional mitral regurgitation. J am Coll Cardiol 1999; 33(3):843-853.

67) Einstein DR, Kunzelman KS, Reinhall PG, Nicosia MA, Cochran RP. Non-linear fluid-coupled computational model of the mitral valve. J Heart Valve Dis. 2005 May;14(3):376-85.

68) He Z, Ritchie J, Grashow JS, Sacks MS, Yoganathan AP. In vitro dynamic strain behavior of the mitral valve posterior leaflet. J. Biomech. Eng 2005, 127 (3), 504-511.

69) Nazari S, Carli F, Bnfi C, Aluffi A, Mourad Z, Buniva P, Rescigno G. Patterns of systolic stress distribution on mitral valve anterior leaflet chordal apparatus. J Cardiovasc Surg 2000; 41:193-202 .

70) He S, Weston MW, Lemmon J, Jensen M, Levine RA, Yoganathan AP. Geometric distribution of chordae tendineae: An important anatomic feature in mitral valve function. J Heart Valve Dis 2000; 9:495-501.

71) Lomholt M, Nielsen SL, Hansen SB, Andersen NT, Hasenkam JM. Differential tension between secondary and primary mitral chordae in acute in-vivo porcine model. J Heart valve Dis 2002; 11:337-345.

72) Lim KO, Bouchner DP. Mechanical properties of human mitral valve chordae tendineae: Variation with size and strain rate. Can. J. Physiol. Pharmacol 1975, 53, 330-39.

73) Ritchie J, Jimenez J, He Z, Sacks MS, Yoganathan AP. The material properties of the native porcine mitral valve chordae tendineae: an in vitro investigation. J Biomech. 2006;39(6):1129-35.

74) Jensen MO, Fontaine, A, Yoganathan AP. Improved In Vitro Quantification of the Force Exerted by the Papillary Muscle on the Left Ventricular Wall Three Dimensional Force Vector Measurement System Ann Biomed Eng 2000;10:111-124.

75) Pinto JG, Fung YC. Mechanical properties of the heart muscle in the passive state. J. Biomech 1973, 6, 596-616.

76) Fung YC. Biomechanics: Mechanical Properties of Living Tissues. Springer-Verlag: New York, NY 1981.

77) Black A, French AT, Dukes-McEwan J, Corcoran BM. Ultrastructural morphologic evaluation of the phenotype of valvular interstitial cells in dogs with myxomatous degeneration of the mitral valve. Am J Vet Res 2005 Aug; 66(8):1408-14.

78) Baker PB, Bansal G, Boudoulas H, Kolibash AJ, Kilman J, Wooley CF. Floppy mitral valve chordae tendineae: histopathologic alterations. Hum Pathol 1988 May; 19(5):507-12.

79) Mills WR, Barber JE, Ratliff NB, Cosgrove DM 3rd, Vesely I, Griffin BP. Biomechanical and echocardiographic characterization of flail mitral leaflet due to myxomatous disease: further evidence for early surgical intervention. Am Heart J 2004 Jul; 148(1):144-50.

80) Corcoran BM, Black A, Anderson H, McEwan JD, French A, Smith P, Devine C. Identification of surface morphologic changes in the mitral valve leaflets and chordae tendineae of dogs with myxomatous degeneration. Am J Vet Res 2004 Feb;65(2):198-206.

81) Lembo NJ, Dell LJ, Crawford MH, Miller JF, Richards KL, O'Rourke RA. Mitral valve prolapse in patients with prior rheumatic fever. Circ 1998; 77(4):830 -836.

82) Barber JE, Ratliff NB, Cosgrove DM 3rd, Griffin BP, Vesely I. Myxomatous mitral valve chordae. I: Mechanical properties. J Heart Valve Dis. 2001 May;10(3):320-4.

83) Dagum P, Timek TA, Green R, Lai D, Daughters GT, Liang DH, Hayse M, Ingels NB, Miller DC. Coordinate- free analysis of mitral valve dynamics in normal and ischemic hearts. Circulation 2000; 102[suppl III]:III-62-III-69.

84) He S, Jimenez JH, He Z, Yoganathan AP. Mitral leaflet geometrical perturbations with papillary muscle displacement and annular dilation: An in-vitro study of ischemic mitral regurgitation. J Heart Valve Dis 2003;12(3):300-307.

85) Nielsen SL, Nygaard H, Fontaine, Hasenkam JM, He S, Yoganathan AP. Papillary muscle misalignment causes multiple regurgitation jets: An ambiguous mechanism for functional mitral regurgitation. J Heart Valve Dis 1999;8:551-564.

86) Grande-Allen KJ, Borowski AG, Troughton RW, Houghtaling PL, Dipaola NR, Moravec CS, Vesely I, Griffin BP. Apparently normal mitral valves in patients with heart failure demonstrate biochemical and structural derangements: an extracellular matrix and echocardiographic study. J Am Coll Cardiol 2005 Jan 4;45(1):62-4.

87) Grande-Allen KJ, Barber JE, Klatka KM, Houghtaling PL, Vesely I, Moravec CS, McCarthy PM. Mitral valve stiffening in end-stage heart failure: evidence of an organic contribution to functional mitral regurgitation. J Thorac Cardiovasc Surg 2005 Sep;130(3):783-90.

88) Grande-Allen KJ, Ratliff NB, Griffin BP, Cosgrove DM 3rd, Vesely I. Case report: outer sheath rupture may precede complete chordal rupture in fibrotic mitral valve disease. J Heart Valve Dis 2001 Jan;10(1):90-3.

89) Lessana A, Carbone C, Romano, M, et al. Mitral valve repair: results and the decision-making process in reconstruction - report of 25 cases. JTCVS 1990, 99: 622-630.

90) Cosgrove DM, Arcidi JM, Rodriguez L, Stewart WJ, Powell K, Thomas JD. Initial experience with the Cosgrove-Edwards Annuloplasty System. Ann Thorac Surg 1995, 60: 499-503.

91) Carpentier AF, Lessana A, Relland M, Belli E, Mihaileanu S, Berrebi AJ, Palsky E, Loumet DF. The "Physio-Ring": an advanced concept in mitral valve annuloplasty. Ann Thorac Surg 1995; 60: 1177-1178.

92) Webb JG, Harnek J, Munt BI, Kimblad PO, Chandavimol M, Thompson CR, Mayo JR, Solem JO. Percutaneous transvenous mitral annuloplasty: initial human experience with device implantation in the coronary sinus. Circulation. 2006 Feb 14;113(6):851-5.

93) Alfieri O, Maisano F, De Bonis M, Stefano PL, Torracca L, Oppizzi M, La Canna G. The double-orifice technique in mitral valve repair: a simple solution for complex problems. J Thorac Cardiovasc Surg 2001; 122(4):674-81.

94) Bhudia SK, McCarthy PM, Smedira NG, Lam BK, Rajeswaran J, Blackstone EH. Edge-to-edge (Alfieri) mitral repair: results in diverse clinical settings. Ann Thorac Surg 2004; 77(5):1598-606.

95) Kinnaird TD, Munt BI, Ignaszewski AP, Abel JG, Thompson RC. Edge-to-edge repair for functional mitral regurgitation: an echocardiographic study of the hemodynamic consequences. J Heart Valve Dis 2003;12(3):280-6.

96) Timek TA, Nielsen SL, Liang D, Lai DT, Dagum P, Daughters GT, Ingels NB Jr, Miller DC. Edge-to-edge mitral repair: gradients and three-dimensional annular dynamics in vivo during inotropic stimulation. Eur J Cardiothorac Surg 2001;19(4):431-7.

97) Timek TA, Nielsen SL, Lai DT, Tibayan FA, Liang D, Rodriguez F, Daughters GT, Ingels NB, Jr Miller DC. Edge to edge mitral valve repair without ring annuloplasty for acute ischemic mitral regurgitation. Circulation 2003 Sep 9, 108 Suppl 1: II 122-127.

98) Maisano F, Caldarola A, Blasio A, De Bonis M, La Canna G, Alfieri O. Midterm results of edge-to-edge mitral valve repair without annuloplasty. J Thorac Cardiovasc Surg 2003; 126(6):1987-97.

99) Votta E, Maisano F, Soncini M, Redaelli A, Montevecchi FM, Alfieri O. 3-D computational analysis of the stress distribution on the leaflets after edge-to-edge repair of mitral regurgitation. J Heart Valve Dis 2002;11(6):810-22.

100) Nielsen SL, Timek TA, Lai DT, Daughters GT, Liang D, Hasenkam JM, Ingels NB, Miller DC. Edge-to-edge mitral repair: tension on the approximating suture and leaflet deformation during acute ischemic mitral regurgitation in the ovine heart. Circulation 2001; 104(12 Suppl 1):I29-35.

101) Timek TA, Nielsen SL, Lai DT, Tibayan F, Liang D, Daughters GT, Beineke P, Hastie T, Ingels NB Jr, Miller DC. Mitral annular size predicts Alfieri stitch tension in mitral edge-to-edge repair. J Heart Valve Dis 2004;13(2):165-73.

102) Tawn Z, Himbert D, Brochet E, Messika-Zeitoun D, Iung B, Vahanian A. Percutaneous valve procedures: present and future. Int J Cardiovasc Intervent 2005; 7(1):14-20.

103) Alfieri O, Maisano F, Colombo A, Pappone C, La Canna G, Zangrillo A. Percutaneous mitral valve repair: an attractive perspective and an opportunity for teamwork. Ital Heart J 2004; 5(10):723-6.

104) Timek TA, Lai DT, Liang D, Tibayan F, Langer F, Rodriguez F, Daughters G.T, Ingels NB, Jr Miller DC. Effects of paracommissural septal-lateral annular cinching on acute ischemic mitral regurgitation. Circulation 2004 Sep 14;110(11 Suppl 1):II79-1184.

105) Tibayan FA, Rodriguez F, Langer F, Zasio MK, Bailey L, Liang D, Daughters GT, Ingels NB, Jr Miller DC. Does septal-lateral annular cinching work for chronic ischemic mitral regurgitation? JTCVS 2004 Mar;127(3):654-663.

106) Timek TA, Lai DT, Tibayan F, Liang D, Daughters GT, Dagum P, Ingels NB, Jr Miller DC. Septal-lateral annular cinching abolishes acute ischemic mitral regurgitation. JTCVS 2002 May;123(5):881-888.

107) Timek TA, Lai DT, Tibayan FA, Daughters GT, Liang D, Dagum P, Ingels NB, Jr Miller DC. Septal-lateral annular cinching ('SLAC) reduces mitral annular size without perturbing normal annular dynamics. JHVD 2002 Jan;11(1):2-9; discussion 10.

108) Moanie SL, Guy S, Gorman JH, Plappert T, Jackson B, St. John-Sutton MG, Edmunds HL, Gorman RC. Infarct restraint attenuates remodeling and reduces chronic ischemic mitral regurgitation after postero-lateral infarction. Ann Thorac Surg 2002; 74:444-449.

109) Messas E, Guerrero JL, Handschumacher MD, Conrad C, Chow C, Sullivan S, Yoganathan AP, Levine RA. Chordal cutting, a new therapeutic approach for ischemic mitral regurgitation. Circulation 2001; 104:1958-1963.

110) Wakiyama H, Okada Y, Kitamura A, Tsuda S, Shomura Y, Shinkai M, Fujiwara H, Handa N, Nasu M, Tanabe K, Tani T, Morioka S. Chordal cutting for the treatment of ischemic mitral regurgitation: two case reports. J Cardiol. 2004 Sep;44(3):113-7.

111) Rodriguez F, Langer F, Harrington KB, Tibayan FA, Zasio MK, Liang D, Daughters GT, Ingels NB, Miller DC. Cutting second-order chords does not prevent acute ischemic mitral regurgitation. Circulation. 2004 Sep 14;110(11 Suppl 1):II91-7.

112) Kasegawa H, Shimokawa T, Shibazaki I, Hayashi H, Koyanagi T, Ida T. Mitral valve repair for anterior leaflet prolapse with expanded polytetrafluoroethylene sutures. Ann Thorac Surg 2006 May;81(5):1625-31.

113) Lam BK, Gillinov AM, Cosgrove DM 3rd. Failed mitral valve repair caused by polypropylene suture. Ann Thorac Surg 2003 Nov;76(5):1716-7.

114) Shi Y, Vesely I. Fabrication of mitral valve chordae by directed collagen gel shrinkage. Tissue Eng. 2003 Dec;9(6):1233-42.

115) Duran CM, Pekar F. Techniques for ensuring the correct length of new mitral chords. J Heart Valve Dis 2003 Mar;12(2):156-61.

116) Rankin JS, Orozco RE, Rodgers TL, Alfery DD, Glower DD. "Adjustable" artificial chordal replacement for repair of mitral valve prolapse. Ann Thorac Surg 2006 Apr; 81(4):1526-8.

117) Smedira NG, Selman R, Cosgrove DM, McCarthy PM, Lytle BW, Taylor PC, Apperson-Hansen C, Stewart RW, Loop FD. Repair of anterior leaflet prolapse: chordal transfer is superior to chordal shortening. J Thorac Cardiovasc Surg 1997 Dec; 114(6):1125-7.

118) Fundaro P, Lemma M, Di Mattia DG, Santoli C. Repair of anterior leaflet prolapse: chordal transfer versus chordal shortening. Which is better? J Thorac Cardiovasc Surg 1996 Aug; 112(2):287-91; discussion 291-2.

119) Ritchie J. The material properties of the chordae tendineae of the mitral valve : an in vitro investigation. M.Sc. Thesis, Department of Biomedical Engineering, Georgia Institute of Technology, USA, 2004.

120) Jimenez JH. The effects of mitral annular dynamics and papillary muscle position on chordal force distribution and valve function: an in vitro study. M.Sc. Thesis, Department of Biomedical Engineering, Georgia Institute of Technology, USA, 2003.

121) Iyengar A, Sugimoto H, Smith DB, Sacks M. Dynamic in vitro 3D reconstruction of heart valve leaflets using structured light projection. Ann Biomed Eng 2001; 29: 963-973.

122) Marzan GT. A computer program for direct linear transformation solution of the collinearity condition and some applications of it. Proceedings of the Symposium on close-range Photogrammetric Systems, 1975, 420-476.

123) Kinney EL, Frangi MJ. Value of two-dimensional echocardiographic detection of incomplete mitral leaflet closure. Am Heart J 1985; 109:87-90.

124) Kaul S, Pearlman JD, Touchstone DA, Esquival L. Prevalence and mechanism of mitral regurgitation in absence of intrinsic abnormalities of the mitral leaflets. Am Heart J 1989; 118: 963-972.

125) Kaul S, Spotnitz WD, Glasheen WP, Touchstone DA. Mechanism of ischemic mitral regurgitation: An experimental evaluation. Circulation 1991; 84:2167-2180.

126) Perloff Jk, Roberts WC. The mitral apparatus. Functional anatomy of mitral regurgitation. Circ 1972; 46:227-239.

127) Kono T, Sabbah HN, Rosman H, Alam M, Jafri S, Goldstein S. Left ventricular shape is the primary determinant of functional mitral regurgitation in heart failure. J Am Coll Cardiol 1992; 20:1594-1598.

128) Ojtsuji Y, Handshumacher MD, Schwammenthal E, Jiang L, Song JK, Vlahakes GJ, Levine RA. Insights from three-dimensional echocardiography into the mechanism of functional mitral regurgitation: Direct *in vivo* demonstration of altered leaflet tethering geometry. Circ 1997; 96:1999-2008.

129) Izumi S, Miyatake K, Beppu S, et al. Mechanism of mitral regurgitation in patients with myocardial infarction: A study using real-time two-dimensional Doppler flow imaging and echocardiography. Circulation 1987; 76:777-785.

130) Godley RW, Wann LS, Rogers EW, Feigenbaum H, Weyman AE. Incomplete mitral leaflet closure in patients with papillary muscle dysfunction. Circulation 1981; 63:565-571.

131) Tei C, Sakamaki T, Shah PM, Meerbaum S, Kondo S, Shimoura K, Corday E. Mitral valve prolapse in short-term experimental coronary occlusion: A possible mechanism of ischemic mitral regurgitation. Circulation 1983;68:183-189.

132) Jensen MO, Lemmon JD, Gessaghi VC, Conrad CP, Levine RA, Yoganathan AP. Harvested porcine mitral xenograft fixation: impact on fluid dynamic performance. J Heart Valve Dis 2001, 10:11-124.

133) Sacks MS, Enomoto Y, Graybill JR, Merryman WD, Zeeshan A, Yoganathan AP, Levy RJ, Gorman RC, Gorman JH 3rd. In-vivo dynamic deformation of the mitral valve anterior leaflet. Ann Thorac Surg 2006 Oct;82(4):1369-77.

134) Nielsen SL. The Impact of Chordal Force Distribution on Functional Mitral Regurgitation – In Vitro Studies. M.Sc. Thesis, Faculty of Health Sciences, University of Aarhus, Denmark, 1999.

135) Nichols WW, O'Rourke MF. The nature of flow of a fluid, in Nichols WW, O'Rourke MF (eds): McDonald's Blood flow in arteries. Theoretical, experimental and clinical principles. Philidelphia, Lea & Febiger 1999: 12-53.

136) Nielsen SL, Soerensen DD, Libergren P, Yoganathan AP, Nygaard H. Miniature C-shaped transducers for chordae tendineae force measurements. Ann Biomed Eng. 2004 Aug;32(8):1050-7.